Title

Fast motional Stark effect diagnostic measurements of hybrid-like magnetic flux-pumping and neoclassical tearing modes in the DIII-D tokamak

Author

King, Joshua Daniel

Publication Date

2011

Peer reviewed|Thesis/dissertation

Fast motional Stark effect diagnostic measurements of hybrid-like magnetic flux-pumping and neoclassical tearing modes in the DIII-D tokamak

By

Joshua Daniel King

A dissertation submitted in partial satisfaction of the

requirements for the degree of

Doctor of Philosophy

in

Engineering - Nuclear Engineering

in the

Graduate Division

of the

University of California, Berkeley

Committee in charge:

Professor Edward C. Morse, Chair
Visiting Professor Brian D. Wirth
Professor Stuart D. Bale
Michael A. Makowski

Fall 2011

Abstract

Fast motional Stark effect diagnostic measurements of hybrid-like magnetic flux-pumping and neoclassical tearing modes in the DIII-D tokamak

by

Joshua Daniel King

Doctor of Philosophy in Nuclear Engineering
University of California, Berkeley

Professor Edward C. Morse, Chair

MSE measurements reveal hybrid-like flux-pumping associated with 2/1 NTM-ELM coupling. Analysis of MSE signals using digital lock-in amplifiers shows the strength of the flux-pumping is more than twice that of typical hybrid discharges. This flux-pumping maintains the minimum safety factor above unity, thereby avoiding sawteeth. The strength of the flux-pumping and ELM-NTM coupling have a clear upward dependence on normalized beta and NTM-pedestal proximity. The size of the island does not appear to effect flux-pumping, except that the mode must be present, suggesting the island chain serves as a radial pivot surface around which poloidal flux is pumped from the core to the edge. This result implies that higher normalized fusion performance (lower q_{95} and higher beta) may be achieved in hybrid discharges that contain a partially suppressed 2/1 NTM. ELM-NTM coupling consists of an Alfvénic timescale drop in the island width followed by a resistive recovery. The recovery phase is successfully modeled using the modified Rutherford equation. The depth of the drop in island width increases as the size of the ELM increases.

To aid in the design of a highly resolved MSE pedestal measurement, full spectral analysis was preformed on existing edge channels. This analysis has revealed that coherent core MHD oscillations cause interference with present dual PEM polarimeters. Avoiding this interference requires a dedicated pedestal polarimeter with second harmonic frequencies greater than those of MHD fluctuations.

Dedication

To Julie Hess

Your encouragement made this possible.

Acknowledgements

Thanks to my wife, Denise, for her love and sacrifice.

Thanks to my parents, Mark and Jackie, for their guidance and support.

Thanks to my sister, Kilee, for her friendship.

Contents

List of Figures and Tables

Chapter 1

Introduction

1.1 Nuclear Fusion Energy

The preponderance of ordinary matter in the universe is comprised of the element hydrogen. Utilizing this abundant substance for controlled energy generation would be mankind's most transcendent achievement. The process of converting hydrogen into energy is known as nuclear fusion.

1.1.1 Historical Context

Since its declassification in 1958[1], nuclear fusion for the production of electrical energy has been a research interest of the United States and other governments. It holds the promise of providing mankind a virtually endless supply of clean energy. However, the challenges associated with creating and harnessing this energy are vast.

A nuclear fusion reaction requires the collision of two nuclei with sufficient energy to overcome coulomb repulsion and allow the overlap of nuclear distributions[2]. Macroscopically overcoming this coulomb repulsion requires the generation of high temperature neutral plasma. The complex dynamics of laboratory plasma required the invention of a new physics discipline. Early analytical work in the 60's and 70's provides the basis for much of modern plasma physics.[3]

Despite encouraging progress, and the establishment of scientific feasibility[4], efforts to develop fusion into an energy source stalled in the early 1980's. In place of energy development were programs focused on fusion science. This has resulted in the construction of numerous medium-sized plasma physics devices around the world. These machines are used to study subtle physics associated with controlling future fusion plasmas.

Political impasses, funding retractions and reinstatements, and international squabbles over construction sites have extended the timeline for mankind's first net energy gain experiment[5] from around the year 2000[6] to currently the year 2027 at the earliest[7]. The current fusion energy effort is an international consort of 33 sovereign countries originally known as the International Thermonuclear Experimental Reactor[7] (ITER) project. Construction of ITER recently began in Cadarache, France and if completed will be the first fusion device large enough to create the necessary densities,

temperatures and energy confinement times[8] to initiate a nuclear fusion burn in excess of auxiliary input power. This effort will be the largest scientific endeavor ever attempted.

1.1.2 Fundamentals

The nuclear reaction whereby two nuclei combine to form a larger nucleus is known as nuclear fusion. This reaction may either release or consume kinetic energy depending on the binding energies of the products and reactants. The exothermic variant of nuclear fusion is of interest for the purposes of electrical power production. This type of reaction consists of a two-body collision that yields a minimum of two bodies to carry the resultant kinetic energy. The intermediate state of compound nucleus formation and decay is neglected, as the timescales[2] involved (10^{-16} to 10^{-18} s) are inconsequential for our purposes.

The largest peak fusion reaction cross section is that of colliding deuterium (D) and tritium (T). This reaction takes the form,

$$D + T \rightarrow {}^{4}He\ (3.5\ MeV) + {}^{1}_{0}n\ (14.1\ MeV) \quad , \tag{1.1}$$

where ${}^{1}_{0}n$ denotes a neutron. Because nuclei are positively charged their Coulomb barrier must be mostly overcome before nucleon interactions are possible. This D-T reaction has the smallest Coulomb barrier possible.

Because scattering is much more likely than fusion, producing energy through beam collisions is impossible. Instead, fusion energy research focuses on the collective. Raising the temperature and density of a quasineutral plasma to sufficiently high values for a long enough duration produces copious fusion reactions.

The acceleration of charged particles due to Coulomb scattering results in Bremsstrahlung light emissions. These emissions are a source of energy loss in high temperature plasma. The essence of fusion energy research is to obtain a plasma that produces more energy through fusion than is lost. Fig. 1.1.2-1 compares fusion power density and Bremstrahlung radiation as a function of temperature. This plot assumes a high density of 10^{21} m^{-3}. It can be seen that beyond 4 keV the plasma radiates less energy than is created. Attaining these high temperatures requires specialized auxiliary heating systems, which will be described in later sections. Note, this plot assumes no high Z impurities are present. In reality atoms from solid wall materials surrounding the plasma are ionized and radiate. For this reason high vacuum (10^{-9} Torr) is required prior to initiating a discharge.

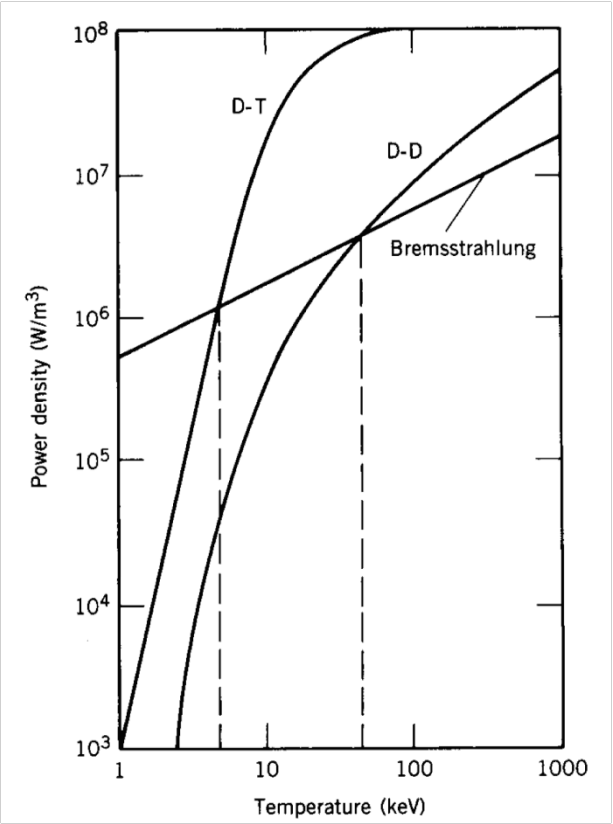

FIG. 1.1.2-1: Power density of D-T and D-D fusion, and Bremsstahlung radiation for an ion density of 10^{21} m^{-3}. (Reprinted from Ref. 2)

Power can be lost from plasma by means other than radiation. An accurate power balance must account for all sources. In general, we can define the total fusion gain Q as,

$$Q \equiv \frac{P_{fus}}{\left(P_{loss} - P_{\alpha}\right)} \quad , \tag{1.2}$$

where, P_{fus} is the total fusion power, P_{loss} is the total power lost from the plasma, and P_{α} is the component of the fusion power attributed to α particle (helium nuclei) heating. The condition where the power output is equivalent to the power input (Q is unity) is known as breakeven. This has been approximately achieved in the Joint European Torus[9] (JET), and the equivalent conditions have been reached in the Japanese JT-60U.[10] In the case where α heating balances losses, the denominator of Eq. (1.2) vanishes and fusion gain approaches infinity. This condition is known as ignition, and corresponds to the point at which auxiliary heating systems can be switched off and a nuclear fire can burn self-sustainingly.

The attractiveness of this energy source comes from the nearly infinite abundance of fusion fuel. On earth deuterium isotopes constitute roughly 1 in every 6400 atoms of hydrogen. However, tritium has no natural presence. To sustain a closed fuel cycle tritium must be breed using another naturally abundant atom.[11] The metal lithium is

readily found in the earth's crust and oceans and is able to react with both fast and slow neutrons as follows,

$$\begin{aligned} {}^{6}\mathrm{Li} + {}^{1}_{0}\mathrm{n}_{\mathrm{thermal}} &\rightarrow {}^{4}\mathrm{He} + \mathrm{T} \\ {}^{7}\mathrm{Li} + {}^{1}_{0}\mathrm{n}_{\mathrm{fast}} &\rightarrow {}^{4}\mathrm{He} + \mathrm{T} + {}^{1}_{0}\mathrm{n} \end{aligned} \quad . \tag{1.3}$$

With these few facts in mind a fusion power plant can be summarized as follows. The D and T burn inside a fusion reactor emitting very energetic neutrons. These neutrons pass through the plasma and interact with a surrounding blanket comprised of lithium metal. Inside this blanket the neutrons undergo multiple scattering collisions, imparting thermal energy to the blanket material, which will serve to boil water, turn a turbine and generate electricity. After numerous collisions, the neutron will react with the lithium as shown in Eq. (1.3). The resulting T will then be removed from the blanket material and injected into the plasma, thereby completing the D-T fusion fuel cycle.

1.2 The Tokamak for Burning Plasmas

In the pursuit of fusion energy numerous configurations have been studied. These devices include Spheromaks[12,13], Reverse-Field Pinches[14], Stellarators[15], Magnetic Mirrors[16] and Levitating Dipoles[17] to name a few. While many of these alternative concepts show great promise, the device with by far the most developed physics basis is a toroidal vacuum chamber with magnetic field coils known as the Tokamak. Following, the Russsian T-3 tokamak achievement of a 10 million degree laboratory plasma in 1969, this configuration has been globally adopted as the preferred path toward accessing the burning plasma regime[18]. It is important to note, the tokamak has become the most developed configuration because it was the first device to satisfy the temperature and confinement goals of the day and not because other concepts are inferior. Many alternative devices have not been ruled out as viable options, and may some day be preferred for commercial fusion power generation[3].

1.2.1 Magnetic Confinement

A tokamak is composed of a torus shaped vessel maintained at extreme vacuum conditions (10^{-9} Torr) by a combination of roughing, turbo, and cryopumps. Surrounding the vacuum vessel are large magnetic field coils with turns in the poloidal direction. These coils are referred to as toroidal field coils as they generate a magnetic field in the toroidal direction (B_ϕ). The strength of this field is inversely related to major radius $B_\phi \propto 1/R$. A schematic diagram showing a poloidal cross section of the DIII-D tokamak[19] is shown in Fig. 1.2.1-1.

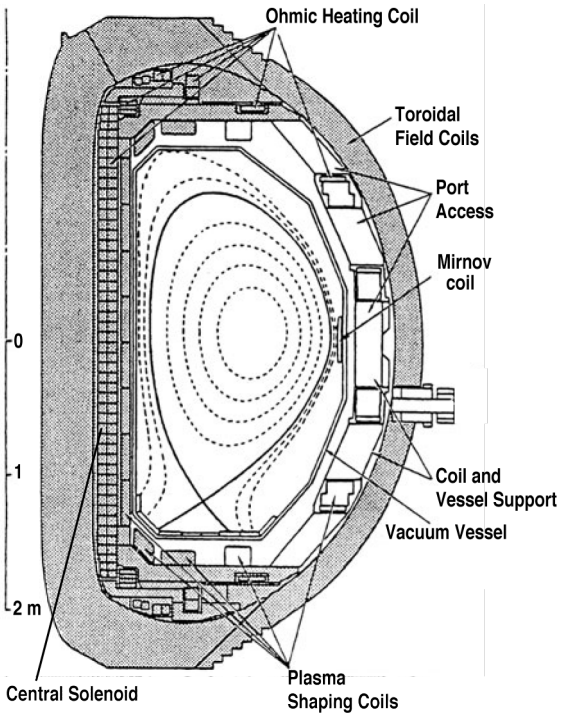

FIG. 1.2.1-1: Schematic of a poloidal cross section of the DIII-D tokamak. (Reprinted from Ref. 19)

A toroidal magnetic field alone can not confine a plasma away from the walls of the vessel. This is because the toroidal curvature and the radial gradient of the field produce particle drifts. The combination of these drift velocities are written as,

$$\vec{v}_{\vec{\nabla}B} + \vec{v}_C = \frac{-m\vec{\nabla}B \times \vec{B}}{qB^3}\left(v_{//}^2 + v_{\perp}^2/2\right) \quad , \tag{1.4}$$

where $\vec{v}_C$ and $\vec{v}_{\vec{\nabla}B}$ are the curvature and field gradient components of the drift velocities respectively, $v_{//}$ and $v_{\perp}$ are the speeds of the particles oriented along and perpendicular to the magnetic field, m is the mass of the ion or electron, and q is the charge[20]. The direction of the ion drift is opposite that of the electron due to the sign of q. Fig. 1.2.1-2 shows that the ions drift to the top of the plasma while the electrons drift to the bottom. The particles are not lost to the wall since these drifts are not sufficiently strong to overcome electrical attraction. Instead, charge separation generates a vertical electric field that is perpendicular to the toroidal magnetic field. This results in a unidirectional drift of ions and electrons radially outward to the wall. The expression describing this drift velocity ($\vec{v}_{\vec{E}\times\vec{B}}$) is[21],

$$v_{\vec{E}\times\vec{B}} = \frac{\vec{E} \times \vec{B}}{B^2} \quad . \tag{1.5}$$

This means that a plasma confined solely by a toroidal field will result in the loss of all particles to the outer wall through $\vec{E} \times \vec{B}$ drift.

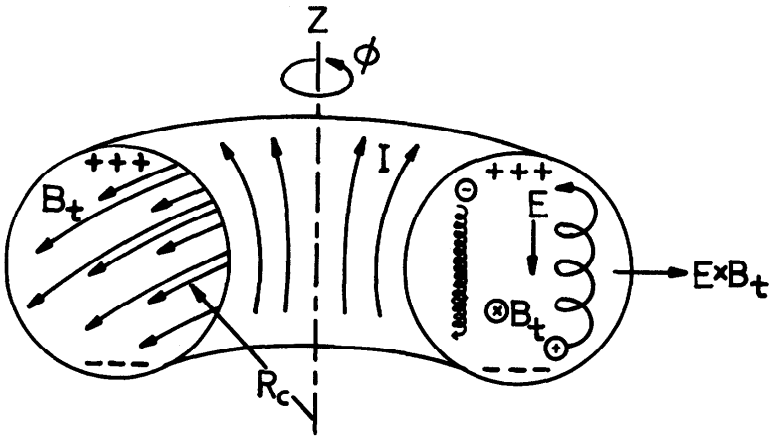

FIG. 1.2.1-2: A cross cut of a magnetized torus. I is the current running through the toroidal field coils. B_t is the toroidal field. The charge separation due to the curvature and gradient of B_t produces an electric field resulting in radial particle drift to the outer wall. (Reprinted from Ref. 11)

By supplying a magnetic field in the poloidal direction (B_θ) the $\vec{E} \times \vec{B}$ drift velocity can be negated. The net result is a confining magnetic field with helical structure. This helical twist of the field lines can be described as the rate of change in toroidal flux Φ with respect to poloidal flux ψ and is called the safety factor $q \equiv d\Phi/d\psi$. The name safety factor relates to the impact this ratio has in determining plasma stability.

In tokamaks, driving a torroidal current through the plasma itself generates the poloidal magnetic field. The primary method of initiating the current is using a solenoid. The solenoid is located in the center of the torus with turns in the toroidal direction. Ramping current through this coil generates a strong toroidal electric field, which ohmically drives current throughout the plasma volume. Other toroidal coils, known as poloidal field coils, partially contribute to the poloidal field strength. These coils, shown in Fig. 1.2.1-1, surround the outside of the torus and are used for pulling the plasma into a desired shape.

The obtainable magnetic fields in a tokamak are limited by technological constraints associated with the present state of super conductors. It is therefore imperative that the applied magnetic fields efficiently suspend the plasma away from the walls. This efficiency is defined by taking the ratio of kinetic plasma pressure (p) to magnetic pressure. This parameter is known as beta and can be written as,

$$\beta = \frac{p}{B^2/2\mu_0} \quad . \tag{1.6}$$

Beta can be normalized with respect to ideal kink mode stability limits[22] as follows,

$$\beta_N = \frac{\beta}{I/aB_\phi} \quad , \tag{1.7}$$

where I is plasma current (MA), and a is the plasma minor radius (m).

1.2.2 Heating and Current Drive

Heating and driving current in tokamaks relies on ohmic, neutral beam, electromagnetic (EM) wave, and α particle sources. This section aims to outline the design of each source, and describe the physical mechanisms whereby electrical and thermal energy is transmitted to the plasma.

Ohmic current drive was described in the previous section as a plasma current induced from ramping current in a central solenoid. Ohmic heating relies on this same process. As the toroidal electric field accelerates electrons, to generate the plasma current, they collide with the relatively stationary ions and neutral atoms imparting their energy, thereby raising the bulk temperature of the plasma. Because collisionality decreases as the temperature of the bulk plasma increases, ohmic heating produces diminishing returns.

Heating beyond the limits of ohmic sources is achieved through neutral beam injection. A neutral beam is a high-energy beam of neutral atoms. The components of a neutral beam injector are shown in Fig. 1.2.2-1. To generate a neutral beam, a plasma, known as an ion source, is created with the desired ion species to be injected. Fusion energy experiments inject either deuterium or tritium. The ions are extracted from the source and accelerated to a prescribed energy through a series of accelerator grids. At this point an ion beam has been created. Because the ions are charged particles, it is not possible to inject them directly into the plasma as the magnetic component of the Lorentz force would be nonzero. Deposition of the beams energy into the bulk plasma is achieved by passing the beam through a neutralizing background gas before entering the tokamak. As the beam passes through the neutralizer gas it undergoes charge exchange collisions allowing for a significant fraction of the high-energy particles to be neutralized without significant energy loss. These high-energy neutral atoms pass through the magnetic field before undergoing either a charge exchange, ionization by ion, or ionization by electron reaction. After this collision, the now high-energy charged particle makes many toroidal transits around the torus at a faster rate than the bulk plasma electrons. *Oppositely charged particles moving at different velocities* is the definition of current. As the particle transits it loses energy to the background plasma through collisions.

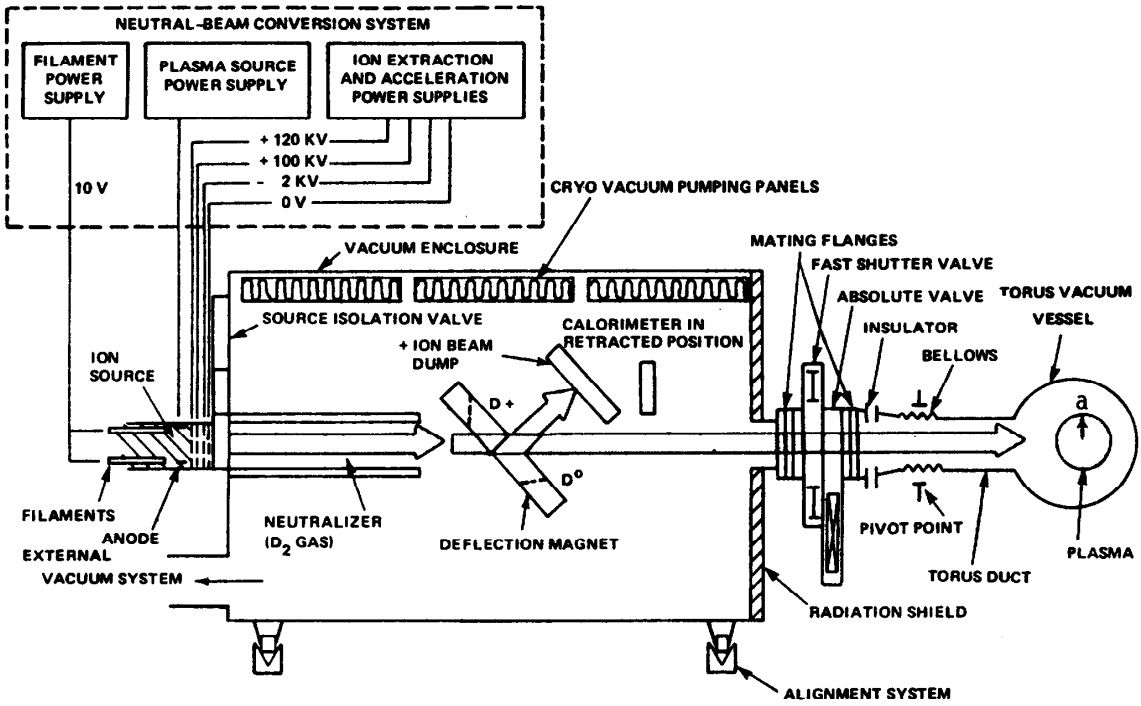

FIG. 1.2.2-1: Schematic of a neutral beam injector from the TFTR tokamak. (Reprinted from Ref. 11)

Note the contrast between ohmic and neutral beam sources. In the ohmic case energetic electrons are the moving charges of the induced current and their collisions with background ions increase the plasma energy. In the case of a neutral beam the current and heat are carried by the ions. For this reason, in strongly neutral beam heated plasmas the temperature of the ions is larger than that of the electrons.

EM waves utilize resonant plasma frequencies to impart energy. One example is the electron cyclotron resonance,

$$\omega_{ce} = \frac{eB}{m_e} \quad , \tag{1.8}$$

where ω_{ce} is the electron cyclotron frequency and m_e is the mass of an electron. In the case of electron cyclotron heating, the wave increases the velocity of the electrons orbiting the magnetic field lines. These fast electrons thermalize with ions through collisions raising the plasma temperature. Electron cyclotron current drive (ECCD) relies on preferentially heating electrons with parallel velocity components in a particular toroidal direction. This is done by tuning the ECCD system to be resonant with a Doppler shifted frequency. The hotter electrons flowing in one direction will have smaller collisionality than the electrons moving in the other direction. For this reason, the slower electrons collide more frequently with ions causing them to have a net drift opposite that of the fast electrons, producing a current.

EM current drive and heating allow tokamaks to operate continuously, rather than having to pulse the central solenoid, which mechanically stresses the machine.

Furthermore, EM power allows for the localized deposition of energy, and rapid changes in the deposition location. This is particularly useful in efforts to suppress and control plasma instabilities.

Self-heating through fusion α particles simply relies on collisions with the background plasma. Because the α particles are emitted isotropically, their motion does not directly generate a net current. Instead the heating indirectly generates a current by creating a gradient in the radial plasma pressure profile, which induces a bootstrap current[23]. It is this current that may allow tokamaks to achieve steady state[24] thermonuclear ignition. Bootstrap current will be discussed further in later sections.

1.2.3 Magnetohydrodynamics

Approximating a tokamak plasma as a single species conducting fluid greatly simplifies the governing equations. This fluid theory is known as Magneto-hydrodynamics (MHD), and is used to study low frequency, large spatial scale phenomena. While some areas require more detail, like turbulent transport[25], a variety of applications, from equilibrium reconstruction to tearing mode stability, have shown the MHD description to be sufficient. The following derivation follows Ref. 26 and 20.

MHD equations are derived from the Vlasov equation,

$$\frac{\partial f}{\partial t} + \vec{v}\cdot\vec{\nabla} f + \frac{\vec{F}}{m}\frac{\partial f}{\partial \vec{v}} = 0 \qquad , \tag{1.9}$$

where $f(\vec{r},\vec{v},t)$ is a distribution function, $\vec{F}$ is a force, and m is the mass of a fluid element. By taking a series of moments of the Vlasov equation a series of equations describing the plasma may be obtained. However because of the $\vec{v}\cdot\vec{\nabla} f$ term, each moment requires an additional moment in order to satisfy the equation. To close this system we must truncate using an equation of state. By taking the zeroth $\int(\,)d\vec{v}$ and first $\int \vec{v}(\,)d\vec{v}$ moments of Eq. (1.9), multiplying by 1 and m, respectively, and inserting the Lorentz force equation $\vec{F} = q/m\left(\vec{E} + \vec{v}\times\vec{B}\right)$ we obtain the continuity equation,

$$\frac{\partial \rho}{\partial t} + \nabla\cdot\left(\rho\vec{v}\right) = 0 \qquad , \tag{1.10}$$

and force balance equation,

$$\rho\left(\frac{\partial}{\partial t} + \vec{v}\cdot\vec{\nabla}\right)\vec{v} = \vec{j}\times\vec{B} - \vec{\nabla}p \quad , \tag{1.11}$$

where ρ is the mass density, $\vec{j}$ is the current density, and p is the kinetic pressure. Here the adiabatic closure is obtained by applying the thermodynamic pressure relationship of a monatomic ideal gas,

$$\frac{p}{\rho^{5/3}} = const. \tag{1.12}$$

A complete system of equations requires Maxwell's equations,

$$\vec{\nabla} \times \vec{E} = -\frac{\partial \vec{B}}{\partial t} \ , \tag{1.13}$$

$$\vec{\nabla} \times \vec{B} = \mu_0 \vec{j} \quad , \tag{1.14}$$

and Ohm's law,

$$\vec{E} + \vec{v} \times \vec{B} = \eta \vec{j} \ , \tag{1.15}$$

where η is the resistivity.

Equations (1.10) through (1.15) comprise a version of MHD equations useful in studying tokamak plasma dynamics. Variations on these equations are possible depending upon the closure chosen and assumptions made.

One example of how these equations are applied in tokamaks is in the establishment of a plasma equilibrium with respect to the applied and induced magnetic fields. The equilibria in tokamaks are static, meaning that the left hand side of the equation of motion, known as the inertial term, is zero. Also, high temperatures lead to low resistivity, causing the right hand side of Eq. (1.15) to approach zero. This leads to a 'flux-frozen' condition, where the particles of the plasma are locked to the magnetic field lines. This means the structure of the internal magnetic field is the same as the structure of the plasma, such that the two evolve together.

As will be discussed later in this work, numerous parameters related to the internal magnetic field structure can be directly measured. From the approximations mentioned above the force balance equation takes the form $\vec{\nabla} p = \vec{j} \times \vec{B}$ and is solved using measured data. An example equilibrium reconstruction, for the complicated elongated poloidal geometry of DIII-D, is shown in Fig. 1.2.1-1. This structural measurement is the backbone of all tokamak fusion research. It has enabled the development of sophisticated feedback control algorithms, which; shape the plasma into any number of possible non-circular poloidal cross sections, maintain vertical position, and alter the points at which open flux surfaces strike the machine floor with millimeter accuracy.

1.2.4 H-mode

Thus far, tokamaks boast the longest particle and energy confinement times of any magnetically confined device. This superior confinement is the primary reason tokamaks are the preferred device for producing burning plasma. However, the theory of tokamak transport is insufficient to provide a first principles predictive extrapolation[27]. For this reason empirical relationships have been determined using a database of discharges spanning multiple machines operated under a variety of conditions. The most cited of these scalings is the ITER89-P. This scaling was generated to extrapolate various parameters to aid in the 1989 design of ITER. The resulting scaling is given by Ref. 28,

$$\tau_E^{ITER89-P} = 0.048 I^{0.85} R^{1.2} a^{0.3} \kappa^{0.5} n^{0.1} B^{0.2} M^{0.5} P^{-0.5} \quad , \qquad (1.16)$$

where $\tau_E^{ITER89-P}$ has units of seconds, I is the plasma current (MA), R is the major radius (m), a is minor radius (m), κ is elongation, n is density (10^{20} /m^3), B is magnetic field strength (T), M is the isotopic mass of the ions (amu), and P is the total applied power (MW). It is important to notice that there is degradation in confinement associated with the applied power.

In 1982 an operating regime was discovered in the German tokamak ASDEX[29] that radically broke the P confinement degradation pattern of Eq. (1.16). A threshold neutral beam power was discovered beyond which particle and energy confinement times roughly double. This gave rise to an increase in both electron temperature and density, which together resulted in a factor of two larger poloidal beta. This can be seen in Fig. 1.2.4-1, where neutral beam power was increased from 1.6 to 1.9 MW between the two discharges. This new mode of operation was called high confinement mode, or H-mode, and has been duplicated in nearly every tokamak around the world.

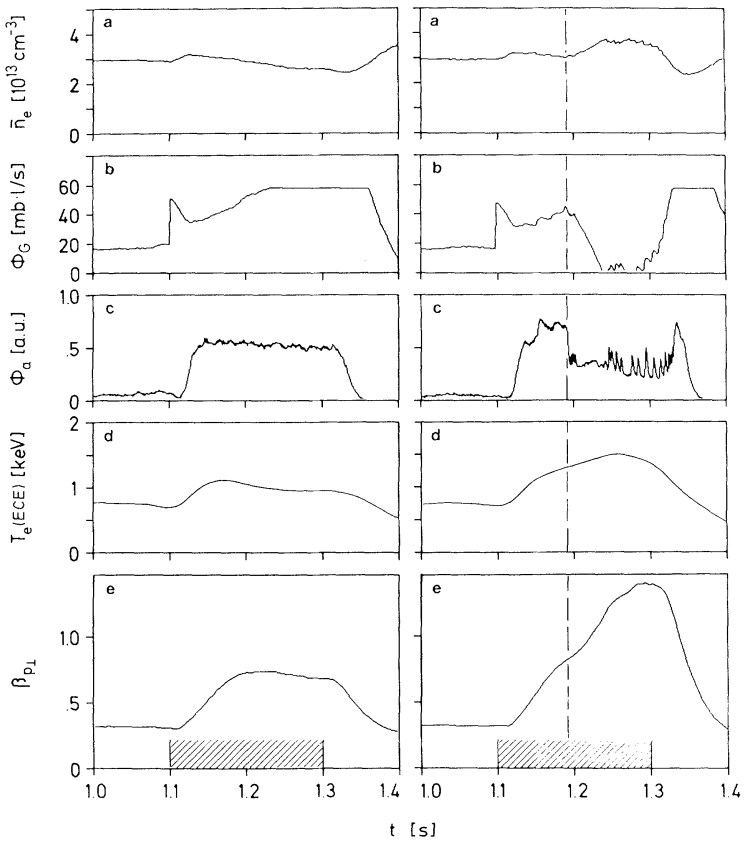

FIG. 1.2.4-1: Left: L-mode discharge with NBI power 1.6 MW. Right: H-mode discharge with NBI power 1.9 MW. (a) central electron density (b) feedback controlled gas injection (c) lost particle flux (d) central electron density (e) poloidal beta (Reprinted from Ref. 29)

It was later found that the improved confinement of H-mode was a consequence of the formation of an energy and density transport barrier in the outer edge of the plasma. This transport barrier[30] was found to be very steep only spanning ~10-15% of the minor radius. The original H-mode transport barrier is shown in Fig. 1.2.4-2 in comparison with the low confinement L-mode phase of the same discharge. This steep transport barrier is known as the pedestal.

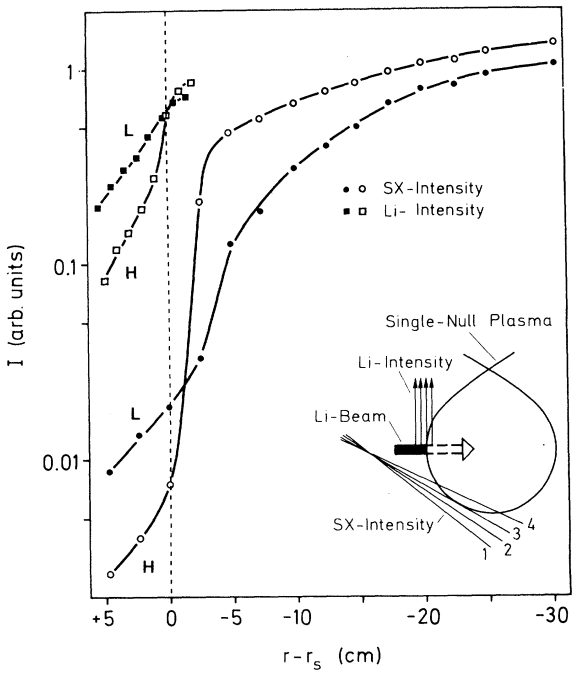

FIG. 1.2.4-2: First transport barrier identified to accompany the transition to H-mode. Soft x-ray temperature profiles of an L-mode and H-mode plasma. (Reprinted from Ref. 30).

Interestingly, once the H-mode transition occurs the L-mode scaling of Eq. (1.16) still applies, except the confinement times are larger by a constant factor. To characterize the quality of H-mode confinement an enhancement factor is introduced, which is a ratio of the energy confinement time of an H-mode discharge (τ_E^H) over the L-mode scaling energy confinement time (τ_E^L),

$$H = \frac{\tau_E^H}{\tau_E^L} \quad . \tag{1.17}$$

H-mode plasmas have inherent periodic particle exhausting events in the pedestal region known as edge localized modes (ELMs). ELMs allow particles to be exhausted while maintaining improved energy confinement. Unfortunately, in experiments big enough to generate commercial levels of power, some ELMs will produce prohibitively large heat loads on wall materials. ELMs will be discussed in more detail later in this work.

1.3 DIII-D National Fusion Facility

DIII-D[19] is a modest sized tokamak with R = 1.66 m and a = 0.67 m. It is capable of significant elongation ($\kappa \sim 2$), and has both upper and lower cryopumped divertors allowing for D-shaped plasmas to be created. The toroidal field can reach 2.2 T and plasma currents of up to 5 MA are possible, which permits a large range of possible current profiles to be obtained ($2 \leq q_{95}$). The machine is a pulsed device with copper, water cooled toroidal field coils. The pulses are 10 sec long. There are 16 MW of neutral beam power, 6 MW of ion cyclotron resonance heating, and 4 MW of electron cyclotron heating. A full-scale model of a poloidal cross-section of DIII-D is shown in Fig. 1.3-1. The device employs a state of the art plasma control system now being used in the recently commissioned Korean KSTAR[31] and Chinese EAST[32] tokamaks. DIII-D is very robust to disruption events due to a carbon tile armor lining inside of the vacuum vessel and an anti-torque outer structure. This has enabled unstable high performance discharges to be tested. To date, it has achieved deuterium plasma conditions sufficient to produce a Q = 0.32 if a 50/50 D-T mix were used[33]. There are over 50 diagnostics installed on the device[34], many of which are pioneering imaging measurements[35].

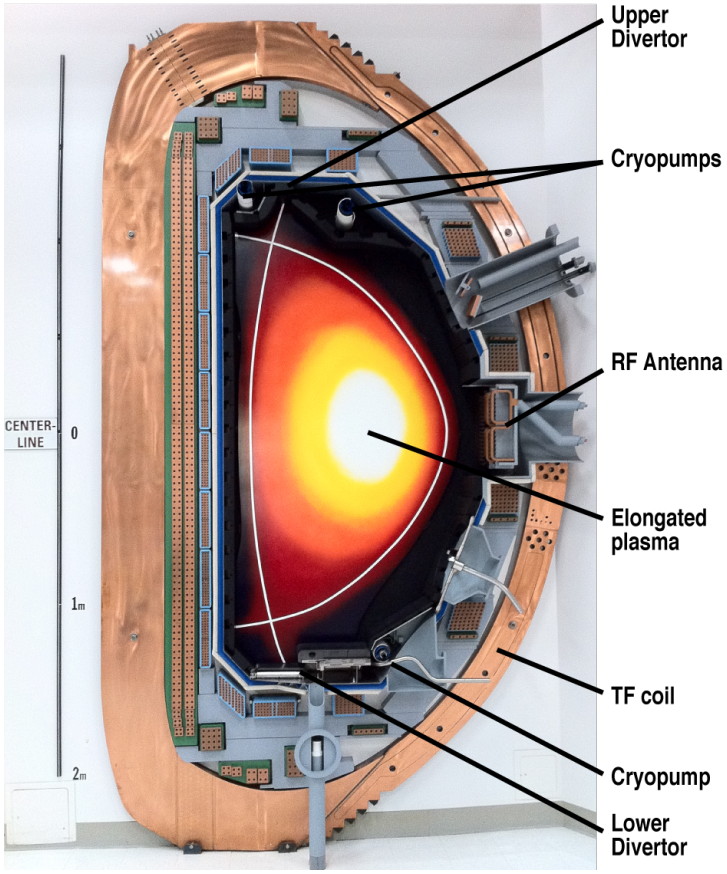

FIG. 1.3-1: A full-scale model of DIII-D, showing the upper and lower divertors, cryopumps, an RF antenna, a toroidal field (TF) coil, and the D-shaped elongated plasma.

1.4 Outline

The goal of the research presented in this dissertation was to extend the motional Stark effect diagnostic[36, 37] capabilities to include the study of MHD fluctuations for use in advanced tokamak scenario[38] development. Specifically, evidence for improved performance of the 'hybrid' discharge[39] scenario was found. In Chapter 2 the origins of tearing instabilities and other MHD phenomena are introduced providing a working vocabulary for the chapters to follow. Also, an outline of advanced tokamak research is provided focusing on the hybrid discharge and how it scales to ITER. The diagnostic tools, added hardware, and fluctuation analysis techniques are discussed in Chapter 3. Chapter 4 details the experimental results. Specifically, the first successful operation of the new hardware is shown, and instrument improvements, needed for pedestal current measurements, are presented. Also discussed in this chapter is evidence suggesting that a new higher performance hybrid regime may be possible. Concluding remarks and a discussion of future internal fluctuating magnetic field measurements are provided in Chapter 5.

Chapter 2

Theory

2.1 The Neoclassical Tearing Mode Instability

The current forefront of fusion performance research is focused on the passive or active avoidance of the neoclassical tearing mode (NTM) instability. Besides ideal magnetohydrodynamic (MHD) external kink limits,[40,41] the greatest determination of achievable fusion performance is dependent on a pressure driven resistive NTM instability[42]. The NTM degrades confinement, plasma rotation[43] and achievable beta. In cases where plasma rotation is sufficiently reduced major disruption events can occur, which cause the plasma thermal and magnetic energy to be lost to the wall in less than 10 ms.[44] These disruptions can significantly damage machine components and must be nearly completely avoided for success in ITER.

Existing experiments have shown that NTM instabilities can be efficiently controlled using electron cyclotron current drive (ECCD) directed at the instability[45]. In fact, active stability control using ECCD has both suppressed the NTM, once it has formed, and prevented it from forming in the first place. While isolated instances of success in this control have been found across numerous machines, no single experiment has succeeded in implementing control systems sufficient to eliminate NTMs from concern in day-to-day operations. Because of this, the onset of an NTM marks the fundamental beta limit of all scenario work.

Complicating matters is the fact that NTMs have advantageous impacts on fusion performance. As will be discussed later, a type of discharge known as the "hybrid" has been shown to benefit from the presence of an NTM.

2.1.1 Magnetic Islands

A magnetic field perturbation to equilibrium flux surfaces results in the formation of a helical structure known as a magnetic island. Magnetic islands are local static regions of plasma that have their own closed flux surfaces. These islands are located inside a larger plasma volume that contains a varying safety factor profile[46]. The islands last closed flux surfaces intersect at rational surfaces, where $q(\psi) = m/n$. The structure of the island can be found by documenting the point of intersection with a poloidal cross

section of a single field line as it makes many toroidal transits. Figure 2.1.1-1 shows an illustration of this poloidal cross cut.

FIG. 2.1.1-1: Poloidal cross-section showing three magnetic island chains (Reprinted from Ref. 46).

The origin of magnetic islands is explained by considering a magnetic field perturbation to an undisturbed plasma equilibrium. In this case the shape of the plasma can be described through the equation,

$$\vec{\nabla}\psi \cdot \vec{B} = 0 \tag{2.1}$$

since the gradient of the flux should always be perpendicular to the field. The following derivation of the magnetic island structure follows Ref. 11. By applying perturbations $\vec{B} = \vec{B}_0 + \vec{B}_1$ and the $\psi = \psi_0 + \psi_1$ to Eq. (2.1), expanding, and neglecting vanishing terms we have,

$$\vec{B}_0 \cdot \vec{\nabla}\psi_1 + \vec{B}_1 \cdot \vec{\nabla}\psi_0 = 0. \tag{2.2}$$

Carrying out the derivatives of Eq. (2.2) in toroidal coordinates and rearranging gives,

$$\frac{\partial \psi_1}{\partial \phi} + \frac{RB_{0\theta}}{rB_{0\phi}}\frac{\partial \psi_1}{\partial \theta} + \frac{R}{B_{0\phi}}\left(\vec{B}_1 \cdot \vec{\nabla}\psi\right)\frac{\partial \psi_0}{\partial \psi} = 0 \quad , \tag{2.3}$$

where ϕ is the toroidal angle, θ is the poloidal angle, r is the minor radius, and R is the major radius. In the large aspect ratio circular poloidal cross section approximation the safety factor is taken as[22],

$$q = \frac{rB_\phi}{RB_\theta} \quad . \tag{2.4}$$

By expressing both ψ_1 and $R/B_{0\phi}\left(\vec{B}_1 \cdot \vec{\nabla}\psi\right)$ as Fourier series, and substituting into Eq. (2.4), Eq. (2.3) can be rewritten as,

$$-\left(\sum_m \psi_m e^{im\theta}\right) ine^{-in\phi} + \left(\frac{1}{q}\sum_m \psi_m e^{-in\phi}\right) ime^{im\theta} + \left(e^{-in\phi}\sum_m b_m e^{im\theta}\right)\frac{\partial\psi_0}{\partial\psi} = 0 \quad , \qquad (2.5)$$

where,

$$b_m = \frac{e^{in\phi}}{2\pi}\int_{-\pi}^{\pi}\left(\frac{R}{B_{0\phi}}\vec{B}_1\cdot\vec{\nabla}\psi\right)e^{-im\theta}\,d\theta \quad . \qquad (2.6)$$

Since the equation must be satisfied for each individual term, the summation of Eq. (2.5) can be dropped and rewritten as

$$\psi_m = -\frac{iqb_m}{(nq-m)}\frac{\partial\psi_0}{\partial\psi} \quad . \qquad (2.7)$$

For this expression, when $q \to m/n$, $\psi_m \to \infty$. To avoid this we must use an expression for $\partial\psi_0/\partial\psi$ that is equal to zero at the rational surfaces. The expression chosen is,

$$\frac{\partial\psi_0}{\partial\psi} = \frac{\sin(n\pi q)}{n\pi(\partial q/\partial\psi)} \quad . \qquad (2.8)$$

Doing a Taylor expansion of q in terms of ψ flux coordinates and considering a region near the rational surface, the sinusoidal term of Eq. (2.8) can be expressed as,

$$\sin(n\pi q) = \pm n\pi\frac{\partial q}{\partial\psi}(\psi - \psi_m) \quad . \qquad (2.9)$$

Using this simplified expression, Eq. (2.8) can be integrated to give an expression for the equilibrium component of the flux as,

$$\psi_0(\psi) = \psi_0(\psi_m) \pm \tfrac{1}{2}(\psi - \psi_m)^2 \quad , \qquad (2.10)$$

and Eq. (2.7) can be written as,

$$\psi_m = \pm\frac{iqb_m}{n(\partial q/\partial\psi)} \quad . \qquad (2.11)$$

The perturbed flux component ψ_1 can be determined by substituting the Fourier series coefficients ψ_m of Eq. (2.11) into the original Fourier series, applying Euler's formula, and taking only the real terms to give,

$$\psi_1 = \pm\sum_m \frac{-qb_m\sin(m\theta - n\phi)}{n(\partial q/\partial\psi)}. \qquad (2.12)$$

A frequently occurring quantity can be redefined as,

$$\left(\frac{w}{4}\right)^2 \equiv \frac{qb_m}{n\left(\partial q/\partial\psi\right)} \quad . \tag{2.13}$$

To determine the structure of an island we combine Eq. (2.10), (2.12), and (2.13) to give the solution of the flux *function* ψ. By setting the values of the flux function to constant values ψ_C, and rearranging the expression to be in terms of the flux *coordinate* ψ, we have,

$$\psi = \psi_m \pm \sqrt{2}\,\frac{w}{4}\left[\psi_i + \sin\left(m\theta - n\phi\right)\right]^{1/2}, \qquad \psi_i = \frac{\psi_C - \psi_0(\psi_m)}{w^2/8} \quad . \tag{2.14}$$

An illustrative topographic plot of Eq. (2.14) is shown in Fig. 2.1.1-2. The dashed line is the seperatrix of the island. This surface divides the island's closed fluxes from the rest of the plasma, and occurs when $\psi_i = 1$. The point where the seperatrix touches the rational surface ψ_m is known as the X-point. The islands center is the O-point, and the full width of this region is *w* from Eq. (2.13). In the case where $\psi_i > 1$, the term under the radical of Eq. (2.14) is always positive for any angle $(m\theta - n\phi)$ so that the solution is a simple sinusoid outside of the seperatrix. Inside the seperatrix $\psi_i < 1$, means only certain angles $(m\theta - n\phi)$ have real solutions, such that islands are formed. In the example shown where $\psi_i = 0.5$, the solution is real only for $11\pi/6 < (m\theta - n\phi) < 19\pi/6$.

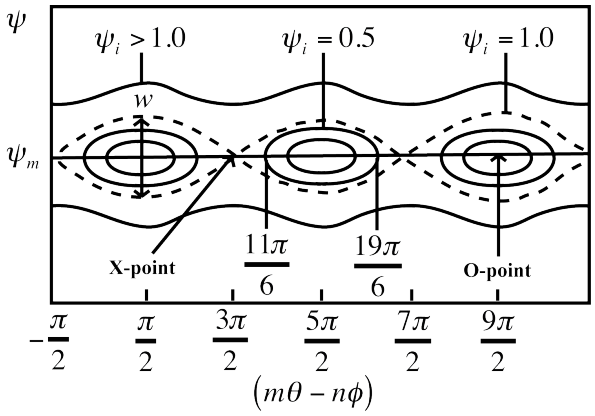

FIG. 2.1.1-2: Topographic plot of a magnetic island chain, using Eq. (2.14).

2.1.2 The Classical Tearing Instability

A radial gradient in the toroidal current density is locally unstable at rational surfaces resulting in magnetic reconnection. This tearing of magnetic field lines occurs because of finite resistivity effects that cause the formation of magnetic islands. To obtain an eigenfunction and eigenvalue growth-rate the MHD force balance equation must be solved both inside and outside the rational surface. Also, the solution to the ideal MHD region outside must match that of the narrow resistive layer at the rational surface[22]. The utility of this solution is limited as it only holds for narrow resistive layers that are too small to be measured. Nevertheless, this layer solution matching gives rise to a description of the flux discontinuity Δ' across the rational surface defined as,

$$\Delta' = \left.\frac{\partial\psi/\partial r}{\psi}\right|_{r=r_s-\varepsilon}^{r=r_s+\varepsilon} \quad . \tag{2.15}$$

This expression is known as the classical tearing stability index. The Δ' parameter is important to determining tearing stability and island growth.

Evaluating Eq. (2.13) from the previous section gives a relationship between island width and radial magnetic field B_r at the rational surface:

$$w \equiv 4\left(\frac{rqB_r}{m\left(\partial q/\partial\psi\right)B_\theta}\right)_{r_s}^{1/2} \quad , \tag{2.16}$$

The width of a tearing mode island is the primary property impacting global plasma parameters (e.g. stability, confinement). Here an expression will be obtained that describes the linear dynamics of the island width. This outline follows Ref. 22 and 46.

Starting from the precept that tearing reconnection produces a magnetic island, the growth of the island beyond the resistive layer and into the surrounding plasma can be described through magnetic diffusion. Only the radial magnetic field perturbation is appreciable such that the diffusion equation can be written as,

$$\frac{\partial B_r}{\partial t} = \frac{\eta}{\mu_0}\frac{\partial^2 B_r}{\partial r^2} \quad , \tag{2.17}$$

where η is resistivity. Integrating Eq. (2.17) across the island width, and because Eq. (2.16) shows $B_r \propto w^2$, the following approximation can be written:

$$\frac{dw}{dt} \approx \frac{\eta}{2\mu_0}\frac{1}{B_r}\left.\frac{\partial B_r}{\partial r}\right|_{r_s-w/2}^{r_s+w/2} \quad . \tag{2.18}$$

Applying the definition of the radial magnetic field $B_r = -(1/r)\partial\psi/\partial r$ to the helically perturbed flux function $\psi = \psi e^{(im\theta - in\phi)}$ gives the perturbed field in terms of flux $B_r = -im\psi/r$. Substituting this into Eq. (2.18) gives,

$$\frac{dw}{dt} \approx \frac{\eta}{2\mu_0} \frac{\partial\psi/\partial r}{\psi}\Bigg|_{r_s - w/2}^{r_s + w/2} \quad , \tag{2.19}$$

From Eq. (2.15) it appears that Δ' can be substituted into the right side this expression. By plugging the definition of the resistive diffusion time ($\tau_R = \mu_0 r^2/\eta$) into Eq. (2.19) we arrive at the Rutherford equation describing the classical evolution of a tearing mode. This equation is written as,

$$\frac{\tau_R}{r^2}\frac{\partial w}{\partial t} = \Delta' \quad . \tag{2.20}$$

It can be seen from this expression that when $\Delta' > 0$ the island grows, and when $\Delta' < 0$ it shrinks. Because Δ' is considered constant the island evolves linearly. As will be shown in the next section, the size of the island can itself impact Δ'.

2.1.3 The Modified Rutherford Equation

While the groundwork has been laid for tearing mode studies, Rutherford required revision. Experimentally tearing modes are observed even when they are classically stable ($\Delta' < 0$). The oversight of Rutherford was a failure to consider the impact of bootstrap current on tearing stability.

Bootstrap current density j_{bs} is independent of ohmically driven current from the tokamak central solenoid. It originates from radial particle diffusion. The intrinsic nature of this current gives rise to it's name "bootstrap". This current can be approximated as follows,

$$j_{bs} \approx -\frac{\varepsilon^{1/2}}{B_\theta}\frac{dp}{dr} \quad , \tag{2.21}$$

where $\varepsilon = r/R$ is the local inverse aspect ratio and dp/dr is the radial pressure gradient. Since the plasma pressure at the wall of the machine must be zero, j_{bs} increases as plasma pressure increases.

A key observation, discussed in the next section, is that magnetic islands flatten the pressure profile around the rational surface. Thus, a small "seed" magnetic island will generate a local absence in j_{bs}. This helical perturbation to the bootstrap current density will reinforce itself, causing the "seed" island to grow. These neoclassical effects

must be included in the description of tokamak tearing instability. The Rutherford equation, including a destabilizing neoclassical correction term, takes the form,

$$\frac{\tau_R}{r^2}\frac{dw}{dt} = \Delta' + \varepsilon^{1/2}\frac{L_q}{L_p}\frac{\beta_p}{w} \quad , \tag{2.22}$$

where $L_q = q/(\partial q/\partial r)$ and $L_p = -p/(\partial p/\partial r)$ are the pressure gradient length and magnetic shear length, respectively, β_p is the ratio of kinetic pressure to poloidal magnetic pressure, and Δ' is the classical stability index. This equation is known as the modified Rutherford equation (MRE).[26, 42]

It can be seen that as w increases the destabilizing neoclassical term decreases. This means, for constant Δ', a point is reached where the stabilizing Δ' term is balanced by the destabilizing neoclassical term. This no growth condition is known as island saturation.

2.1.4 The Belt Model and Energy Confinement

Heat can diffuse rapidly across a magnetic island, resulting in global energy confinement degradation[47]. Instead of heat diffusing through the volume occupied by the island, it passes around the X-point. In other words, the smaller path length of the island seperatrix removes the thermal insulation of the equilibrium. This can be roughly described using a 'belt' model.

In the 'belt' model the island effect on confinement can be approximated as a flattening of the temperature profile across the full width of the island. Figure 2.1.4-1 illustrates the temperature profiles for a plasma with ($T(r)$) and without ($T_0(r)$) a magnetic island present.

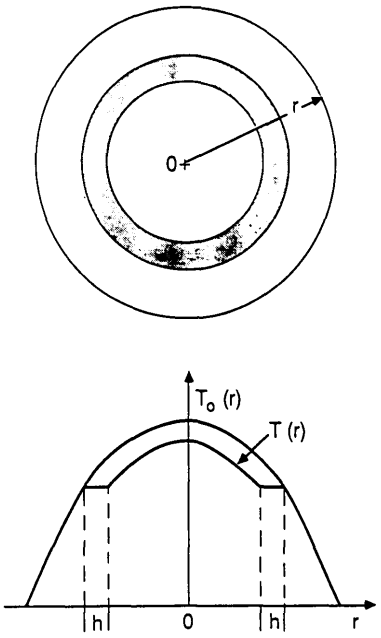

FIG. 2.1.4-1: The belt model of a magnetic island. Top – poloidal cross-section of a circular tokamak plasma r is minor radius. Bottom – $T_0(r)$ is the temperature profile without an island, $T(r)$ is the profile with the island. h is the belt width, and is equivalent to w for our purposes. (Reprinted from Ref. 47)

The one-fluid energy balance equation can be written as,

$$3\frac{\partial(nT)}{\partial t} = -\nabla\cdot\left(n\chi\vec{\nabla}T\right) + Q \quad , \tag{2.23}$$

where n is density, T is temperature, χ is radial heat diffusivity, and Q is the difference between energy sources and sinks. This expression gives the energy per unit volume. If the n, χ, and Q profiles are known, then the total stored energy can be determined by integrating Eq. (2.23) over the full plasma volume. The energy confinement time is defined as the stored energy divided by the input power ($\tau = W/P_{in}$).

The fractional degradation in the energy confinement due to an NTM is approximated using the above definition of τ. First, τ is calculated using n, χ, and Q profiles for a plasma free of MHD. The 'belt' model assumes the island causes the temperature profile to be flat across the full width, which is equivalent to assuming that the heat diffusion in the island region is infinite. Only modifying χ to fit this assumption, τ can be recalculated for a plasma containing an NTM. Taking a ratio of these two confinement times gives,

$$\frac{\tau_{inc}}{\tau_{inc0}} = 1 - \frac{4r^3 w}{a^4} \quad , \tag{2.24}$$

where τ_{inc} and τ_{inc0} are the incremental energy confinement time with and without a tearing mode respectively, r is again the minor radius of the rational surface, w is the full

magnetic island width, and a is the plasma minor radius. It can be seen from this expression that the larger the island width the greater the confinement degradation. However, the far more important factor is the location of the rational surface, which scales as the cube of r.

2.2 The Edge Localized Mode

Edge localized modes (ELMs) are ideal MHD instabilities[48] that develop near the pedestal of H-mode discharges. They are poloidally and radially localized filamentary structures that trace a field line in the plasma edge. ELMs originate on the low field side of the machine and grow in tens to hundreds of μs. These bursty instabilities are analogous to solar flares[49]. Each ELM event rapidly transports energy and particles from the top of the pedestal to open flux surfaces of the scrape off layer[50]. This has a benefit of exhausting impurities from the closed flux of the core plasma to the divertor region for pumping. Unfortunately because of their eruptive nature, ELMs can produce large heat fluxes on divertor materials[51]. In ITER the largest ELMs are expected to exceed material design thresholds over a single discharge.

Attempts have been made to suppress ELMs without degrading H-mode properties. For instance, the application of static magnetic fields using internal coils, known as resonant magnetic perturbations[52] (RMP), eliminates large ELMs. This is because the applied field generates stochastic field lines within the edge-pedestal region that effectively dampen the rapid ELM energy transport[53]. Application of the RMP does come at the expense of reduced plasma rotation, which in turn diminishes global stability. At present, RMP internal coils are included in the ITER design.

Theoretical and experimental studies have found that ELMs are best described as intermediate n ($3 < n < 20$) coupled peeling-ballooning modes[54] and that modifications in plasma shape can achieve high pedestal conditions while the size and frequency of ELMs is maintained small enough to be within the material tolerances of the divertor tiles. The Edge Localized Instabilities in Tokamak Experiments (ELITE) MHD stability code[54] has extended this understanding to identify the regions of stability. These stability regions are shown in Fig. 2.2-1. Peeling modes are stabilized by steep pedestal pressure gradients (p'_{ped}) and destabilized by pedestal currents (J_{ped}). The opposite is true for ballooning modes. Note, a constant pedestal width was maintained in generating Fig. 2.2-1 such that an increase in the pressure gradient results in a higher pedestal. For this reason the optimum performance regime lies at the peak of the stability curve just beyond the peeling unstable region and just inside of the ballooning unstable region. Furthermore, Fig. 2.2-1(a) shows how plasma shaping extends the stability region of both peeling and ballooning modes toward regions of higher performance.

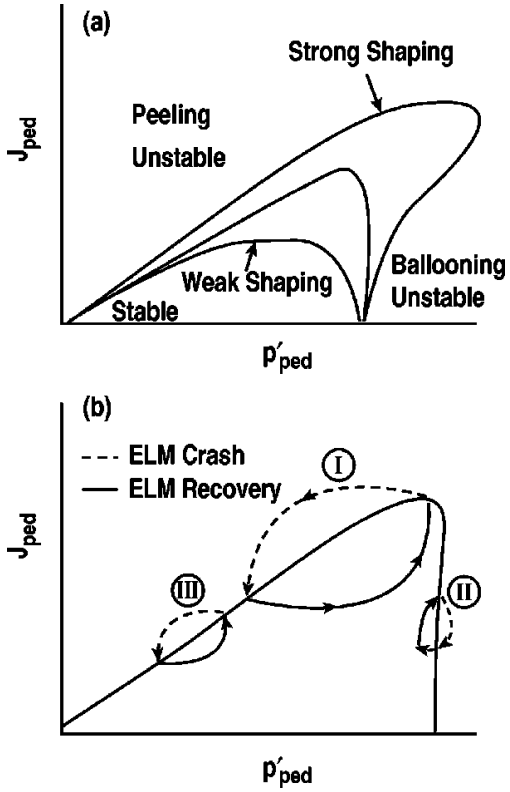

FIG. 2.2-1: (a) ELM stability regions in pedestal current – pressure gradient space (b) Characterization of ELMs into types I, II, and III (Reprinted from Ref. 54)

ELMs are categorized as type I, II, and III. Type I ELMs are the largest and therefore most damaging to divertor materials. Type II and III are significantly smaller and therefore preferred in future experiments. The size of the ELM is dependent on the radial depth of the most unstable mode[54]. Ballooning modes are of higher order and are disturbed in a narrower region of the edge than peeling modes and therefore produce smaller ELMs. This can be heuristically understood considering Fig. 2.2-1(b). First note that there is a difference between the recovery timescales of J_{ped} and p'_{ped}. As an example consider the type I ELM. A relatively high p'_{ped} causes the bootstrap current, and therefore J_{ped}, to slowly rise until it becomes peeling unstable. This causes a rapid drop in the pedestal gradient[55], but because of low collisionality the bootstrap current slowly drops until the stability region is reached. Once in this region, auxiliary heating and rapid energy transport quickly replenish the pedestal to it's original height and the process repeats.

Measurements of ELM properties are achieved through a variety of diagnostics. The preferred diagnostic for ELM identification is the filterscope. This diagnostic optically filters light emissions to only measure thermal D-α line emissions. They are focused at a number of locations around the divertor strike points. By detecting the filtered light intensities, ELMs impacting the divertor tiles are observed. A sample measurement of these characteristic ELM spikes is shown in Fig. 2.2-2.

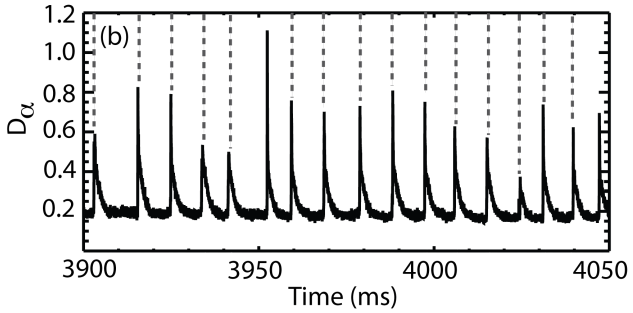

FIG. 2.2-2: Thermal D-α intensity measurement for an ELMing H-mode discharge.

2.3 Sawteeth

A discharge is unstable to sawteeth when a q = 1 rational surface is generated. Imaging diagnostics[56], as well as magnetic probe measurements, have revealed a m/n = 1/1 structure for this instability.

This instability is characterized by oscillations in the density, temperature and current profile. An example of this oscillating phenomenon is shown in Fig. 2.3-1. Because of heat conduction, the center temperature of a tokamak is disproportionately larger than the outer region. Since plasma conductivity is proportional to $T_e^{3/2}$, for a constant externally applied field the current profile inside a tokamak tends to be peaked toward the center. Since the applied toroidal field is maintained constant, this increased central current results in a decrease in the center safety factor $q \equiv d\Phi/d\psi$. Once the safety factor reaches unity, a 1/1 instability is triggered and grows rapidly (~100 μs). The growth results in a collapse of core confinement, which causes the central temperature and density to be transported to the outer plasma region. This results in the inverted temperature behavior about the 1/1 rational surface seen in the soft X-ray signals of Fig. 2.3-1. Because of the change in temperature profile the center current drops, and in some cases q increases above one, causing the growth of the mode to be halted. This effectively flattens the current and safety factor profiles. The center current then again begins to slowly increase (tens of ms) on a resistive timescale (τ_R) and the process repeats. The rapid collapse and slow recovery produce a central temperature time trace resembling the teeth on a handsaw blade, hence the name 'sawteeth'. Note, the preceding explanation of sawteeth oscillations is not complete. Discharges have been reported with minimum safety factors less than 1 throughout numerous sawteeth oscillations, and the precise physical reason for this phenomenon is still an active area of investigation.

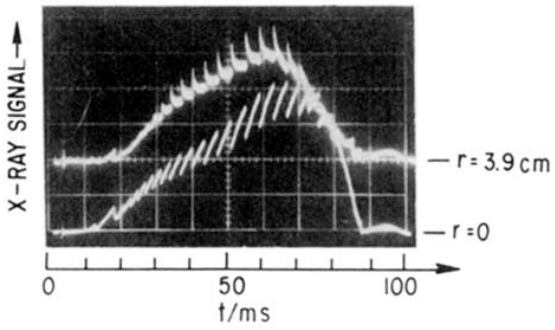

FIG. 2.3-1: Bottom trace is the center temperature, and top trace is the edge temperature of a sawtoothing discharge from the ST tokamak. (Reprinted from Ref. 57)

Even though the center heat is transported to the edge of the plasma and not to the outer wall, the overall energy confinement is degraded by sawtooth oscillations. This is primarily a consequence of the edge heat diffusivity being much larger in the edge than the core, such that once the sawtooth transports the core heat to the edge it more easily propagates out of the plasma. A similar 'belt' model analysis as was discussed for the tearing mode shows that sawteeth degrade confinement by about 17%.[47]

2.4 Advanced Tokamak Physics

Two goals of ITER are the demonstration of $Q \geq 10$ inductive ELMy H-mode discharges, and non-inductive $Q \sim 5$ steady state discharges. Advanced tokamak research is aimed at bridging the gap between these two modes of operation, as well as pushing performance of inductive discharges toward ignition[38]. Both of these endeavors require improved confinement and larger normalized beta.

The H-mode ITER scenario intends to create a 400 s burn time with $q_{min} < 1$ and $q_{95} \sim 3$. It is a pulsed discharge, meaning that the duration of the discharge is technologically limited by the available inductive flux of the superconducting central solenoid. These discharges will have the highest plasma current at 15 MA. There is confidence in the empirical extrapolation of this scenario to ITER, since H-mode has the largest database of available discharges across multiple machines.

The focus of steady state operation is to sustain the plasma current non-inductively, thereby extending the discharge length indefinitely. However, for practical reasons these discharges will be limited to about 3600 seconds. Initiation of a steady state discharge still relies on the toroidal electric field of the central solenoid. However, once a current flat top is reached the voltage across the coil terminals is dropped to zero. The safety factor will be non-monotonic with $q_{min} \sim 2.5$ and $q_{95} \sim 5.5$. By reversing the gradient of the safety factor near the mid-minor radius an internal transport barrier is established[58]. This transport barrier is required to improve confinement and normalized beta beyond that found in the inductive H-mode scenario. Furthermore, cyclic steady state scenarios are being studied in which the center solenoid may be recharged throughout the discharge using neutral beam current drive[59].

Within the realm of advanced tokamak research is the advanced-inductive 'hybrid' discharge. Part of the aim of this scenario is to extend the $Q \sim 10$ pulse length of inductive H-mode to ~1000 seconds. To do this, roughly half of the plasma current must be non-inductive and/or bootstrap. The current profile of these discharges are relatively flat in the core with $q_{min} \sim 1$ and q_{95} between 3.2 and 4.5. Furthermore, a hybrid requires active control of normalized beta. This relies on neutral beam actuators and indirectly allows for the bootstrap current to be maintained constant.

2.4.1 Stationary Hybrid Discharges

Hybrid discharges with more than 50% non-inductively driven plasma current have been realized in ASDEX-U[60], JET[61], JT-60U[62], and DIII-D[39] tokamaks. Beyond high performance, all plasma parameters have been maintained stationary for timescales greater than the current relaxation time (τ_R). In almost all cases, a neoclassical tearing mode (NTM) is present throughout the stationary phase of the discharge.

Hybrids are considered in two camps. The first has $q_{95} > 4$ and is stable to sawteeth. The other has $q_{95} \sim 3$ with sawteeth throughout the stationary phase of the discharge. In both cases 3/2 NTMs are present.

For $q_{95} > 4$, it has been found that the 3/2 NTM is required to avoid sawteeth[63]. Specifically, suppressing the NTM after it has formed leads to sawteeth. Further analysis has revealed that pumping of magnetic flux from the core to the edge is maintaining the minimum safety factor above unity[64]. This magnetic flux-pumping is associated with coupling between ELMs and the 3/2 NTM and will be described in more detail later.

Although counter-intuitive, the greatest performance has been found in discharges with multiple core MHD instabilities present. Specifically, the additional current of the $q_{95} \sim 3$ case has the highest performance, despite having both sawteeth and a 3/2 tearing instability. Recall $q_{95} > 4$ discharges only contain 3/2 tearing modes.

2.4.2 Normalized Fusion Performance

Evaluation of fusion performance across multiple machines requires a dimensionless quantity for comparison and extrapolation to ITER. Recall, the definition of fusion gain Q from the introduction chapter. The triple product $nT\tau$ is proportional to both the equivalent fusion gain for D-D plasmas (Q_{DT}^{E0}) and the ratio of α power to lost power (P_α / P_{loss}). Because one fifth of the energy for a D-T fusion reaction is carried by the α particle the total fusion power can be written as $P_{fus} = 5P_\alpha$. Using this expression, Eq. (1.2) of Chapter 1 can be rewritten as,

$$\frac{P_\alpha}{P_{loss}} = \frac{Q}{(Q+5)} \propto nT\tau \quad . \tag{2.25}$$

A comparison between deuterium only machines, where no appreciable α heating is present, and D-T devices requires Eq. (2.25) to be rewritten in terms of dimensionless parameters. By definition it is known that $nT \propto \beta_N I$. From numerous empirical scalings[65, 28] it is known that $\tau \propto HI$, where H is a dimensionless enhancement factor describing the increase in energy confinement resulting from H-mode vs. L-mode operation. The edge safety factor is inversely proportional to the plasma current $q_{95} \propto 1/I$. Combining these proportionality expressions Eq. (2.25) can be rewritten as,

$$nT\tau \propto \frac{\beta_N H}{q_{95}^2} \equiv G \qquad , \tag{2.26}$$

where G is the normalized fusion performance parameter. Note that this expression is written in terms normalized variables that can be advanced through improved physics understanding. In other words, no technological constraints (e.g. field strength B) appear in the expression.

In the DIII-D tokamak, hybrids have achieved normalized fusion performance in excess of that required to reach the inductive H-mode goal of Q =10 in ITER. For these studies the confinement enhancement factor H_{89P} was used in Eq. (2.26). This factor is the enhancement compared with the ITER 1989 L-mode energy confinement scaling[66].

Chapter 3

Diagnostics

3.1 The Motional Stark Effect Diagnostic

The motional Stark effect diagnostic (MSE) has become one of, if not the most important diagnostic to advanced tokamak research. Its utility is applicable to any high field fusion energy experiment containing a neutral beam. From active suppression of tearing modes, to general stability current profile studies, to non-inductive steady state experiments, detailed internal current profile measurements are indispensable. The only proven technique, currently with 22 years of development, is a polarimeter measurement of the Stark spectrum. While other techniques involving spectroscopic analysis of the Stark spectrum are showing progress, it is likely that the polarimeter measurement will remain the primary method for determining internal current profile structure in the foreseeable future.

3.1.1 Atomic Physics

In DIII-D, neutral beams inject deuterium atoms at energies of 81 kV into the bulk plasma. These neutrals are atomically excited to higher energy states through collisions with the electrons and ions. The excited atoms pass through the strong internal magnetic field causing them to experience a Lorentz electric field $\vec{E} = \vec{v} \times \vec{B}$. For a 2T magnetic field the amplitude of the local electric field is ~5500 kV/m. This electric field causes the D-α, n = 3 to n = 2 atomic transition to be split into nine observable components. The three $\Delta m = \pm 1$ transitions are known as σ emissions and have a polarization angle that is parallel to the internal magnetic field (perpendicular to the electric field). The six $\Delta m = 0$ transitions are called π emissions and are oriented perpendicular to magnetic field (parallel to the electric field). Due to thermal Doppler broadening the individual transitions are not distinguishable. Instead, the three σ components produce a single peak and the three higher and three lower energy transitions of the π components produce two peaks on either side of the σ emission with ~3 to 5 Å separation. An atomic transition diagram is shown for reference in Fig. 3.1.1-1.

The ion source of the neutral beam produces monatomic, diatomic, and triatomic singly charge ions (D^+, D_2^+, and D_3^+). These ions are then accelerated over a series of

grid voltage drops. The extra mass of the D_2^+ and D_3^+ ions result in one half and one third the energy of atomic deuterium, respectively, and are also shown in Fig. 3.1.1-1. Beyond Stark splitting, the relative velocity of the neutrals, with respect to the MSE optics viewing position, causes either blue of red Doppler shifts. This separation of the unpolarized thermal D-α emissions from the Stark split spectrum is critical to producing high signal-to-noise polarization measurements. Figure 3.1.1-2 shows all 5 polarimeter views on DIII-D. It can be seen that the polarimeter viewing the 30^0 beam from the 315^0 port is in a blue shift orientation. The corresponding Doppler shifted spectrum for these channels is illustrated in Fig. 3.1.1-1.

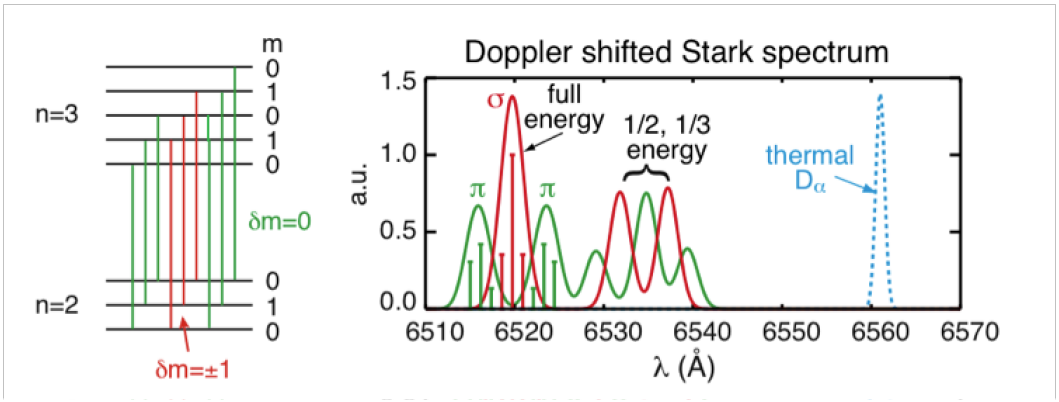

FIG. 3.1.1-1: The atomic transitions and Stark split spectrum for a single blue shifted MSE channel (Reprinted from Ref. 67).

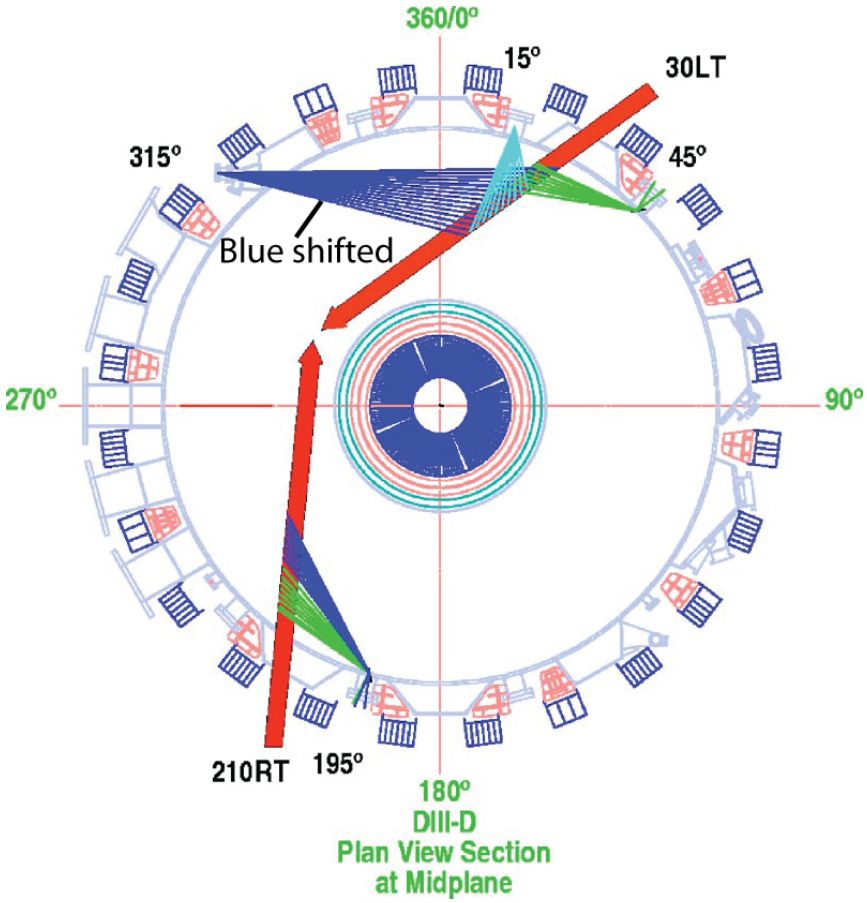

FIG. 3.1.1-2: Cross section of DIII-D showing 5 MSE polarimeters and their corresponding neutral beams. The blue shifted MSE system located in the 315^0 port is highlighted (Reprinted from Ref. 68).

3.1.2 Detection and Narrowband Optical Filtering

During a discharge the DIII-D machine hall experiences a large ionizing radiation field due to neutron production from fusion reactions and gamma decay of activated machine components. Because the light detectors of the MSE are sensitive to this radiation, a shielded detection room is used. The light from the machine hall is fiber optically coupled to this separate detection room. This light is collimated, passed through an optical filter, and then focused onto the photo cathode of a photomultiplier tube (PMT).

The MSE measures the linear polarization angle of the full energy σ light emissions to determine the direction of the internal magnetic field. To achieve this, 3 Å wide narrowband optical filters are employed. The peak transmission of these optical filters is typically greater than 55%, and the transmission curves can be approximated as a Gaussian. Since there is a different Doppler shift for each channel, unique narrowband filters with centroid wavelengths matching the peak σ emissions must be selected.

The centroid wavelength of each MSE channel is approximated using in-vessel geometry measurements and well-known neutral beam energy values. The actual centroid wavelength may be several Å different from those computed due to, among other things, unaccounted for vacuum vessel stress deformations that alter the MSE chord intersection with the beam line. To account for these errors, a library of optical filters is maintained with differences in centroid wavelength of less than 3 Å. For the ~3 Å bandpass of each filter, this results in a nearly complete coverage of the possible σ centroid wavelengths.

Even with a variety of filters to choose from, fine-tuning of the central σ wavelength to overlap the peak transmission is necessary. This is because the signal-to-noise ratio of the measurement is proportional to $\sqrt{I}$, where I is the light intensity at the detector. Because the polarization of the σ and π light is orthogonal, the detected light intensity is dependent on the difference between their individual intensities. This is further explained in the sections to follow.

The fine-tuning is achieved by tilting the filters relative to the direction of collimation. The larger the tilt angle (θ) of a filter, the greater the filter centroid wavelength (λ_0) will blue shift. This can be described as[69],

$$\lambda(\theta) = \lambda_0 \sqrt{1 - \left[\frac{N_{ext}\sin(\theta)}{N_{eff}}\right]^2} \quad , \tag{3.1}$$

where N_{ext} is the external medium refractive index, N_{eff} is the refractive index of the filter, and λ is the centroid wavelength after tilting. It should be noted that the peak transmission decreases and the width of the passband increases as the filter is tilted. It is therefore desired to select a filter that requires minimal tilting.

The procedure for determining the correct filter, and tilt angle for each channel involves scanning a number of filters roughly $\pm 10^0$ while measuring the amplitude of the MSE signal. The signal strength is determined using lock-in amplifiers, which will be described in more detail later in this chapter. For now the lock-in output can be thought of as signal strength. These scans are preformed using very repeatable plasma discharges with nearly constant density profiles. A simple lever arm is connected to a slowly oscillating bar (~0.5 Hz). The tilt angle is measured using a position sensitive potentiometer. Only two full sweeps of the filter angles are possible, due to the finite pulse length of the neutral beam.

A few sample filter scan results are shown in Fig. 3.1.2-1. When the filter centroid wavelength is on the blue side of the σ emission, no angle can be swept that will allow it to overlap the σ peak of the Stark spectrum. This scan will yield a Gaussian shaped curve, and is considered a "low" wavelength case. A "high" wavelength case results in a pronounced dip in the scan as the filter is starting at such a high wavelength that only at the extreme filter angles is the filter blue shifted enough to reach the peak of the Stark spectrum. This case is not preferred because the peak transmission decreases at large angles. A "tunable" filter is one where the scan of the filter yields only a slight dip in the center, allowing a small tilt angle to be used to match the peak σ emission. In the "ideal" case a filter has a center wavelength that is exactly the same as the peak of the

Stark spectrum. In this case the scan yields a region of near flatness at the top with no dip in the center.

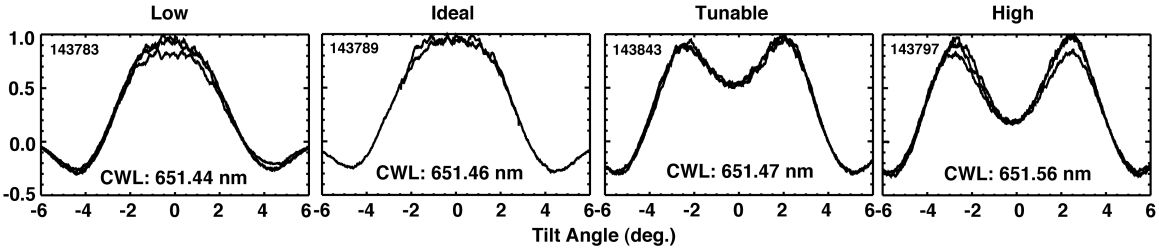

FIG. 3.1.2-1: Optical filter scans showing low, ideal, tunable, and high centroid wavelengths.

3.1.3 Stokes Parameters

Measuring the polarization of individual photons is not technologically feasible. For the polarization of light to be observable, average values of many photons must be considered. In other words, the intensity of light must be considered as opposed to the amplitudes of the individual electric field components. Through the measurement of four Stokes parameters (intensities) any polarization state can be measured. The following explanation follows Ref. 70.

The electromagnetic wave equation[71] can be written as,

$$\nabla^2 \vec{E} = \frac{1}{c^2}\frac{\partial^2 \vec{E}}{\partial t^2} \quad , \tag{3.2}$$

where $\vec{E}$ is the electric field vector and c is the speed of light. Solving the wave equation for a plane wave gives a solution for the electric field vector in both the x and y direction as follows,

$$E_x(t) = E_{0x}\cos(\omega t + \delta) \text{ , and } E_y(t) = E_{0y}\cos(\omega t + \delta) \text{ ,} \tag{3.3}$$

where E_{0x} and E_{0y} are the electric field amplitudes, $E_x(t)$ and $E_y(t)$ are the rapidly oscillating fields as the light propagates, ω is the frequency of the light oscillations and δ is the difference in phase between the x and y components. Combining these expressions and rearranging, we can write the solution to the wave equation as the elliptical polarization expression taken as,

$$\frac{E_x^2(t)}{E_{0x}^2} + \frac{E_y^2(t)}{E_{0y}^2} - \frac{2E_x(t)E_y(t)}{E_{0x}E_{0y}}\cos\delta = \sin^2\delta \quad . \tag{3.4}$$

This expression can be rewritten, now considering a rotated ellipse with new axis x' and y' oriented along the semi-major and semi-minor axis. This is shown in Fig. 3.1.3-1. A polarization angle γ is introduced that defines the angle between the old and new coordinate systems. After a number of trigonometric expansions and algebra Eq. (2.4) can be rewritten as,

$$\tan(2\gamma) = \frac{2E_{0x}E_{0y}\cos\delta}{E_{0x}^2 - E_{0y}^2}, \tag{3.5}$$

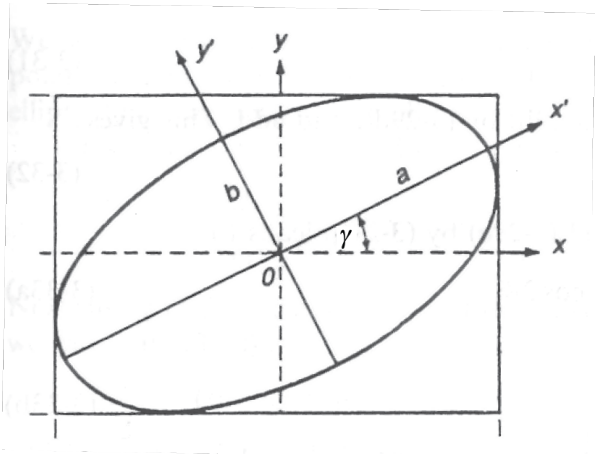

FIG. 3.1.3-1: The polarization ellipse and new coordinate system (Reprinted from Ref. 70).

Within Eq. (3.4) are the rapidly oscillating, immeasurable terms $E_x^2(t)$, $E_y^2(t)$ and $E_x(t)E_y(t)$. Recall, each of the terms is defined in Eq. (3.3). Averaging these terms over a large time interval relative to the femtosecond period of light oscillations gives,

$$\left\langle E_x^2(t)\right\rangle = \frac{1}{2}E_{0x}^2 \text{ , } \left\langle E_y^2(t)\right\rangle = \frac{1}{2}E_{0y}^2 \text{ , and } \left\langle E_x(t)E_y(t)\right\rangle = \frac{1}{2}E_{0x}E_{0y}\cos\delta \text{ .} \tag{3.6}$$

Plugging these average terms of Eq. (3.6) into the polarization ellipse expression of Eq. (3.4) and rearranging we have,

$$\left(E_{0x}^2 + E_{0y}^2\right)^2 = \left(E_{0x}^2 - E_{0y}^2\right)^2 + \left(2E_{0x}E_{0y}\cos\delta\right)^2 + \left(2E_{0x}E_{0y}\sin\delta\right)^2. \tag{3.7}$$

This expression completely describes the polarization state in terms of measureable intensities ($I \propto E^2$). Each term in Eq. (3.7) is a Stokes parameter. Equation (3.7) can therefore be rewritten as,

$$S_0^2 = S_1^2 + S_2^2 + S_3^2. \tag{3.8}$$

All four Stokes parameters are referred to as a Stokes vector. The Stokes vector is equivalently defined in complex notation as,

$$
\begin{aligned}
S_0 &= E_x E_x^* + E_y E_y^* \\
S_1 &= E_x E_x^* - E_y E_y^* \\
S_2 &= E_x E_y^* + E_y E_x^* \\
S_3 &= i\left(E_x E_y^* - E_y E_x^*\right)
\end{aligned}
\tag{3.9}
$$

Measurement of the Stokes parameters requires four measurements involving only three optical components. The equipment includes a quarter-wave retarder, a linear polarizer, and a detector. The first three measurements involve only the linear polarizer and detector, and require a measurement with the angle of the polarizer at 0^0, 45^0, and 90^0. The final measurement requires the polarizer to be set to 45^0 with the quarter-wave retarder in the optical path. Each of these measurements is expressed as $I(\theta,\phi)$, where θ is the polarizer angle, and ϕ is the retardance. The Stokes parameters are measured as,

$$
\begin{aligned}
S_0 &= I\left(0^0,0^0\right) + I\left(90^0,0^0\right) \\
S_1 &= I\left(0^0,0^0\right) - I\left(90^0,0^0\right) \\
S_2 &= 2I\left(45^0,0^0\right) - I\left(0^0,0^0\right) - I\left(90^0,0^0\right) \\
S_3 &= 2I\left(45^0,90^0\right) - I\left(0^0,0^0\right) - I\left(90^0,0^0\right)
\end{aligned}
\tag{3.10}
$$

Recalling the linear polarization angle given by Eq. (3.5) and the definition of the Stokes parameters given by Eq. (3.7) and (3.8) we see that γ can be expressed as,

$$
\tan(2\gamma) = \frac{S_2}{S_1} \quad . \tag{3.11}
$$

The MSE diagnostic measures this linear polarization angle, which is oriented parallel to the direction of the internal magnetic field.

3.1.4 Dual Photoelastic Modulator Mueller Matrices

To describe a dual photoelastic modulator (PEM) polarimeter[72] we must introduce the Mueller matrix formalism[73, 74]. The polarization state of an incident beam is changed when it interacts with matter. A Meuller matrix is a transfer matrix that describes this change in polarization associated with a material. Specifically, the emergent beams Stokes vector S' can be described as a linear combination of the incident beams Stokes vector S. The Mueller matrix is a 4×4 matrix containing the coefficients of this linear combination. The equation describing the material effect on the incident beam takes the form,

$$S' = M \cdot S \quad . \tag{3.12}$$

The primary optical polarization elements are diattenuators (or polarizers), rotators, and retarders. A diattenuator unequally attenuates the orthogonal x and y components of the electric field vectors of a beam. A rotator rotates the angle of polarization. The phase of the x component of the field vector is shifted with respect to the phase of the y component in the case of a retarder. Writing these terms explicitly in terms of their effect on the electric field vector we have,

$$\begin{array}{lll} E'_x = p_x E_x & E'_x = E_x \cos\theta + E_y \sin\theta & E'_x = E_x e^{i\phi/2} \\ E'_y = p_y E_y \text{,} & E'_y = E_y \cos\theta - E_x \sin\theta \text{,} & E'_y = E_y e^{-i\phi/2} \quad \text{,} \end{array} \tag{3.13}$$

describing a polarizer, rotator and retarder, respectively. Here p_x and p_y are attenuation coefficients and are between 0 and 1. Note, real optical materials contain a combination of all of these ideal effects, as well as potential depolarization effects. By multiplying a chain of Meuller matrices describing these ideal effects any real component can be described. Using the definition of the Stokes parameters from Eq. (3.9) of the previous section, we can write the Mueller matrices for the components of Eq. (3.13) as,

$$M_{pol} = \frac{1}{2}\begin{pmatrix} 1 & 1 & 0 & 0 \\ 1 & 1 & 0 & 0 \\ 0 & 0 & 0 & 0 \\ 0 & 0 & 0 & 0 \end{pmatrix} \qquad M_{rot} = \begin{pmatrix} 1 & 0 & 0 & 0 \\ 0 & \cos 2\theta & \sin 2\theta & 0 \\ 0 & -\sin 2\theta & \cos 2\theta & 0 \\ 0 & 0 & 0 & 1 \end{pmatrix}$$

$$M_{ret} = \begin{pmatrix} 1 & 0 & 0 & 0 \\ 0 & 1 & 0 & 0 \\ 0 & 0 & \cos\phi & \sin\phi \\ 0 & 0 & -\sin\phi & \cos\phi \end{pmatrix} \tag{3.14}$$

where the Mueller matrices of the polarizer, rotator and retarder are M_{pol}, M_{rot}, and M_{ret}, respectively.

In the case of a tokamak measurement of the direction of the magnetic field a couple key parameters must be defined. First, the Stokes vector describing the light emissions from the plasma is written as,

$$S_{plasma} = \begin{pmatrix} I_{bk} + I_\sigma + I_\pi \\ (I_\sigma - I_\pi)\cos(2\gamma) \\ (I_\sigma - I_\pi)\cos(2\gamma) \\ 0 \end{pmatrix} \quad , \tag{3.15}$$

where I_{bk}, I_σ, and I_π are the unpolarized background (bremsstrahlung), and polarized σ and π light intensities, respectively, and γ is the linear polarization angle. Also, the definition of a light detector, such as the PMT of the MSE, must be described as a Mueller matrix as follows,

$$M_{PMT} = \begin{pmatrix} 1 & 0 & 0 & 0 \\ 0 & 0 & 0 & 0 \\ 0 & 0 & 0 & 0 \\ 0 & 0 & 0 & 0 \end{pmatrix} \quad . \tag{3.16}$$

Note that a PMT is not sensitive to polarization and can only measure light intensities.

Recall the four intensity measurements of the previous section required to measure the Stokes vector. This process is quite laborious, and would require repeated mechanical movements of optical components in order to make a single measurement of γ. While mechanical movements of optical components may be acceptable for some experimental applications, the requirements of fusion energy experiments are stricter. The magnetic field of the plasma evolves over sub millisecond intervals requiring a high temporal resolution measurement. For this reason a new technique was devised that employs an optical component called a photoelastic modulator (PEM).

A PEM is a strain induced birefringent crystal that is oscillated at a resonant frequency by a piezoelectric transducer resulting in modulated retardance due to the photoelastic effect. Specifically, the phase varies in time as,

$$\phi_{1,2} = A_{1,2}\cos\left(\omega_{1,2}t\right) \quad , \tag{3.17}$$

where A_1 and A_2 are the retardance amplitudes, and ω_1 and ω_2 are different frequencies at which the PEMs are oscillated. Most tokamak PEMs have fundamental frequencies 20 and 23 kHz, however, as will be shown in the sections to follow, these frequencies must be revised for plasma pedestal measurements. To recover the S_1 and S_2 Stokes parameters the polarimeter uses two PEMs with modulator axis oriented 45^0 to one another, followed by an analyzing linear polarizer oriented 22.5^0 between both of the PEM axis. A schematic of a PEM is shown in Fig. 3.1.4-1, and a diagram of a dual PEM polarimeter setup is shown in Fig. 3.1.4-2.

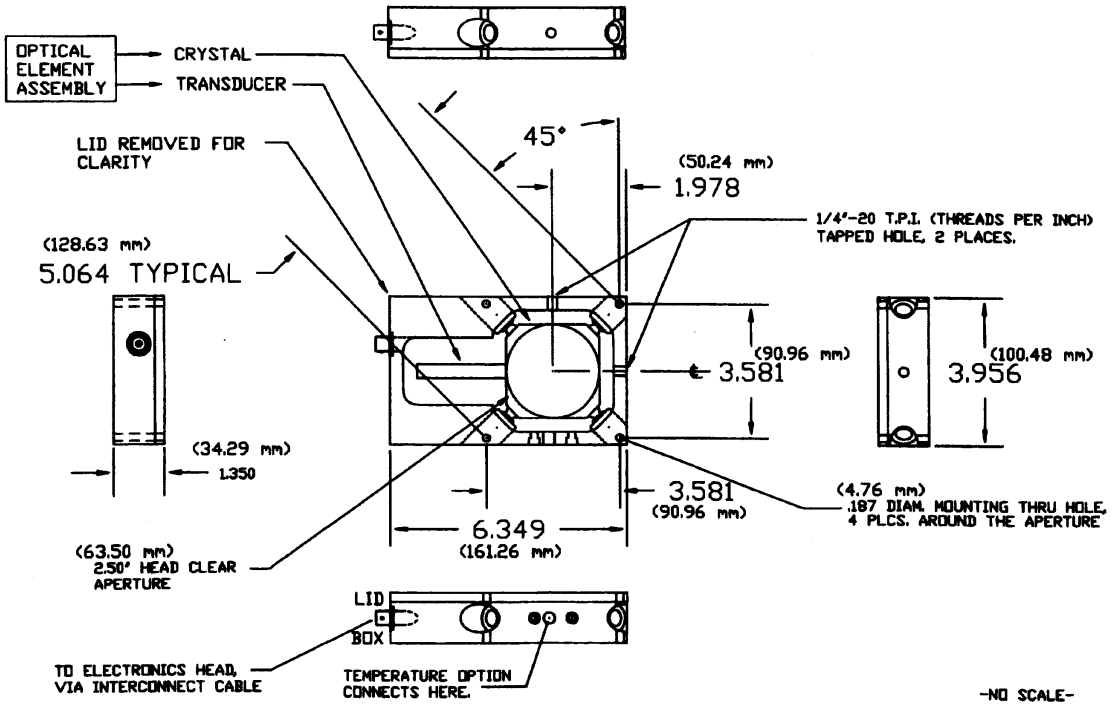

FIG. 3.1.4-1: A schematic diagram of an MSE PEM (Reprinted from Ref. 75).

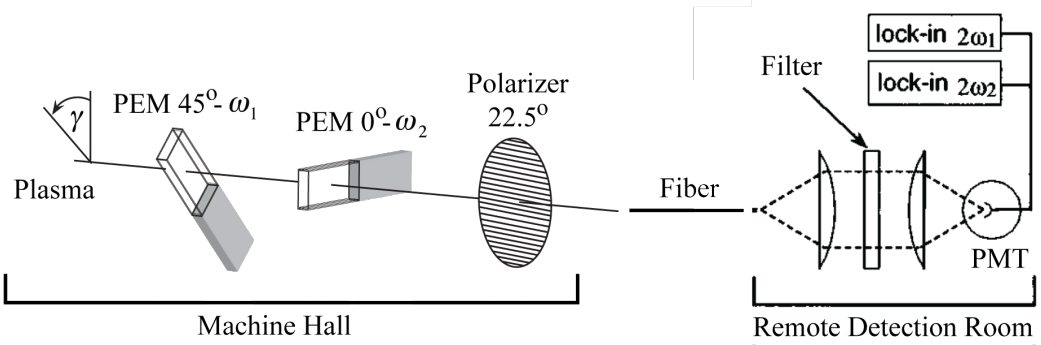

FIG. 3.1.4-2: The dual PEM polarimeter setup. The linear polarization angle γ, originating in the plasma, passes through two PEMs, then passes through a linear polarizer. The modulated signal is coupled to a remote detection room via fiber optic cable, where it is collimated and filtered before being detected by a PMT and demodulated using lock-in amplifiers.

The MSE signal can be described through the multiplication of a chain of Mueller matrices. Because all of the component axes are not equal to one another it is necessary to define the lab frame as being aligned with a single optical component. In this case, I chose to define the modulator axis of the second PEM to be the lab frame. Also, the Mueller matrix of a PEM is the Mueller matrix of a retarder except the retardance varies in time according to Eq. (3.17). The intensity modulated signal for the entire chain of MSE components is,

$$I_{PMT} = M_{PMT} M_{rot}(-\pi/8) M_{pol} M_{rot}(\pi/8) M_{PEM\,2} M_{rot}(-\pi/4) M_{PEM\,1} M_{rot}(\pi/4) S_{plasma} \,. \quad (3.18)$$

Carrying out the multiplication of Eq. (3.18) and performing Bessel function expansions of the nested sinusoidal terms yields,

$$I_{PMT} = I_{bk} + A_S \sin(2\gamma)\cos(2\omega_1 t) + A_C \cos(2\gamma)\cos(2\omega_2 t) + ... \quad , \quad (3.19)$$

where $A_S = (I_\sigma - I_\pi) J_2(A_1)/\sqrt{2}$ and $A_C = (I_\sigma - I_\pi) J_2(A_1)/\sqrt{2}$.

Recovery of γ from the intensity modulated signal requires lock-in amplifiers to measure the amplitudes of the $2\omega_1$ and $2\omega_2$ oscillating terms. The lock-ins recover the S_1 and S_2 Stokes parameters. The final expression for the measured γ is,

$$\gamma = \frac{1}{2}\tan^{-1}\left(\frac{1}{G}\frac{LI_a}{LI_b}\right) \quad , \quad (3.20)$$

where the lock-in outputs are $LI_a = A_S \sin(2\gamma)$ and $LI_b = A_C \cos(2\gamma)$, and the gain term $G = A_S/A_C$. G is a calibrated correction to the lock-in signals and is needed to eliminate variability in electronic gain.

3.1.5 Digital Lock-In Upgrade

The following section has been previously published by J.D. King, *et al.* in the Review of Scientific Instruments **81**, 10D739 (2010) (Ref 76).

Digital lock-in (DLI) detection[77] has become a well-established technique for recovering AC signals many times smaller than noise. Specifically, DLI detection employing field programmable gate arrays (FPGA) has enabled significant versatility in multi-channel systems at extremely low cost.[78] While the concept of the DLI is far from new,[79] implementation gives rise to application-specific subtleties. The following describes the unique DLI requirements of the motional Stark effect (MSE) diagnostic for internal magnetic field measurements of a tokamak plasma.

The full data acquisition system installed on the five operating MSE polarimeters of DIII-D is composed of a D-tAcq multi-channel DLI amplifier utilizing FPGA firmware, as well as a 32-channel 500 kHz digitizer. The digitizers record the raw PMT signal allowing full MSE spectral and magnetohydrodynamic (MHD) fluctuation[80] analysis. The DLI serves an identical function as previous analog lock-ins,[78] recovering in real time the amplitudes of the PEM second harmonics and thus the linear polarization angle.

Typical MSE measurements of the polarization angle γ utilize single phase analog lock-in amplifiers to recover the $\sin(2\gamma)$ and $\cos(2\gamma)$ polarimetry amplitudes from a modulated signal. Demodulation relies on a phase sensitive detector (PSD) to multiply

the modulated signal by a reference.[81] This results in signals $A_{s1,s2}A_{r1,r2}[1-\cos^2(2\pi f_{1,2}t)]$, where $A_{s1,s2}$, $A_{r1,r2}$, and $f_{1,2}$ are the signal amplitudes, reference amplitudes, and frequencies for the MSE PEM second harmonics at 40 and 46 kHz ($f_{1,2} = \omega_{1,2}/\pi$), respectively. The DC term, proportional only to $A_{s1,s2}$ and $A_{r1,r2}$, is recovered by filtering the PSD signal through a series of active low pass electronic filters. Identically, this multiplication and filtering can be done discretely using a digital system.[77, 82]

The D-tAcq hardware serves the mixing and filtering function of the DLI. Prior to demodulation the signals and references are electronically processed. A schematic of the entire data acquisition hardware implementation is shown in Fig. 3.1.5-1.

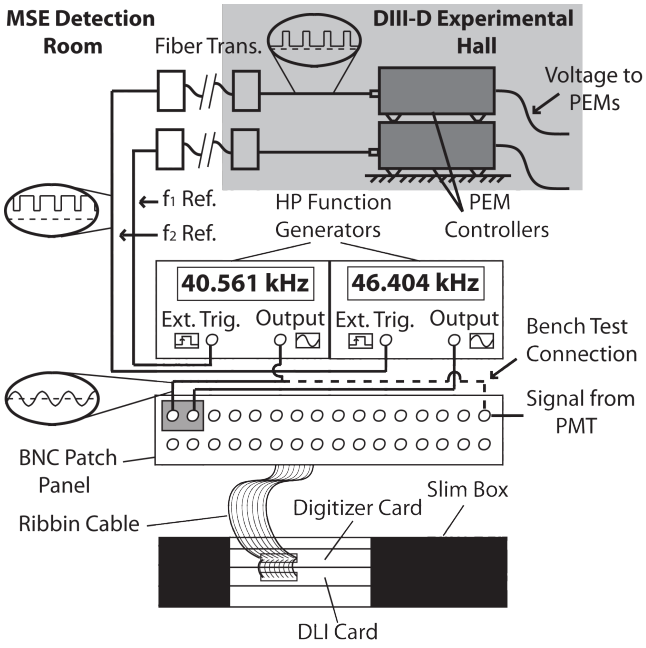

FIG. 3.1.5-1: Schematic of new MSE data acquisition system showing: PEM controllers, Fiber optic transmitter and receiver, two reference processing Hewlett Packard 3314A function generators; and the D-tAcq hardware consisting of a BNC patch panel, twisted pair ribbon cable connections to the digitizer and DLI cards, and a slim box housing. A dashed line shows the DLI bench testing connection.

The references originate at the PEM controllers and are sent via fiber optic transmitters from the DIII-D experimental hall to the MSE detection room. The result is a square wave reference of arbitrary duty cycle and DC offset. In order to demodulate only the desired second harmonics all other harmonics of the reference square wave must be removed. This was done by phase locking the reference to an output sinusoid of a Hewlett Packard (HP) 3314A function generator. This produces a nearly perfect sinusoid reference at the exact f_1 and f_2 frequencies. The amplitude and phase of these processed references were then adjusted to peak the DLI output. In particular, the phase differences between the references and signals were adjusted to 0° using the HP 3314A phase shifter. This is possible because the raw signals and references are separately digitized and their phases can be directly recovered through Fourier analysis[83]. Because this system permits exact phase matching and easy monitoring of the phase evolution during plasma

operations, it presents a clear advantage to the single phase analog setup, which requires time consuming in-vessel calibrations to re-peak signals.

The processed signals and references are connected to a BNC patch panel and transmitted to the DLI and digitizer computer cards via a twisted pair ribbon cable. Both the DLI and digitizer cards are housed in a slim box chassis with a back panel Ethernet network connection that transmits the digitized data to be stored in memory.

At the D-tAcq cards the signals and references are first digitized at 500 kHz. Then the firmware algorithm multiplies the digitally sampled signal $S(n,m)$ with the sampled sinusoidal references $R_{1,2}(n,m)$ and then sums these values over a predefined accumulator interval L to filter out carrier frequencies, such that the lock-in outputs $X_{1,2}(n)$ become

$$X_{1,2}(n) = \sum_{m=1}^{L} S(n,m) \cdot R_{1,2}(n,m) \,. \tag{3.21}$$

The subscript n indexes the values of the lock-in outputs in time, and the subscript m denotes the local accumulation operation. Both n and m are positive integers. For the MSE DLI we have chosen to digitize the PMT signal once and demodulate the f_1 and f_2 components using separately digitized references. While the full spectrum of the MSE contains many PEM harmonics as well as beat frequencies, the following analysis was simplified by only considering the second harmonics. This means the digitized signal takes the form

$$S(n,m) = A_{s1}\cos\left(2\pi f_1 dt\left[(n-1)L+m\right]\right) + A_{s2}\cos\left(2\pi f_2 dt\left[(n-1)L+m\right]+\phi\right), \tag{3.22}$$

where dt is the time between samples and ϕ is an arbitrary phase difference between the f_1 and f_2 components. The sampled references of the f_1 and f_2 second harmonics are,

$$R_{1,2}(n,m) = A_{r1,r2}\cos\left(2\pi f_{1,2}\, dt\,\left[(n-1)L+m\right]\right) \tag{3.23}$$

By inserting Eq. (3.22) and Eq. (3.23) into Eq. (3.21) a unique analytical solution is found. For the f_1 reference this solution takes the form

$$X_1(n) = \frac{A_{r1}}{4}\begin{pmatrix} A_{s1}\csc\left(2\pi f_1 dt\right)\left[2L\sin\left(2\pi f_1 dt\right)+\sin\left(2\pi f_1 dtC_1\right)-\sin\left(2\pi f_1 dtC_2\right)\right]+ \\ A_{s2}\csc\left(\pi\left(f_1+f_2\right)dt\right)\left[\sin\left(\pi\left(f_1+f_2\right)dtC_1+\phi\right)-\sin\left(\pi\left(f_1+f_2\right)dtC_2+\phi\right)\right]+ \\ A_{s2}\csc\left(\pi\left(f_1-f_2\right)dt\right)\left[\sin\left(\pi\left(f_1-f_2\right)dtC_1-\phi\right)-\sin\left(\pi\left(f_1-f_2\right)dtC_2-\phi\right)\right] \end{pmatrix}, \tag{3.24}$$

where $C_1 = 1+2nL$ and $C_2 = 1-2L+2nL$. From this expression one can readily change parameters to those of the MSE experiment, enabling quick analysis of various attributes of the algorithm.

A number of bench tests were carried out, which insured the analytical solution of Eq. (3.24) correctly represents the new hardware. The first bench test used the setup seen in Fig. 3.1.5-1, where the f_1 reference was also connected to the signal input of the patch panel instead of the modulated PMT signal. The accumulator L was arbitrarily set to 125 data points per lock-in output value, which for the 500 kHz sample rate of the digitizer corresponds to a 4 kHz data throughput rate for the DLI. These DLI parameters, along with the signal frequency of 40.561 kHz and amplitudes $A_{s1} \approx A_{r1} \approx 4V$ and $A_{s2} \approx A_{r2} \approx 0V$ where entered into Eq. (3.24).

In Fig. 3.1.5-2 it can be seen that the analytical solution agrees with the DLI data both for the overall DC recovered amplitude, and a fine oscillating structure. The oscillating structure has been arbitrarily shifted in phase to lineup with the measurement.

The oscillating artifact seen in Fig. 3.1.5-2 is not acceptable for real-time MSE polarization angle γ measurements. In an initial plasma data comparison with the analog lock-ins the DLI, with accumulator 125, showed a factor of 5 greater variation in the recovered γ, due to this oscillation.

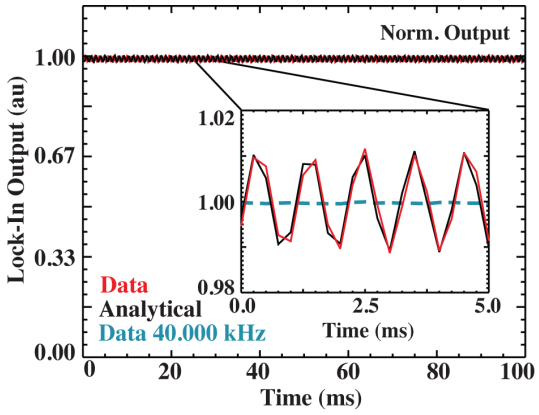

FIG. 3.1.5-2: Red represents the DLI output for a synthetic function generator signal input at the PEM frequency. Black represents the analytical solution computed for the same input parameters as the red synthetic signal. Blue represents the normalized DLI output for a 40.000 kHz synthetic input.

This artifact is caused when the accumulator interval does not contain an exact integer number of multiplier output periods. For the example shown in Fig. 3.1.5-2 the dimensionless expression $f_1 dtL$ must be an integer to avoid the oscillating artifact. Note, when $f_1 dtL$ and $f_2 dtL$ are integer values, Eq. (3.24) simplifies to an expression containing only the desired DC value proportional to the signal amplitude and accumulator interval,

$$X_1 = \frac{A_{s1} A_{r1} L}{2} \quad . \tag{3.25}$$

Further confirmation of this non-integer multiple effect was found by adjusting the function generator frequency of the DLI input signal and reference to f = 40.000 kHz. The accumulator parameter L was again set to 125 points, and dt = 0.002 ms. These DLI parameters give an integer value for $f_1 dt L$ of 5, and result in the complete elimination of

the oscillating artifact seen in the normalized output of Fig. 3.1.5-2. Note that this test only considers a single signal frequency. Including an additional signal at f_2 with a non-integer value for $f_2 dtL$ would cause another artifact to appear on the f_1 DLI output.

Tuning the PEM frequencies such that $f_1 dtL$ and $f_2 dtL$ are integer values is not possible. The frequencies of the PEMs are inherent to the crystal dimensions and, to a lesser degree, environmental conditions. For example, the tangential MSE PEMs have second harmonic frequencies of 40.561 and 46.404 kHz, and these frequencies slowly change by 7 to 10 Hz over a given run day as temperatures in the DIII-D experimental hall vary. Therefore, the only adjustable parameter of the $f_1 dtL$ and $f_2 dtL$ expressions is the accumulator interval L.

The firmware of the DLI allows the accumulator L to be set to any integer value between 2 and 5000. By varying L between 250 and 750 in Eq. (3.24), and setting A_{s1}, A_{s2}, A_{r1}, and A_{r2} to about 4V an identical trend in the standard deviation of the artifact was found for both the f_1 and f_2 DLI outputs. This trend is shown in Fig. 3.1.5-3. In addition to the general trend of decreasing artifact amplitude with increasing L, the standard deviation of the artifact approaches zero at six nodes (e.g. $L \sim 431$). Each of these nodes correspond to L values that allow both of the $f_1 dtL$ and $f_2 dtL$ expressions to approach integer values. For example, at the $L = 431$ node the $f_1 dtL$ and $f_2 dtL$ expressions approach integers 35 and 40, respectively. Also, the nodes L values were found to be invariant with respect to ϕ, $A_{s1,s2}$ and $A_{r1,r2}$. However, the overall standard deviation of the artifact does vary when the ratio of the signal amplitudes is changed.

The $L = 431$ node was found to be the smallest accumulator interval that reduces the DLI oscillating artifact beneath the electronic noise ($1 - 4 \times 10^{-3}$ in Fig. 3.1.5-3) of the analog system for both the f_1 and f_2 signals. At a temporal resolution of ~0.9 ms, this accumulator is comparable to the 2 kHz rate at which the analog units are sampled.

Recall, the simplifying assumption that the MSE spectrum only contains second harmonic components. For our setup the second harmonic amplitudes are about an order of magnitude greater than the odd harmonics and beat frequency amplitudes. It is likely that this second harmonic dominated spectrum allows this simplified analysis to successfully characterize the artifact reduction. However, Eq. (3.24) may no longer be representative of the DLI output if other harmonics and beats have a greater proportion in the spectrum.

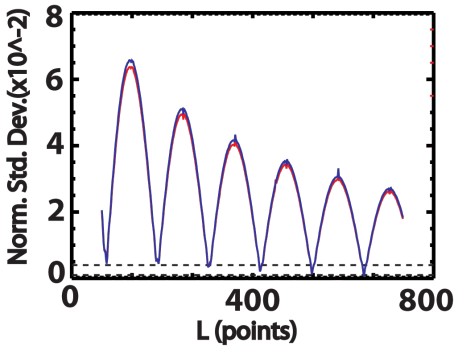

FIG. 3.1.5-3: Blue line represents analytically calculated amplitude of the oscillating artifact for f_1, and red line represents the same result for f_2. Dotted lines show the region of analog lock-in electronic noise.

3.2 Fast MSE Measured Fluctuations

The measurement of coherent MHD oscillations using the MSE is important for two reasons. First, it provides a self-diagnosis tool for improving MSE pedestal current measurements, which currently have very high uncertainties. Next, it can provide a direct measurement of both density and eventually magnetic fluctuations. Future magnetic fluctuation measurements could provide the first direct determination of internal MHD structure (e.g. NTMs and Alfvén Eigenmodes).

The following sections will discuss the installed signal processing hardware, as well as provide a derivation of the MHD fluctuation measurement expressions. The only physically meaningful MSE flucuation measurements thus far have been due to variations in the electron density. However, the expressions for magnetic fluctuation measurements are also provided to motivate a future work discussion. The installed hardware detailed in section 3.2.1 has been previously published in J.D. King, *et al.* Review of Scientific Instruments **81**, 10D739 (2010) (Ref. 76). Also, material of Section 3.2.2 was first published in J.D. King, *el al.* Review of Scientific Instruments **82**, 033515 (2011) (Ref. 84).

3.2.1 Installed Hardware

The MSE detects the modulated light intensity from the polarimeter using a Hamamatsu R636-10[85] photomultiplier tubes[86] (PMT). The resultant μA current originating at the detector must be converted to a voltage that spans the 20 V dynamic range of the digitizer. Because the MSE is a critical diagnostic to daily operation of the DIII-D tokamak, the qualification phase of this new hardware could not affect existing analog lock-in electronics. For this reason tandem, electrically isolated operation of the two systems was required. A simple schematic showing the successful circuit designed to meet these criteria is shown in Fig. 3.2.1-1.

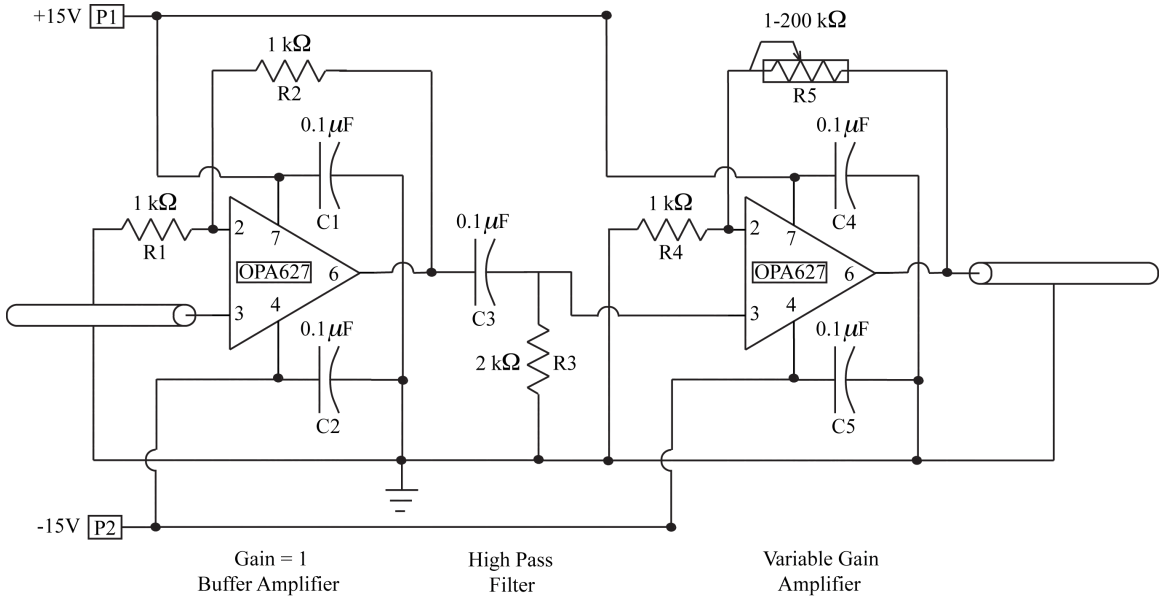

FIG. 3.2.1-1: The components of the signal processing hardware are a unity gain buffer amplifier, followed by an RC high pass filter and then a variable gain amplifier before being connected to a BNC patch panel.

The electronic processing begins by transforming the modulated MSE PMT current into a voltage drop across a 20 kΩ resistor connected to ground. This modulated voltage signal then passes to both the signal processing hardware of the new data acquisition system and the analog lock-in amplifiers.

Tandem operation of the new hardware and analog systems without electrical interference was needed to verify successful DLI operation. This electrical isolation was achieved by installing a very low noise unity gain Burr Brown (BB) OPA627 buffer amplifier as the first element in a signal processing chain.

The fidelity of the digitized signal is improved by utilizing the full ±10V dynamic range of the 16-bit digitizers. Typical MSE signals contain a large DC component resulting from the detection of unpolarized background light. This DC component contains no information about the polarization and is therefore removed through a passive high pass electronic filter. The AC coupled signal allows the gain stage amplifier (also, BB OPA627) to amplify only the modulated portion of the signal to the full dynamic range of the digitizer. Note, these analog signal processing electronics maintain a flat phase response to within a few degrees across all frequencies greater than 1 kHz.

Recall, prior MSE measurements relied on lock-in amplifiers to recover only the amplitudes of the second harmonic PEM signals. Now, after digitization, the signal can be Fourier analyzed[87] to provide information about MHD fluctuations and the full MSE spectrum. Specifically, higher harmonic spectral components, with frequencies less than the Nyquist frequency of 250 kHz, can be recovered.

3.2.2 MHD Fluctuation Analysis

MHD fluctuations have been found to mix with the MSE polarimeter modulations such that the amplitude of density ($\tilde{n}$) and polarization angle ($\tilde{\gamma}$) fluctuations may be recovered. Vertical magnetic field fluctuations ($\tilde{B}_z$), which are proportional to $\tilde{\gamma}$, could provide the first measurement of the internal structure of MHD[80]. While current efforts have revealed that the ratio of signal-to-noise (SNR) is below that required for successful $\tilde{B}_z$ measurements, improvements to the MSE and/or neutral beam may enable this measurement in the future. Future MSE improvements will be discussed in the final chapter of this work.

To first order, the MSE signal is composed of two second harmonic PEM frequencies ($2\omega_1$ and $2\omega_2$) and DC background light. As was described in Section 3.1.4, this signal takes the form,

$$I_{PMT} = I_{bk} + A_S \sin(2\gamma)\cos(2\omega_1 t) + A_C \cos(2\gamma)\cos(2\omega_2 t) \quad , \tag{3.26}$$

where I_{bk} is the background intensity, and the $A_S \sin(2\gamma)$ and $A_C \cos(2\gamma)$ are the amplitudes used to measure γ. Substitution of an oscillating perturbation to the unpolarized background intensity $I_{bk} = I_{bk} + \tilde{I}_{bk}\cos(\omega t)$, the polarized light amplitudes $A_{S,C} = A_{S,C} + \tilde{A}_{S,C}\cos(\omega t)$, and the polarization angle $\gamma = \gamma + \tilde{\gamma}\cos(\omega t)$ into Eq. (3.26) gives,

$$\begin{aligned} I_{PMT} &= I_{bk} + \tilde{I}_{bk}\cos(\omega t) \\ &\quad + A_S \sin(2\gamma)\cos(2\omega_1 t) + A_C \cos(2\gamma)\cos(2\omega_2 t) \\ &\quad + \left[\frac{\tilde{A}_S \sin(2\gamma) + 2A_S\tilde{\gamma}\cos(2\gamma)}{2}\right]\cos\left[(2\omega_1 \pm \omega)t\right] \\ &\quad + \left[\frac{\tilde{A}_C \cos(2\gamma) - 2A_C\tilde{\gamma}\sin(2\gamma)}{2}\right]\cos\left[(2\omega_2 \pm \omega)t\right] \end{aligned} \quad , \tag{3.27}$$

where ω is the toroidal MHD frequency of rotation. It can be seen that the original $A_S \sin(2\gamma)$ and $A_C \cos(2\gamma)$ values are recovered as the third and fourth terms in Eq. (3.27). The second term shows an intensity fluctuation in the unpolarized background light at the MHD frequency. The fifth and sixth terms of Eq. (3.27) result in four sidebands of the second PEM harmonics at frequencies $2\omega_1 \pm \omega$ and $2\omega_2 \pm \omega$. The sideband amplitudes are proportional to both the fluctuating polarized light intensities $\tilde{A}_{S,C}$ and $\tilde{\gamma}$. Each component of the spectrum has been experimentally verified through the application of Fourier analysis.

The $\tilde{\gamma}$ can be calculated from the following system of six equations,

$$S_{2\omega_1 \pm \omega} = \frac{\tilde{A}_S \sin(2\gamma) + 2A_S \tilde{\gamma} \cos(2\gamma)}{2} \quad , \tag{3.28}$$

$$S_{2\omega_2 \pm \omega} = \frac{\tilde{A}_C \cos(2\gamma) - 2A_C \tilde{\gamma} \sin(2\gamma)}{2} \quad , \tag{3.29}$$

$$S_{2\omega_1} = A_S \sin(2\gamma) \quad , \tag{3.30}$$

$$S_{2\omega_2} = A_C \cos(2\gamma) \quad , \tag{3.31}$$

$$G = \frac{A_S}{A_C} \quad , \tag{3.32}$$

$$\frac{\tilde{A}_S}{A_S} = \frac{\tilde{A}_C}{A_C} \quad , \tag{3.33}$$

where the $S_{2\omega_{1,2} \pm \omega}$ terms are the sideband amplitudes, the $S_{2\omega_{1,2}}$ are the second harmonic amplitudes, G is the gain term determined through in-vessel calibration. Eq. (3.33) expresses the assumption that any change in density will result in an identical change in the polarized light intensity. This is a fair assumption since changes in plasma density simply change the overall intensity of the beam-stimulated emissions. Solving the system of equations (2.28) through (2.33) for $\tilde{\gamma}$ we have,

$$\tilde{\gamma} = \frac{1}{2}\left(\frac{S_{2\omega_1 \pm \omega}}{S_{2\omega_1}} - \frac{S_{2\omega_2 \pm \omega}}{S_{2\omega_2}} \right) \sin(4\gamma) \quad . \tag{2.34}$$

As mentioned previously, $S_{2\omega_1}$ and $S_{2\omega_2}$ are already routinely recovered for existing MSE polarimetry, so the only new signals that need to be successfully recovered are the $S_{2\omega_1 \pm \omega}$ and $S_{2\omega_2 \pm \omega}$ sidebands. In an attempt to recover these sidebands standard Fourier techniques have been employed, including digital filtering[83]. Also, noise reduction algorithms involving single value decomposition (SVD) analysis have been applied. Despite utilizing these digital signal processing routines the SNR for the largest core sideband is ~2, which is too low to be considered physically meaningful.

$\tilde{\gamma}$ is related to $\tilde{B}_z$ through a simple expression involving the MSE view angle geometry terms A_1 and A_2. This expression is, $\tilde{B}_z = (A_2/A_1)\tilde{\gamma}B_t$, where B_t is the local toroidal magnetic field. While measuring $\tilde{B}_z$ is still the focus of future work, the MHD fluctuation analysis presented in this section has resulted in the discovery of MHD interference with pedestal γ measurements. This result, and its impact on the design of future MSE measurements, will be discussed in Chapter 4.

3.3 Diamagnetic Loops and Magnetic Probes

The diamagnetic loop is a single poloidal coil that surrounds the outside of the vacuum vessel. Because the loop encloses a full cross-section of the plasma it measures the total toroidal flux. To determine the plasma current and pressure, and hence total stored energy, the dominant vacuum magnetic flux must be first subtracted as follows,[88,89]

$$\Delta\Phi_D = \Phi_{total} - \Phi_{vacuum} \approx \frac{2\kappa}{1+\kappa^2}\frac{(\mu_0 I_p)^2}{8\pi B_{\phi 0}}\left(1-\beta_p\right) \quad , \tag{3.35}$$

where κ is the vertical elongation, I_p is the plasma toroidal current, β_p is the ratio of poloidal kinetic to magnetic pressure, and $B_{\phi 0}$ is the toroidal magnetic field at the magnetic axis.

The internal stored energy W of the plasma can be written as[22],

$$W = \tfrac{3}{8}\mu_0 R_0 \beta_p I_p^2 \quad , \tag{3.36}$$

where R_0 is the major radius. By integrating the voltage signal of a Rogowski coil[22] I_p can be directly measured. This combined with the diamagnetic loop measurement of $\Delta\phi_D$ are then plugged into Eq. (3.36) to determine the internal energy of the plasma. Note, κ is determined from magnetic probe measurements described below.

There are eight diamagnetic loops installed on DIII-D, two of which are continuously used. These loops surround the exterior surface of the vacuum vessel and are Mg-O insulated.

Mirnov magnetic probes are multiturn coils capable of measuring time changing magnetic fields. The voltage induced at the coil terminals is dependent upon a change in poloidal flux. The total flux measured $\Phi = NAB$ is dependent upon the area of the coil cross section A, the number of turns N and the magnetic field intersecting the probe area B.[89, 90]

The probes in DIII-D used for measuring MHD are located inside the vacuum vessel in order to avoid the shielding effects of the wall eddy currents. To protect them from the plasma they are placed behind the non-conducting graphite tile armor. Because of tight spacing behind the tiles, the coils are wound in an oval cross section.

Tearing mode perturbations create radial displacements that cause a time changing poloidal flux at the wall of the machine. Because the mode is rotating toroidally at the frequency of the bulk plasma (ω), the frequency of the perturbation at the wall is related to the plasma rotation at the rational surface by $n\omega$. From this change in poloidal flux, the fluctuating radial field ($\tilde{B}_r$) amplitude at the rational surface can be determined as follows[91],

$$\left|\tilde{B}_r\right| \approx \frac{1}{2}\left(\frac{b}{r}\right)^{m+1}\left|\tilde{B}_\theta\right|_{wall} \quad , \tag{3.37}$$

where b is the minor radius of the magnetic probe, r is the rational surface minor radius, m is the poloidal mode number, and $\left|\tilde{B}_\theta\right|_{wall}$ is the fluctuating poloidal magnetic field amplitude measured by the probe at the wall. In the approximation of a large aspect ratio tokamak the island width w is determined as follows,

$$w \approx \left(\frac{16 r R_0 \left|\tilde{B}_r\right|}{m s B_{\phi 0}} \right)^{1/2} \quad , \tag{3.38}$$

where $s = r(dq/dr)/q^2$. Because DIII-D is not a large aspect ratio tokamak the island widths have to be corrected by a factor of 2/3.[91] This scaling factor was found using island size data measured from electron cyclotron (ECE) measurements, which are described in the next section.

3.4 Electron Cyclotron Emission Radiometry

Moving charged particles rotate around externally applied magnetic fields. This rotational acceleration gives rise to the emission of electromagnetic radiation called electron cyclotron emissions (ECE). As was mentioned previously, the expression describing the frequency of this emission is, $\omega_{ce} = eB/m_e$ where e is the electric charge associated with the electron, B is the magnitude of the magnetic field, and m_e is the rest mass of an electron. For typical fields in DIII-D of 1 to 2 T the second harmonic cyclotron frequency range of 83.5 to 129.5 GHz provides good radial coverage. The second harmonic of the cyclotron emission is used to provide the greatest range accessible of densities.

Since the dominant toroidal magnetic field in a tokamak is proportional to $1/R$, a spectrum of electron frequencies are emitted across the plasma. Binning the spectrum into narrow frequency bands at the detection stage allows a radial profile measurement to be obtained from a single chord path.

On DIII-D the signal is first split using waveguide couplers, and then mixed with one of three mixers at 81, 96, and 112 GHz. This mixing down converts the signals into three 2-18 GHz bands. These bands are then split using a quadraplexer and the output is then split again using 2 and 4 channel power splitters to arrive at a total of 40 different frequency bands each one constituting a single local electron temperature measurement. These channels are then bandpass filtered and detected[92].

The intensity of the cyclotron emission is dependent upon the electron temperature (T_e) of the plasma. The plasma serves as a black-body radiator with a Maxwellian distribution of electron velocities. Because $h\nu << kT_e$, the intensity of the cyclotron emission can be approximated by Rayleigh-Jeans law as,

$$I_{BB} = \frac{\omega_c^2}{4\pi^2 c^3} kT_e \quad . \tag{3.39}$$

Similar to the previously discussed MSE and magnetic probe fluctuation measurements, coherent MHD oscillations in the electron temperature ($\tilde{T}_e$) can be measured using ECE. Here the presence of a tearing mode results in a flattening of the temperature profile about the rational surface at the O-point. For a view chord located inside of the rational surface, the T_e will decrease at the O-point and increase at the X-point. The result is a fluctuation in the ECE signal intensity $\tilde{I}_{BB}$ that is proportional to $\tilde{T}_e$.

As will be shown later, recovery of $\tilde{T}_e$ for a number of channels provides an estimate of the island structure.

Chapter 4

Experiment and Measurement

The following chapter is comprised of previously published materials. Specifically, Section 4.1.2 first appeared in J.D. King, *et al.*, Review of Scientific Instruments **81**, 10D739 (2010) (Ref. 76). The material from a paper entitled, "Hybrid-like 2/1 flux-pumping and magnetic island evolution due to edge localized mode-neoclassical tearing mode coupling in DIII-D", submitted to the Physics of Plasmas is reprinted in Sections 4.2 and 4.3 (Ref. 93). Section 4.4 was originally presented in J.D. King, *et al.*, Review of Scientific Instruments **82**, 033515 (2011) (Ref. 84).

4.1 Plasma Equilibrium

In tokamaks the plasma is held away from the solid vacuum vessel walls through applied and induced magnetic fields. Force equilibrium must be established between the outward directed plasma pressure and the inward restoring magnetic pressure. The plasma can be approximated as a conducting fluid for these purposes, permitting the use of ideal magnetohydrodynamics (MHD). This MHD force balance takes the form

$$\nabla p = j \times B, \tag{4.1}$$

where j is the plasma current density, B is the confining magnetic field, and p is the plasma pressure. Recall the key parameter describing the efficiency of sustaining plasma equilibrium by a magnetic field is beta.[20,22]

The internal plasma current profile $j(r)$ can take many forms (e.g. peaked or hollow) and is not a simple machine parameter like the toroidal magnetic field. In modern tokamaks plasma current is generated through a variety of different sources including ohmic, neutral beam, electromagnetic wave, and internally generated bootstrap. Each of these current sources has different dependences, allowing for significant variability in the possible current profiles. For example, the portion of the current induced ohmically through the central solenoid is dependent on the conductivity of the plasma, which is proportional to $T_e^{3/2}$, which is proportional to auxiliary power input and impurity radiation and the presence of magnetic islands *etcetera*. Also, the location where auxiliary current is deposited is dependent upon the density profile, among other things. In addition, the shape of the current profile impacts global and resistive stability

as well as internal plasma turbulence and transport. For these reasons, determination of the toroidal current profile is vital to the accurate reconstruction of tokamak equilibrium.

4.1.1 The Code EFIT

Tokamak equilibrium reconstruction is the backbone of nearly all magnetically confined fusion research. From maintaining plasma shape and global stability, to tearing stability or transport barrier studies, the use of plasma equilibria is fundamental. The following description follows references 94, 95 and 96.

Magnetic probes and flux loops only provide global current parameters like plasma internal inductance l_i. The MSE diagnostic constrains equilibrium reconstructions throughout the plasma volume allowing for the internal current profile to be determined. From this information, and knowledge of the toroidal field strength, the toroidal current density profile and poloidal field profile are recovered and an equilibrium can be calculated.

Determination of plasma equilibrium starts with rewriting the ideal MHD force balance, given by Eq. (4.1), in terms of poloidal flux ψ. The resultant expression is the Grad-Shafranov equation and takes the form,

$$\Delta^*\psi = -\mu_o R J_\phi \quad \text{, where} \quad \Delta^* = R^2\nabla\cdot\left(\nabla/R^2\right) \quad . \tag{4.2}$$

$$J_\phi = RP'(\psi) + \mu_o FF'(\psi)/4\pi R \tag{4.3}$$

or in integral form,

$$\psi_p(\vec{r}) = \int_V dR'dZ'G_\psi(\vec{r},\vec{r}')J_\phi[R',\psi(\vec{r}')].$$

Here G_ψ is the Green's induction function relating a local toroidal current filament to poloidal flux. The summation of the poloidal flux contribution of many toroidal current filaments provides an estimate of the whole plasma effect on a single probe measurement. P' and FF' are stream functions which are dependent on normalized magnetic poloidal flux x, and are approximated using a linear combination of basis functions y_n (either polynomial or spline) with coefficients α_n and γ_n taken as,

$$P'(\psi) = \sum_n \alpha_n y_n(x) \qquad FF'(\psi) = \sum_n \gamma_n y_n(x) \quad . \tag{4.4}$$

From the flux-function an expected magnetic probe measurement can be calculated as follows,

$$C_i^{m+1}(\vec{r}_i) = \sum_j G_{Ci}(\vec{r}_i,\vec{r}_{ej})I_{ej} + \int_{V^m} dR'dZ'G_{Ci}(\vec{r}_i,\vec{r}')J_\phi[R',\psi^m(\vec{r}'),\vec{\alpha}^{m+1}] \quad , \tag{4.5}$$

where $\vec{\alpha}$ is the vector containing all of the α_n and γ_n coefficients, as well as external poloidal field coil currents I_{coil}. The finite size of the poloidal field coils doesn't allow them to be considered known quantities in Eq. (4.5). Instead they are also modeled as small current filaments similar to the integration over the plasma volume.

By substituting Eq. (4.3) and (4.4) into Eq. (4.5) and rearranging, a system of linear equations is obtained that depends on the number of measurements used. This rearrangement can be written as the following normal equation,

$$\vec{\vec{R}}\vec{\alpha} = \vec{M} \quad , \tag{4.6}$$

where $\vec{\vec{R}}$ is a known response matrix that is dependent upon the Green's functions (available in a look up tables), $\vec{\alpha}$ is the unknown vector of coefficients that is being solved, and $\vec{M}$ is the vector containing all the measured values. The measured values include the MSE and magnetic probes. The equilibrium fitting code[95] (EFIT) successively solves for $\vec{\alpha}$ numerically[97] (i.e. Jacobi method, or single value decomposition) and relies on convergence criteria to establish a good fit. This can be thought of as a repeated guess and check process. The approximate equilibrium is guessed; the resulting magnetic probe and MSE measurement values are calculated based on that guess and then checked against the actual diagnostic measurements. Note, with each iteration a new solution $\vec{\alpha}^{m+1}$ is generated to serve as the next guess of the equilibrium. The specific convergence is determined by minimizing the following,

$$\chi^2 = \sum_i \left(\frac{M_i - C_i}{\sigma_i} \right)^2 \quad , \tag{4.7}$$

where M_i is the measured value of the i^{th} probe/MSE channel, C_i is the calculated value of the i^{th} probe based on the particular iteration being considered, and σ_i is the uncertainty of the real measurement.

4.1.2 Digital and Analog Lock-In Equilibria

As was discussed in the Section 3.1.4 the accumulator interval of the digital lock-in requires an exact integer number of multiplier output periods to avoid the generation of an oscillating artifact. Using Eq. (3.24) from Section 3.1.4, it was shown that the first node where the oscillating artifact was reduced below the noise of the analog lock-in was $L = 431$.

By setting L to 431 for the tangential MSE array, the DLI recovered γ now matches that of the analog system for all channels. A few examples of this agreement are shown in Fig. 4.1.2-1. The channel 7 standard deviations from ~ 3800 to 4000 ms were 0.12° and 0.10° for the analog and DLI, respectively. The difference in averaged γ values for both systems across all channels was less than the 0.1° – 0.2° uncertainty of the measurement.[98]

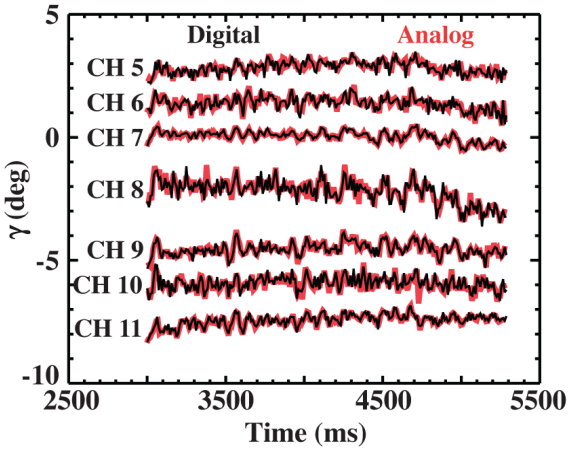

FIG. 4.1.2-1: Black represents DLI-recovered γ. Red represents analog lock-in recovered γ (shot 142349).

Using DLI-recovered γs, EFIT[96] equilibria were computed and showed very good overall agreement with equilibria computed using analog data. Figure 4.1.2-2 compares the equilibria of the analog and DLI for shot 142349 at 4000 ms. The magnetic axis of both the analog and DLI were computed to be 3.6 cm below the machine midplane. The major radius of the magnetic axis showed only a 3 mm difference between the two cases.

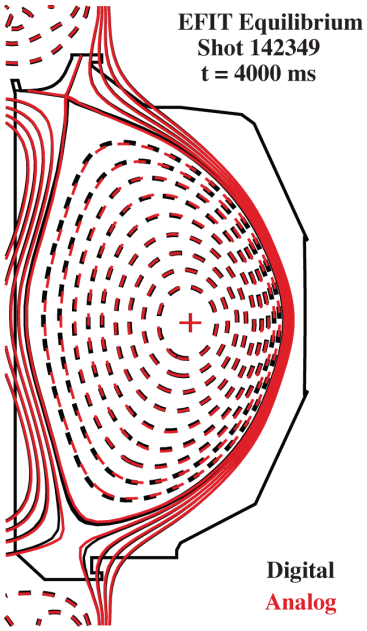

FIG. 4.1.2-2: Black represents the EFIT equilibrium using DLI data. Red/gray represents an EFIT equilibrium from analog lock-in data (shot 142349).

Also, significant agreement of the DLI- and analog-computed safety factor profile was observed. Both systems show $q_{min} \sim 1.1$, with only 5% difference between them. The safety factor at normalized ρ of 0.95 shows only a 3% difference. The internal inductance measured by both systems was ~ 0.7.

These observations demonstrate, with careful consideration of the accumulator interval, this relatively simple multi-channel DLI can provide an identical real-time MSE measurement to its analog counterpart. Because of inconsistencies between the analog hardware across all 5 MSE polarimeters, the DLI recovered MSE signals are used in the remainder of this work.

4.2 Edge Localized Mode-Neoclassical Tearing Mode Coupling

A number of observations have been made showing a correlation between the rapid onset of an ELM and a correspondingly rapid decrease in the magnetic island width of an NTM. There is presently no explanation as to how an ideal ELM interacts with the resistive NTM. The subsections to follow provide the most comprehensive analysis of this physics to date.

4.2.1 Alfvénic Island Width Shrinkage

For this section, saturated 2/1 NTMs were considered. The radial proximity of 2/1 NTMs to the Mirnov probes produces the largest $\tilde{B}_\theta$ amplitudes, and hence result in the greatest signal-to-noise for studying mode width evolution. ECE radiometry[92] temperature ($\tilde{T}_e$) and MSE density[99, 84] fluctuation ($\tilde{n}_e$) data are also considered and agree well with probe width measurements.

These multiple fluctuation diagnostics show drops in amplitude associated with the 2/1-ELM coupling. Figure 4.2.1-1 shows significant drops in the NTM $\tilde{n}_e$, $\tilde{T}_e$, and $\tilde{B}_z$ amplitudes during ELMs. Note, the Mirnov probe measurement is taken at the wall, the MSE channel is located in the edge pedestal on the low field side midplane of the machine, and the ECE channel is measuring near the mode rational surface on the high field side of the machine. Despite these very different radial locations each signal exhibits a similar drop in amplitude correlated with a filterscope measurement of ELM induced D-α light emissions[100].

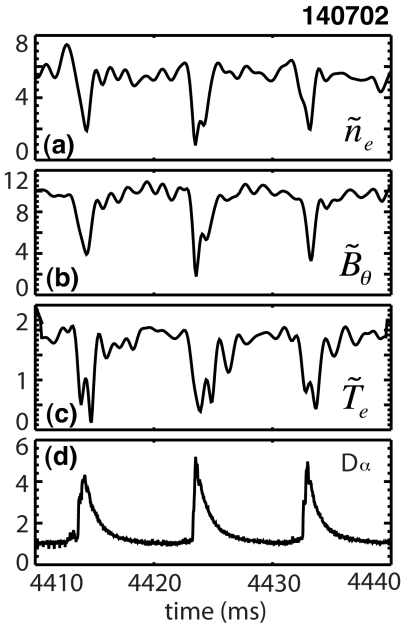

FIG. 4.2.1-1: Amplitudes of arbitrary units (a) MSE density fluctuation at the edge pedestal (b) Mirnov probe (c) high field side core ECE electron temperature fluctuation near the rational surface (d) filterscope measurement of D-α light intensity due to ELMs.

To verify that these drops in signal amplitude are due to island shrinkage as opposed to global plasma displacements the entire 40 channel ECE array was used to estimate the island structure. Figure 4.2.1-2(a) shows the island structure ~ 600 μs before and after an ELM event measured again on the high field side of the machine. This contour plot is detrended by removing the absolute value of the temperature for each channel and only considering the fluctuating component $\tilde{T}_e$. The blue and red colors represent temperatures less than and greater than the local absolute temperature, respectively. A clear 180^0 phase inversion occurs across the rational surface. The rational surface remains stationary across the ELM event. Figure 4.2.1-2(b) shows two normalized cross-cuts of the island O-point, before (1) and after the ELM (2). These fluctuation profiles are separately normalized on either side of the rational surface using the local maximum $\tilde{T}_e$ amplitude. The peak fluctuation amplitudes correspond to the maximum radii of the island seperatrix. This means that the distance between the peak amplitudes in Fig. 4.2.1-2(b) provides an estimate of the full island width. The distance between the peaks in profile 1 is about 4 cm larger than that of profile 2, therefore the island shrinks by ~ 4 cm across the ELM. This particular ELM was relatively small at less than 20 kJ for a plasma with total stored energy of 750 kJ. For larger ELMs, greater than 80 kJ, the drop in island width would require a 15 cm radial displacement of the rational surface to explain the drop in $\tilde{B}_\theta$ measured at the wall, which is far greater than is believed physically possible.

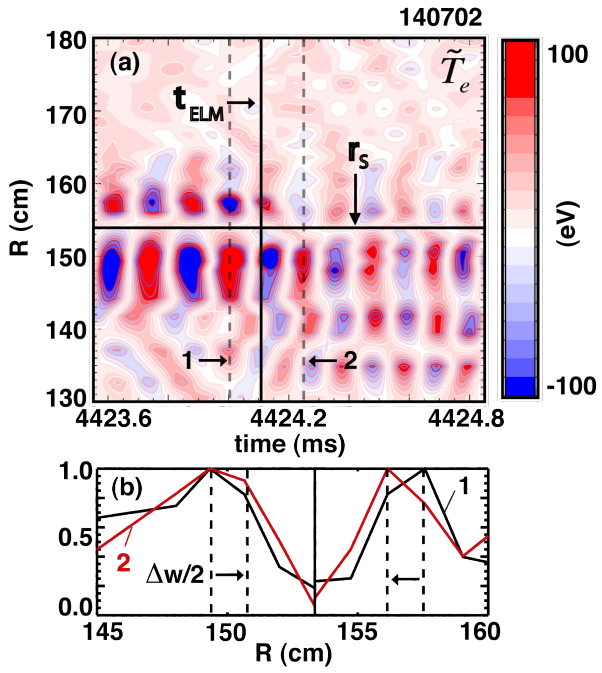

FIG. 4.2.1-2: Electron cyclotron radiometry measurements of poloidal island shrinking, (a) island structure, time of ELM crash (t_{ELM}), time before ELM (1) and time after ELM (2), (b) normalized cross cuts (1) and (2) of the island before the ELM (black-1) and after the ELM (red-2).

4.2.2 ELM size vs. Island Shrinkage

ELM-NTM coupling can be considered in two distinct regions, an Alfvénic timescale drop in the island width followed by a resistive recovery to the original saturated island width. This section discusses a relationship between a drop in island width and the size of the ELM.

To isolate ELMs as the only MHD perturbing the island, the 2/1 modes were restricted to a saturated island size (between ELMs) of $\tilde{B}_\theta$ ~ 15 G, and auxiliary power remained constant. This strict criterion on auxiliary heating allows β_N to be restricted to a narrow region between 1.4 and 1.6. To maintain a constant distance between the rational surface and the edge pedestal, q_{95} for most cases was held at 4. One shot had q_{95} of 5, but still showed the same general trend. The size and period of the perturbing ELMs were varied by changes in the plasma shape,[54] resulting in negligible radial differences between the edge pedestal and the rational surface. A sample discharge is shown in Fig. 4.2.2-1. The highlighted region meets all specified criteria.

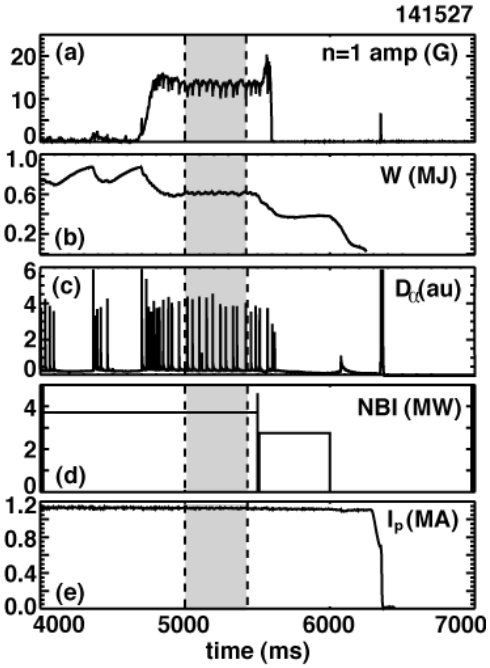

FIG. 4.2.2-1: (a) Mirnov probe amplitude (G), (b) diamagnetic measurement of total plasma stored energy (MJ), (c) filterscope measurement of D-α light intensity resulting from ELM events, (d) total injected neutral beam power (MW), (e) plasma current (MA).

The size of the ELM was determined from a diamagnetic loop measurement of the drop in the plasma internal stored energy (W). Diamagnetic loop measurements are only sensitive to course changes in W, therefore relatively large ELMs (> 25 kJ) were considered. Due to an ELMs rapid change in W and the large skin time of the vacuum vessel wall, accurate measurements of the change in W require that the ELM period be longer than 50 ms. For consistency infra-red television (IRTV) measurements[101] of ELM divertor heat fluxes were compared with the diamagnetic loop measured W.

Figure 4.2.2-2 shows a clear upward trend between the fractional stored energy loss $\Delta W/W$ of the ELM and the fractional drop in the island width $\Delta w/w$. Each point plotted corresponds to a single ELM event. $\Delta W/W$ is calculated by subtracting the W measured after an ELM from W before the ELM and then dividing by the W before the ELM. An identical procedure is followed for calculating $\Delta w/w$, where the island widths are determined using Mirnov probe measured $\tilde{B}_\theta$. Note the good agreement between the IRTV measured ELM energy changes and the diamagnetic loop.

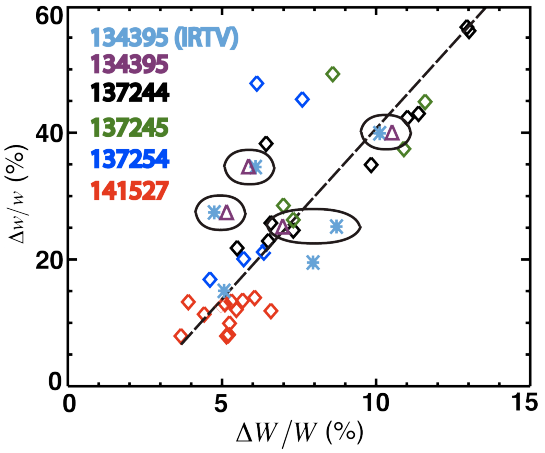

FIG. 4.2.2-2: Fractional drop in the magnetic island width (measured by Mirnov probes) vs. the fractional drop in stored energy associated with ELMs (measured by diamagnetic loop and IRTV divertor camera).

Proximity partly explains this stronger ELM-NTM coupling as the ELM size increases. ELM size is related to the radial depth of the most unstable mode[32]. Specifically, the dominant lower order mode numbers of the ELM are located deeper in the plasma and result in greater energy expulsion. Because of their greater depth, larger ELMs also have a greater proximity to core tearing modes improving their interaction.

4.2.3 Restive Recovery to Saturation

By applying a downward going impulse perturbation δ_o to the MRE from Section 2.1.3 and expanding, an accurate description of the ELM-NTM coupling resistive recovery phase is obtained. The relatively fast impulse (on an Alfvénic timescale) at an ELM and the relatively long τ_R in the MRE, suggests an ideal coupling of the NTM to the ELM, which is a peeling/ballooning mode; this could result in a transient negative "pole" in the Δ' term[102]. The evolution of the island width w is taken as

$$w = w_{sat} - \delta_o e^{-t/\tau_{relax}} \quad , \tag{4.8}$$

where w_{sat} is the saturated island width, t is time, and τ_{relax} is a time constant given by,

$$\tau_{relax} = \frac{w_{sat}^2 L_p \tau_R}{r_s^2 \varepsilon^{1/2} L_q \beta_p} \quad . \tag{4.9}$$

Figure 4.2.3-1 shows excellent agreement between the measured island width and this analytical description of the recovery given by Eq. (4.8). The relaxation time constant for this discharge was calculated to be 11.3 ms. The drop (δ_o) is not analytically

determined and was taken from the local minimum of the measured values for each of the coupling events.

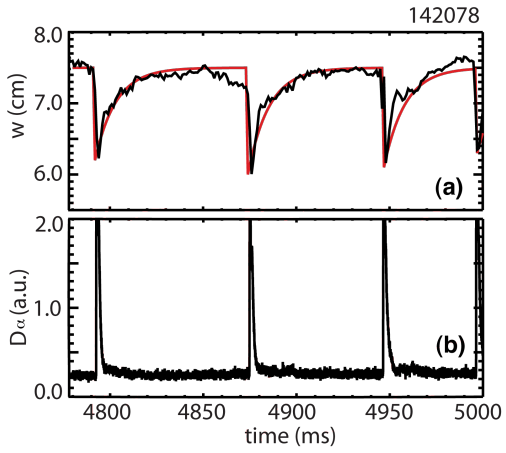

FIG. 4.2.3-1: For ELM-NTM coupling events, (a) - (black) measured island width using Mirnov probe $\tilde{B}_\theta$ measurements (red) analytical expression for the recovery given by Eq. (4.8). (b) Filterscope measurement of ELM induced D-α emissions.

This section shows that the recovery of the NTM to a saturated island width can be accurately modeled using the MRE. Also, it was shown that the size, and therefore proximity of the ELM to the NTM, results in stronger coupling. Specifically, the larger the ELM the greater the drop in the NTM island width. This finding agrees with flux-pumping observations presented in the next section.

4.3 Magnetic Flux-Pumping

Interestingly the avoidance of sawteeth in higher q_{95} hyrbids is tied to the presence of a 3/2 tearing mode[63], which couples to ELMs and causes repeated Alfvénic relaxations of the current profile[64]. With each ELM-NTM coupling event, poloidal flux is pumped from the core to the edge of the plasma across the 3/2 rational surface. Throughout this work the transport of poloidal flux across the rational surface of an NTM is referred to as "flux-pumping".[64] Note that no internal flux measurement is made. Instead changes in flux are inferred from measurements of the vertical magnetic field strength. By flattening the toroidal plasma current profile, q outside the 3/2 rational surface decreases and q inside the rational surface increases. For sufficiently rapid ELM events, the minimum safety factor (q_{min}) stays above unity and sawteeth stability is maintained. This magnetic flux-pumping is measured directly from MSE polarimeter[36, 37] data using Ampere's law[103] without equilibrium reconstruction. Later in this work we will show that magnetic flux-pumping is not unique to the 3/2 tearing mode.

In the higher performing hybrid discharges (q_{95} ~3) normalized beta is limited to a value ~20% smaller than the no-wall limit[6] ($4l_i$), where l_i is the plasma internal inductance. This is partly due to energy confinement degradation from the sawteeth themselves[47] and partly due to the sawteeth triggering 2/1 tearing modes. The goal of advanced inductive hybrid discharges has mostly focused on pushing plasma performance without stability or current profile control. From the findings presented in this work, it appears that partial 2/1 mode suppression may have a double benefit of allowing higher achievable β_N while providing inherent sawtooth suppression in lower q_{95} discharges. Furthermore, much progress has been made in efficient electron cyclotron current drive (ECCD) NTM stabilization[45, 104, 105]; routine use of this technique is expected in future devices.

Recent advanced inductive low torque experiments, with similar discharge parameters as are expected in ITER hybrids, have shown a propensity to develop only 2/1 NTMs instead of 3/2 modes. Also, the normalized beta threshold for 2/1 NTM onset is significantly reduced at the low rotation velocities predicted for ITER[106]. These results provide additional motivation for the study of 2/1 hybrid discharges.

4.3.1 Hybrid-like 2/1 Flux-Pumping Discharge

Figure 4.3.1-1 shows a successful hybrid discharge (red) and a similar discharge where a saturated 2/1 tearing mode was generated (black). It can be seen in the black case that β_N drops by ~13%, while beta feedback control causes the neutral beam power to surge from 5 MW to 9 MW in an attempt to sustain the target beta. This degradation in confinement is significant enough that the discharge would not be considered a high performance hybrid. However, the two cases have similar safety factor profiles, with q_{95} ~ 4.4, and q_{min} being maintained above unity. Accordingly, no sawteeth are observed in either case evidenced by the absence of periodic drops in the core soft x-ray signals.

Both plasmas have identical resistance R_p and therefore similar current relaxation times. The discharge containing the 2/1 can be considered "hybrid-like" in that stationary plasma parameters are maintained for times longer than τ_R after the NTM saturates.

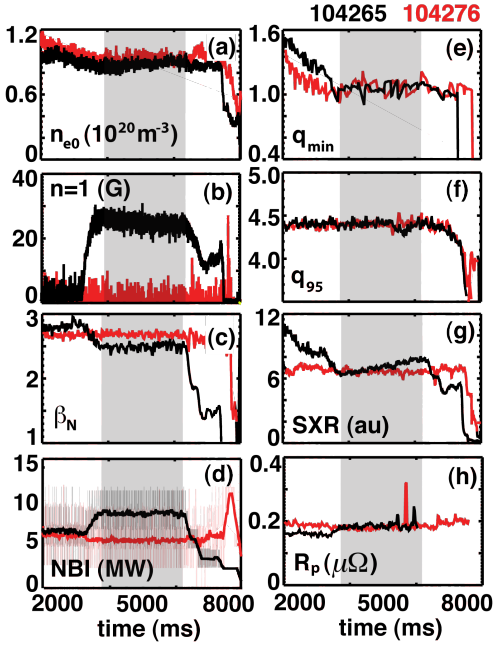

FIG. 4.3.1-1: Black - discharge parameters of a hybrid discharge containing only a 2/1 tearing mode, Red - discharge parameters containing only a 3/2 mode (a) Center electron density (10^{20} m^{-3}) (b) Mirnov probe amplitude of n=1 mode (G) (c) normalized beta (d) Total (light) and averaged (dark) injected neutral beam power (MW) (e) minimum safety factor (f) edge safety factor (g) core soft x-ray signal (arb. units) (h) average plasma resistance ($\mu\Omega$).

During the stationary period of the discharge an average measured MSE pitch angle for each channel is determined 5 ms before, and 5 ms after a series of ELM events. The internal current profile before and after the ensemble average of ELM events is then calculated directly from Ampere's law[103], rather than from an equilibria reconstruction, allowing the average change in the q-profile across the ELM event to be determined.

The periodic change in the q-profile, characteristic of 3/2-hybrid discharges, is also seen for hybrids that develop 2/1 NTMs. Figure 4.3.1-2 shows the change in the q-profile for a poor confinement hybrid-like plasma containing a saturated 2/1 NTM. This change in safety factor is consistent with a shift in the externally driven current density from inside to outside the $q = 2$ surface. The largest increase in the q value inside the 2/1 rational surface is just under 0.06, which is more than twice that measured in a previous work for a 3/2-hybrid at similar q_{95} and normalized beta[64]. Also, the change in q shows a zero crossing at the 2/1 rational surface compared with the 3/2 case zero crossing at $q = 1.5$. For clarity, an illustration of the change in q due to flux-pumping is shown in Fig. 4.3.1-2(b). Notice the safety factor profile pivots about the rational surface minor radius.

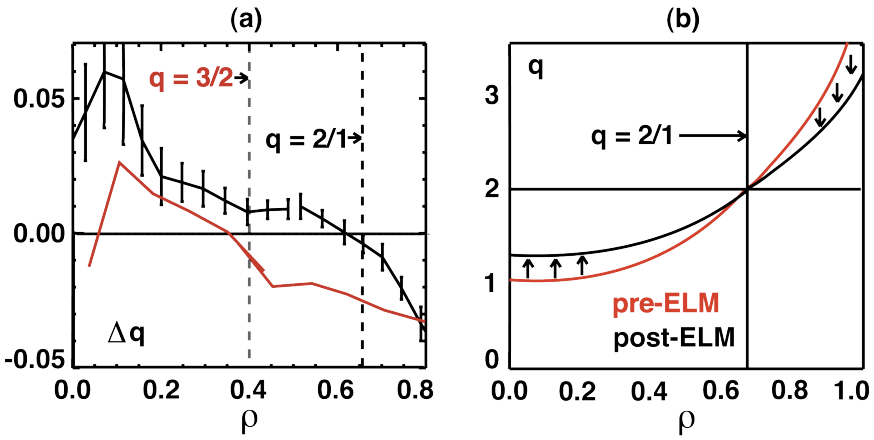

FIG. 4.3.1-2: (a) Black - change in the safety factor profile measured through direct MSE analysis using Ampere's law and ensemble averaged over 44 ELM events for 2/1 flux-pumping. Red – flux-pumping due to 3/2 mode. (b) Illustration of safety factor profile evolution. ρ is the normalized minor radius.

This stronger 2/1 flux-pumping should mean that 2/1-hybrids can operate without sawteeth at lower q_{95}, or with less frequent ELMing. A lower q_{95} discharge with $q_{min} > 1$ requires a broader safety factor profile than higher q_{95} cases. Stronger flux-pumping results in greater flattening of the safety factor profile per ELM event. Recall, lower q_{95} discharges contain smaller relaxed values of q_{min}. For higher q_{95} discharges less frequent ELMs are required since each ELM event produces a greater change in q_{min}.

Previously it was shown that the strength of the ELM-2/1 tearing mode coupling is related to the radial proximity of the ELM to the tearing mode. This agrees with the finding of stronger flux-pumping in the 2/1 case since the 2/1 tearing mode is located closer to the ELMing pedestal than the 3/2 mode.

4.3.2 Effect of Active Suppression

Stronger 2/1 flux-pumping may enable sawtooth free hybrid operation at lower q_{95} and higher β_N for the same ELM frequency as conventional 3/2-hybrids. However, achieving higher normalized fusion performance will require a significant improvement in energy confinement in the presence of the 2/1 mode. Complete suppression[107] and prevention[108] of the 2/1 NTM has shown that $\beta_N \sim 4l_i$ can be achieved in hybrid discharges. While suppressing the 2/1 has extended normalized beta operation, the presence of the expected 3/2 mode and inefficient continuous wave application of ECCD has caused reduced H_{89P} in DIII-D. From this work, it appears that a hybrid containing only a modest sized, partially suppressed 2/1 tearing mode could both improve confinement and produce a flatter average current profile from intrinsic plasma flux-pumping. Future attempts to obtain a high performance non-sawtoothing 2/1-hybrid discharges could benefit from O-point ECCD modulation techniques.[45,104] In this section,

requirements for a partially suppressed 2/1-hybrid are outlined and the effect of active suppression on flux-pumping is shown.

As was seen in the previous section, confinement degradation of a 2/1 tearing mode is greater than that of an equivalent 3/2 island. This is due to the greater minor radius of the 2/1 rational surface, and can be illustrated by considering the magnetic island belt model[47]. The shaded region of Fig. 4.3.2-1 shows the additional stored energy lost from a 2/1 NTM of identical width as a 3/2 mode. Note the cubic relationship between the rational surface minor radius and energy confinement degradation seen in Eq. (2.24) of Section 2.1.4.

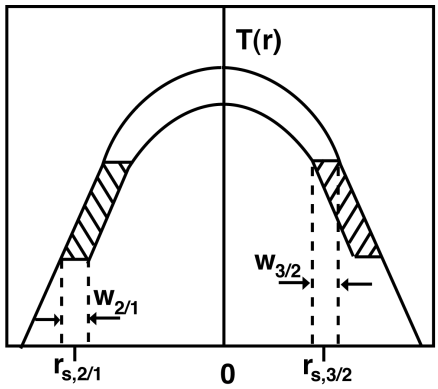

FIG. 4.3.2-1: Cartoon of a full poloidal cross-section temperature profile for a 3/2 and 2/1 NTM of identical width. The shaded area shows the additional confinement degradation of the 2/1 NTM.

Successful sawtooth free stationary hybrid discharges in DIII D have been found to contain 3/2 tearing modes ~ 6 to 8 cm wide[109]. Considering a single 3/2-hybrid q-profile, for the 3/2 mode $r_s \sim 26$ cm, where as for the 2/1 mode $r_s \sim 36$ cm. For an 8 cm 3/2 island the confinement is degraded by 8.3% according to the belt model. To obtain identical confinement degradation for the 2/1 mode, the island must be suppressed to less than 3 cm wide. Note, the island widths calculated throughout this work use a large aspect ratio approximation[91], proportional to the square root of the poloidal field fluctuation amplitude ($\tilde{B}_\theta$) measured at the wall by a Mirnov probe, and a 2/3 correction measured using ECE.

Beyond fusion performance, stability to tearing mode locking[110] will ultimately limit the allowable 2/1 or 3/2 island size[111] for hybrid discharges. For ITER low q_{95} discharges, it has been estimated that 2/1 and 3/2 island full widths will be limited to less than 5 and 8 cm, respectively to avoid locking[112, 113] and potentially causing a disruption. Previous work[63] has shown that complete suppression of 3/2 NTMs in stationary hybrid discharges results in the prompt return of sawteeth, proving that the presence of the mode is critical to maintaining sawteeth stability. Active control algorithms have already demonstrated on DIII-D complete suppression of both 3/2 and 2/1 NTMs is possible using ECCD[114].

In Fig. 4.3.2-2 a hybrid discharge with $q_{95} \sim 4.3$ is generated. Once the discharge reaches stationary plasma conditions, the neutral beam injected power is surged to rapidly increase β_N and deliberately destabilize a 2/1 NTM. Once the tearing mode is generated,

neutral beam heating is returned to the level applied prior to the creation of the mode. This is followed by active suppression of the mode by applying ECCD from two gyrotrons focused at the 2/1 rational surface. At ~5700 ms the 2/1 mode amplitude is completely suppressed. Immediately after suppression, sawteeth appear for the first time in the discharge. This is a nearly identical finding as the 3/2 suppressed case[63]. The sawteeth are not believed to be coincident with changes in the overall current profile, and instead result from the loss of the 2/1 mode.

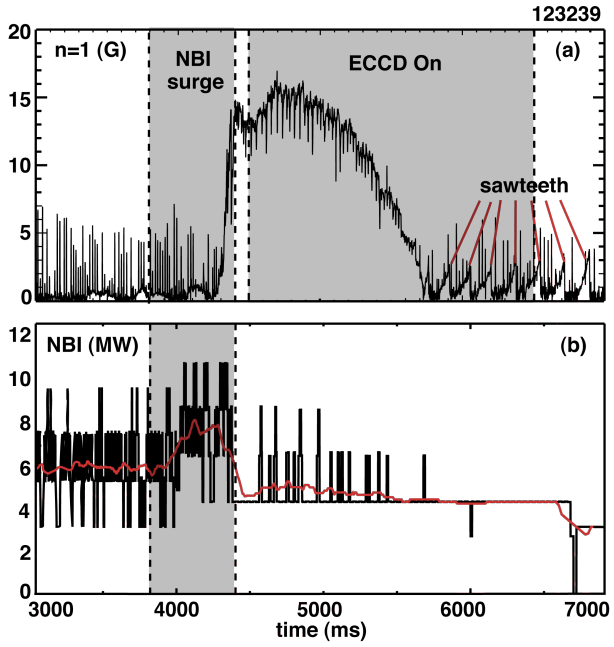

FIG. 4.3.2-2: (a) The amplitude of an n = 1 tearing mode (G) followed by sawteeth after complete suppression, (b) total neutral beam injected power (MW).

Flux-pumping is present during the partially suppressed period of the 2/1 NTM. Figure 4.3.2-3 shows flux-pumping profiles taken from an ensemble average of 51 ELM-NTM coupling events. The data was taken over the 4500 ms to 5500 ms period of the discharge shown in Fig. 4.3.2-2, where ECCD is actively suppressing the mode but hasn't completely suppressed it. A clear inversion of the magnetic field strength, safety factor and externally driven current density profiles (including Ohmic) at the 2/1 rational surface can be seen. Also, there is a characteristic spike in the bootstrap current density at the 2/1 rational surface, which is consistent with an increase in the pressure gradient during the island shrinking. This J_{BS} is determined from a direct MSE measurement of the Pfirsch-Schlüter current density and the application of neoclassical theory in a simplifying limit[103]. Note, the smaller than expected increase in q_{min}, and decrease in core J_{CD} indicate that the net plasma current increased at the ELM crash, which is unlikely. This can be partly explained by the fact that only changes due to ELMs are considered in this analysis and a correction for the overall evolution in the current profile was not applied.

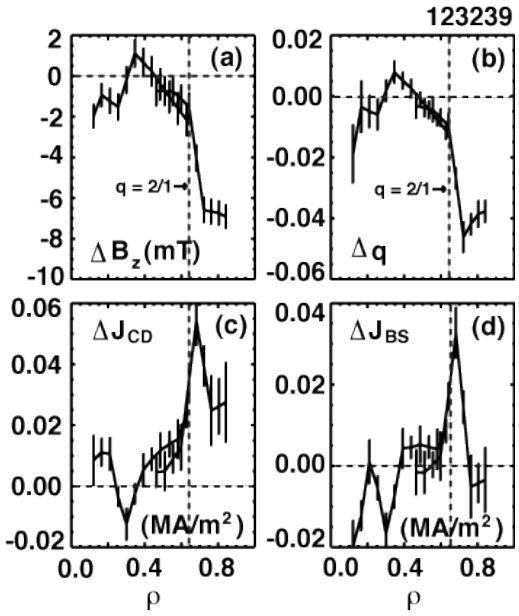

FIG. 4.3.2-3: Changes in radial profiles during ELM-NTM coupling events for (a) vertical magnetic field strength (mT), (b) safety factor, (c) externally driven current density (MA/m^2), and (d) bootstrap current density (MA/m^2). The profiles where determined from ensemble averaging MSE data 51 ELM-NTM coupling events.

Previous work has shown 3/2-hybrid flux-pumping is strongest at higher β_N values [Ref. 64, Fig. 5]. Of the two discharges the lower β_N (lower flux-pumping) case had sawteeth. Further analysis of these discharges show that for the same average neutral beam power the smaller β_N case also has a 12% larger 3/2 island. This can be seen in Fig. 4.3.2-4. Recall[115] $w_{sat} \propto \beta_p L_q / L_p$, where w_{sat} is the saturated island width, L_p and L_q are the pressure gradient length and magnetic shear length, respectively. Therefore, a difference in the pressure or safety factor profile can result in a different saturated island width for the same beta. In discharge 123204, larger L_q and smaller L_p resulted in a larger island at smaller β_N. This might suggest a favorable relationship exists between flux-pumping strength and a smaller island. However, it will be shown later that flux-pumping does not depend on island width.

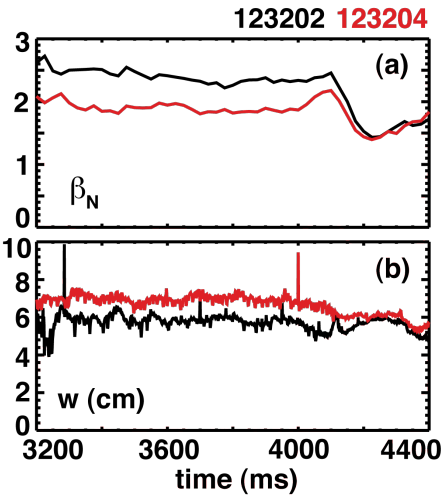

FIG. 4.3.2-4: For two shots showing different 3/2 flux-pumping in Ref. 9: (a) normalized beta (b) full island width (cm) measured by a Mirnov probe array.

To further elucidate hybrid flux-pumping two parameters must be defined. The strength of the flux-pumping is taken as the total displacement of the safety factor across the rational surface (Δq_{tot}). This is found by taking the difference between the maximum and minimum values of the Δq-profiles. The distance between the tearing mode and the ELMing pedestal ($\Delta\rho_{ped}$) is defined as the difference between the normalized minor radius (ρ) at the rational surface and ρ at q_{95} ($\rho \leq 1$). Table 4.3.2-1 compares the flux-pumping strength, proximity to the ELM region, normalized beta and island width for the discharges discussed.

Table 4.3.2-1: Comparison of flux-pumping strength; the discharge number, the tearing mode poloidal (m) and toroidal mode numbers (n), flux-pumping strength (Δq_{tot}), distance between the mode rational surface and q_{95} in terms of normalized poloidal flux ($\Delta\rho_{ped}$), normalized beta (β_N), and average island width (w).

Discharge	m/n	Δq_{tot}	$\Delta\rho_{ped}$	β_N	w (cm)
104268	2/1	0.10	0.36	2.5	8.5
123239	2/1	0.06	0.30	1.9	6.4
123202	3/2	0.06	0.51	2.7	5.8
123204	3/2	0.02	0.45	1.9	6.6

The flux-pumping strength is predominantly dependent on β_N and the proximity of the mode to the edge pedestal, and appears invariant with respect to the island size. For the same β_N and nearly the same island width (123204 and 123239) the mode closer to the pedestal (123239) shows a factor of three stronger flux-pumping than the larger distance case (123204). The two cases containing 2/1 modes (104268 and 123239) have roughly the same proximity to the pedestal, but the larger β_N case (104268) has the

stronger flux-pumping. This β_N dependence is also true for the previously published[64] 3/2 mode discharges (123202 and 123204). The strongest overall flux-pumping (104268) occurs when both the proximity to the ELM and β_N are greatest. Likewise, the weakest flux-pumping (123204) occurs when both β_N is low and the island is furthest from the pedestal. While independent variation of the island width is required to draw any strong conclusions, there appears to be no clear connection between the size of the island and the strength of the flux-pumping. This suggests that the rational surfaces of the respective island chains are serving only as radial surfaces around which the safety factor is able to pivot. Partial suppression of the island chains should therefore not impede flux-pumping, rather the higher achievable β_N afforded from the improved energy confinement, should amplify it.

This finding parallels the result of the previous section where greater proximity of the ELM (depth) to the tearing mode caused greater ELM-NTM coupling. Here, instead of the most unstable mode of the ELM approaching the NTM rational surface, the tearing mode rational surface of the 2/1 NTM is closer to the ELMing pedestal then the surface of the 3/2 mode.

4.4 MHD Interference with Pedestal MSE

Large and erratic uncertainties in MSE signals in the H-mode pedestal have left the current profile of this important region mostly unmeasured. An effort is currently underway to upgrade the optical narrowband filters for these channels to improve their discrimination between σ and π light and therefore increase their SNR. Furthermore, a new spectrometer has been installed and efforts are underway to make the first full spectral measurement of the Stark split spectra to verify that it is free of impurity lines.

The following section presents the discovery of, and solution to, a polarimeter-plamsa interaction, which causes the MSE measured polarization angles to be invalid during temporally localized regions of MHD activity. This finding is only one example of the self-diagnosis capabilities enabled through the use of fast MSE Fourier analysis.

4.4.1 Strong Edge Density Fluctuations

MSE sideband fluctuations containing $\tilde{\gamma}$ and $\tilde{A}_{s,c}$ components are strongest in the large density gradient pedestal ($\rho \geq 0.92$) of H-mode discharges. Because rotating core NTMs cause small radial field displacements $\tilde{B}_R$ in the pedestal, it is believed these displacements produce large density fluctuations as they sweep the steep density gradient past the stationary MSE channel field of view. This suggests that the dominant sideband component in the pedestal is $\tilde{A}_{s,c}$, which is proportional to $\tilde{n}$. An illustration of these strong density fluctuations is provided in Fig. 4.4.1-1.

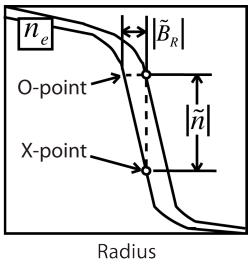

FIG. 4.4.1-1: An illustration of a radial field displacement shift of the electron density profile. The open circle represents the location of an MSE channel. The $\tilde{n}$ and $\tilde{B}_R$ amplitudes are shown at the X and O point of the tearing mode.

The density profile is extended outward at the island O-point, and returns it to an island-free position at the X-point. As was discussed previously, MSE light results from neutral beam-stimulated emission, which makes the MSE sensitive to changes in plasma density. As the island rotates from the X-point to the O-point the density at the MSE channel location increases. The reverse occurs as the X-point realigns with the channel.

The net result is a large density fluctuation correlated with the tearing mode rotation frequency.

4.4.2 Polarimeter-Plasma Interaction

Magnetic islands are roughly symmetric about their rational surface. Therefore measurement of fluctuating quantities ($\tilde{n}_e$, $\tilde{T}_e$, or $\tilde{B}_z$) on opposite sides of the rational surface should exhibit a 180^0 phase inversion. Since the MSE fluctuations are not always visible near the rational surfaces, this inverse phase technique has not been exploited for identifying the mode. Instead the modes seen by the MSE have been identified through correlation with other diagnostics. MSE spectrograms show NTM fluctuations that correlate with the frequencies measured by a toroidal array of Mirnov magnetic coils. A magnetic probe array allows the toroidal mode number to be determined using the code NEWSPEC[89]. For the sample discharge shown in Fig. 4.4.2-1, the toroidal mode number was found to be $n = 1$. For $n = 1$, the mode frequency of toroidal rotation should match that of the bulk plasma rotation. At ~3400 ms an ~8 kHz mode can be seen. Charge exchange recombination[116] (CER) measurements of the impurity toroidal velocity (v_{tor}) profile show that $v_{tor}/2\pi R$ = 8 kHz at $\rho \approx 0.4$, corresponding to a safety factor of 2. Therefore the mode is located at the $q = 2$ rational surface implying the poloidal mode number is $m = 2$. This is likely a 2/1 neoclassical tearing mode (NTM). This procedure, as well as the measurement of $\tilde{T}_e$ using electron cyclotron emission radiometry[92], identifies both the toroidal and poloidal mode number of the modes seen in MSE spectrograms.

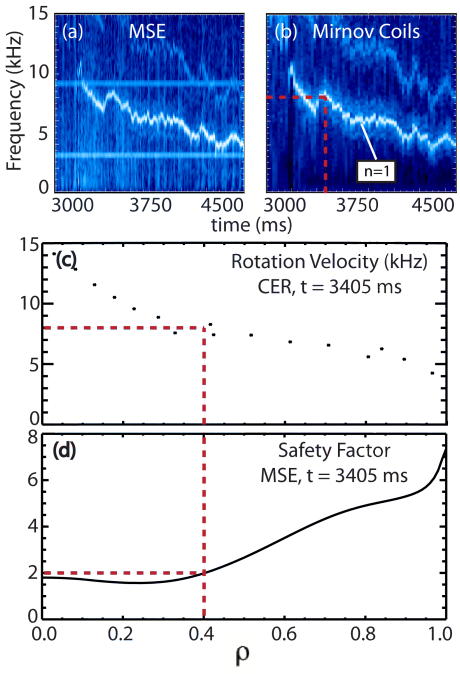

FIG. 4.4.2-1: (a) MSE spectrogram, (b) Mirnov coil spectrogram with toroidal mode number identified (n = 1 RMS mode amplitude is ~34 G), (c) CER rotation frequency, (d) MSE q-profile (shot 140702).

During strong periods of MHD activity, intensity (ω) and sideband ($2\omega_1 + \omega$ and $2\omega_2 - \omega$) fluctuations have been found to mix with the second harmonic PEM frequencies ($2\omega_1$ and $2\omega_2$), resulting in a superposition that causes significant errors in measured γ. For the same discharge shown in Fig. 4.4.2-1, Fig. 4.4.2-2 shows three time range windows: A, B, and C. In time window B (2450–3150 ms), a $n = 3$ NTM intensity fluctuation crosses the 2nd harmonic frequencies at 40 and 46 kHz. Note, Fig. 4.4.2-2(b) is simply a highlighted cartoon of the spectrogram of Fig. 4.4.2-2(a) to emphasize the component frequencies of interest. In Fig. 4.4.2-2(d), it can be seen that during time range B there is a notable increase in the γ noise.

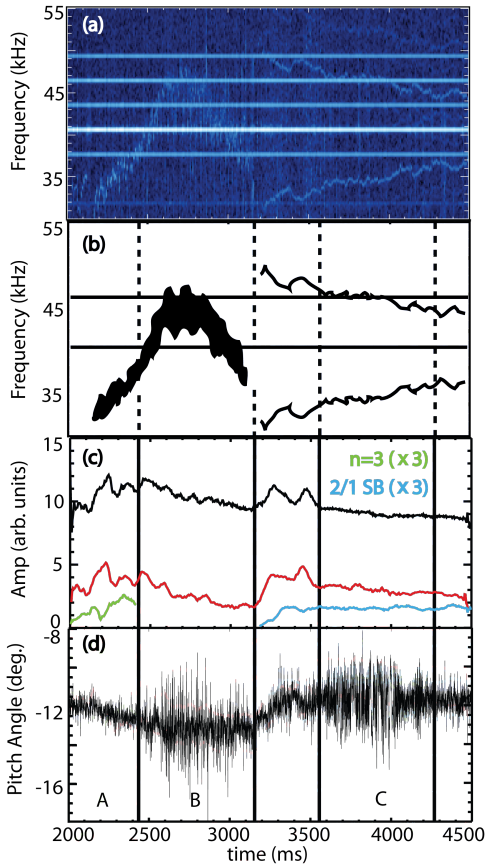

FIG. 4.4.2-2: (a) MSE spectrogram at ρ = 0.92, (b) Important regions of the spectrogram include 40 and 46 kHz second harmonic signals, a $n = 3$ tearing mode intensity fluctuation at 2200 ms to 3100 ms, and 2/1 tearing mode sideband fluctuations $2\omega_1 - \omega$ and $2\omega_1 + \omega$ at 3200 ms to 4500 ms, (c) box-car smoothed Fourier recovered amplitudes for 40 kHz (black) 46 kHz (red) $n = 3$ (green triangle) and 2/1 sideband $2\omega_1 - \omega$ (blue circle), (d) measured γ (shot 140702).

In window C a $2\omega_1 + \omega$ sideband fluctuation crosses the $2\omega_2$, 46 kHz frequency, and results in an increase in the γ noise comparable to that seen in time range B. Note that the greater the polarization fraction the more apparent the sidebands become. The typical polarization fraction for MSE on DIII-D is around 0.85. The sideband fluctuation in time range C corresponds to a 2/1 NTM intensity fluctuation seen in Fig. 4.4.2-1(a). Through most of time range C the sideband fluctuation exactly overlaps the 46 kHz instrument frequency. The standard deviation of γ from 3600 to 4100 ms is 1.07 degrees, whereas the standard deviation of the same channel for shot 140691 without MHD is only 0.37 degrees. This suggests MHD interference in time range C caused a factor of 3 increase in the noise of the calculated magnetic field polarization angle γ.

While this analysis focuses on NTM fluctuations, other higher frequency MHD, like toroidal Alfvén eigenmodes (TAE), have also been observed on MSE spectrograms at frequencies 50 to 160 kHz.

4.4.3 ELM Verification

ELMs have been observed on MSE lock-in signals for channels focused near the edge pedestal. ELMs are known to cause radial particle transport from the pedestal to the scrape-off layer[117] producing local variations in density and temperature at a fixed radius[118]. Because the MSE relies on beam-stimulated emissions, the light collected is a product of neutral beam current density and the plasma density[36]. The neutral beam current density remains constant, so variations in the light intensity are caused by variations in plasma density only. Note, $A_{s,c}$ is proportional to electron density. Because γ is computed by taking a ratio of the amplitudes of $2\omega_1$ and $2\omega_2$ the intensity difference due to an ELM divides out. Figures 4.4.3-1(a) and (b) show that the normalized lock-in [$A_s \sin(2\gamma)$ and $A_c \cos(2\gamma)$] signals for time range A of Fig. 4.4.2-2 track one another and are correlated with the ELM signature D_α emissions measured by filterscopes.[119]

It can be seen in Fig. 4.4.3-1 (a) and (b) that $A_s \sin(2\gamma)$ and $A_c \cos(2\gamma)$ for edge pedestal MSE channels should correlate with the D_α emissions of the filterscopes. This means the filterscopes can serve as a diagnostic for confirming the expected pattern of the lock-in recovered signals. In Fig. 4.4.2-2(a), only the $2\omega_1 \pm \omega$ sidebands are visible, and the $2\omega_2 \pm \omega$ sidebands are below the noise floor of the spectrogram. Only the $2\omega_1 + \omega$ sideband intersects the $2\omega_2$ instrument frequency at 46 kHz. This means that the $A_c \cos(2\gamma)$ signal should show the greatest deviation from the characteristic ELM pattern if sideband interference is the cause of the errors in γ. Figures 4.4.3-1 (c) and (d) show this to be the case: for the time period C of Fig. 4.4.2-2, the $A_s \sin(2\gamma)$ output still tracks the D_α emissions, while $A_c \cos(2\gamma)$ shows almost no correlation with the filterscopes.

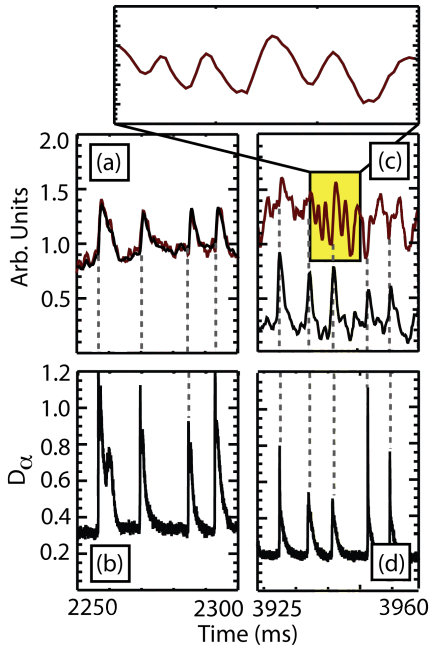

FIG. 4.4.3-1: For channel 44 located at ρ = 0.92 within time period A of Fig. 4.4.2-2: (a) Normalized 40 kHz $A_s\sin(2\gamma)$ (black) and 46 kHz $A_c\cos(2\gamma)$ (red) lock-in (LI) signals free of MHD contamination. (b) Filterscope measurement of ELMs. For the same channel later in time range C of Fig. 4.4.2-2: (c) Normalized 40 kHz $A_s\sin(2\gamma)$ (black) signal showing no MHD contamination and 46 kHz $A_c\cos(2\gamma)$ (red) LI signal showing MHD contamination resulting in a beat frequency. (d) Filterscope measurement of ELMs (shot 140702).

Upon closer inspection, around 3935 to 3950 ms, a 100–350 Hz oscillation can be seen on the $A_c\cos(2\gamma)$ output of Fig. 4.4.3-1(c). The MSE spectrum at this time, shows a difference in the sideband frequency and the 46 kHz instrument frequency of ~300 Hz. This indicates the $A_c\cos(2\gamma)$ oscillation results from the slight difference in the sideband frequency and the PEM reference frequency, such that demodulation at the phase sensitive detector of the lock-in results in a low frequency beating output $f_{beat} = f_{46\text{kHz}} - f_{\text{MHD}}$, which is of low enough frequency to pass through the active low pass electronic filter of the lock-in.

Shortly after time range C of Fig. 4.4.2-2 at 4490 ms, the frequency of the sideband is ~1.5 kHz lower than the 46 kHz instrument frequency while its amplitude is nearly identical. Despite having the same amplitude at 3940 ms, the relatively rapid 1.5 kHz beating is filtered by the lock-in, and therefore does not contaminate γ.

This suggests the mechanism causing the error in γ is a superposition of MHD fluctuations onto the second harmonic instrument frequencies. Because the phase of the MHD is arbitrary with respect to the phase of the instrument this superposition can result in either constructive or destructive interference. Additionally, the variation in the MHD frequency causes lock-in beating during mixing. This results in a temporally localized period when the outputs of the lock-ins are no longer proportional to $A_s\sin(2\gamma)$ or $A_c\cos(2\gamma)$, such that γ calculated from their ratio is no longer valid. The criteria for the

occurrence of this error is when $\omega \rightarrow 2\omega_1$ and/or $\omega \rightarrow 2\omega_2$, or $2\omega_1 + \omega \rightarrow 2\omega_2$ and/or $2\omega_2 - \omega \rightarrow 2\omega_1$.

Figure 4.4.2-2(c) shows the sideband amplitude is ~20% as large as the amplitude of the instrument at 46 kHz. Interference of this magnitude is significant and certainly explains the major polarization angle variations seen. To illustrate the MSE sensitivity to such interference, consider a nominal γ value for channel 44 ($\rho = 0.92$) of -12^0. This means the ratio of $A_s \sin(2\gamma)$ over $A_c \cos(2\gamma)$ is ~ –0.445. Applying a 20% change to this ratio and re-computing gives –9.8 degrees < γ < –14.1 degrees, a difference of 4.3^0, which is right in line with the ~ 5^0 variation seen in Fig. 4.4.2-2(d).

The data for this work was acquired during a high β experiment with frequent MHD activity. During this experiment 13 of 35 discharges showed some form of temporally localized error associated with MHD interference. When these errors occurred they were seen across all 18 edge pedestal channels with $\rho < 0.9$.

4.4.4 Effect on EFIT Computed Safety Factor

While the main concern of this MHD interference finding pertains to accuracy of edge pedestal field measurements, it has also been found that including contaminated edge channels in equilibria reconstructions can significantly impact the calculated *q*-profile near the plasma core. This section is intended to illustrate the importance of removing these erroneous channels from equilibria reconstruction and should not be considered a reflection of the accuracy of the MSE diagnostic as a whole. Recall, the observed interference errors have only been observed in the edge pedestal MSE channels during H-mode discharges.

Channel 44 is a part of the tangential MSE array on DIII-D, is considered a low noise channel, and is routinely used in EFIT[96] equilibria reconstructions. Because of photon statistics MSE data supplied to EFIT is typically averaged over a 10 ms period. For this averaging time the calculated uncertainty for γ measurements is ~0.1 degrees[98]. Figure 4.4.4-1 shows the 10 ms averaged values of γ for shot 140702 for an edge channel 44 containing MHD interference, as well as two channels located radially inward where no MHD interference has been observed. It can be seen that the edge channel exhibits ~3 degrees variation in averaged γ, or about 30 times greater variation than the typical uncertainty of the measurement. At 4000 ms (the yellow box of Fig. 4.4.4-1) the calculated γ of the outermost channel 44 $\rho = 0.92$ crosses that of channel 43 $\rho = 0.77$, producing a potentially nonphysical result.

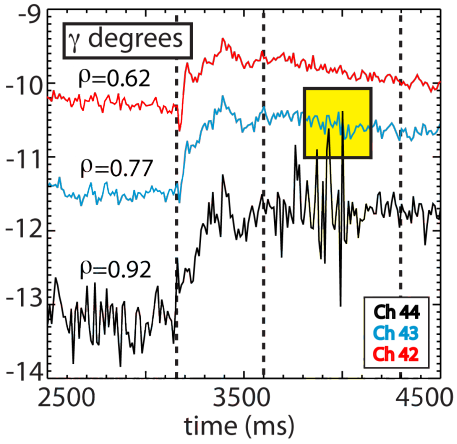

FIG. 4.4.4-1: Polarization angles averaged over 10 ms for edge ρ = 0.92 channel 44 containing MHD interference (black), and adjacent channels 43 and 42 inside the edge ρ = 0.77 and ρ = 0.62 with no MHD interference (blue triangle and red diamond). The yellow box represents a period that is potentially non-physical (shot 140702).

An EFIT equilibrium reconstruction was first computed over a 10 ms averaging window at 4000 ms using MSE data from 15 routinely used tangential array channels, which included the MHD interference-effected channel 44. Then the value of γ for only channel 44 was set to the outlying values –10.50 degrees and –13.25 degrees seen in Fig. 4.4.4-1 at 4000 ms. The other 14 channels were left unchanged, and for these three cases (γ = –10.50 degrees, γ = –13.25 degrees, and default γ = –11.12 degrees) new equilibria were run. The resulting *q*-profiles can be seen in Fig. 4.4.4-2. A 38% difference in *q* can be seen at ρ ~ 0.67 for the outlier-computed equilibria. This corresponds to the measured rational surface being either 3 or 4, depending on the outlier selected. The minimum *q* shows <1% variation between the two cases. Note that EFIT has many versions constrained by different diagnostic inputs. The version of EFIT considered in this section utilizes MSE and magnetics data to quickly reconstruct the equilibria between shots.

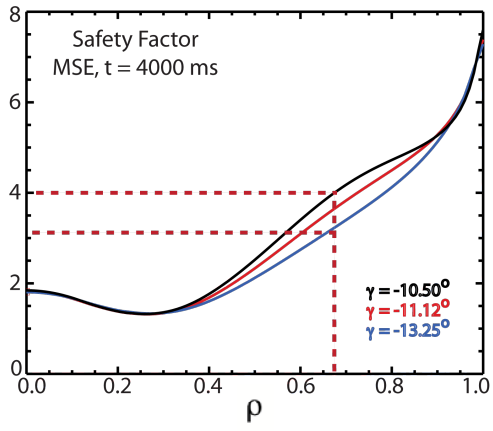

FIG. 4.4.4-2: Range of safety factor profiles possible when outlying values of averaged γ, caused by MHD interference, are used for edge channel 44 at ρ = 0.92 (shot 140702).

The exact numerical rationale for this EFIT computed variation in q is beyond the scope of this work. One reason for the non-localized nature of the error is that the measured plasma current defines the total poloidal flux used in EFIT. Since this key constraint was maintained constant in each case, any change in γ requires that EFIT adjust the q-profile to conserve the total poloidal flux. Also note, in EFIT MSE data is weighted according to the standard deviation of the polarization angles for a specified time interval centered about the requested time. The standard deviation of γ's used in the EFITs of Fig. 4.4.4-2 were from a 3990 to 4000 ms time interval, where γ variations were greatest, and therefore the channel weighting was small. Even with the relatively small weighting of these γ's, significant effects on the q-profile are apparent.

4.4.5 Interference Avoidance

One path to potentially limiting the severity of MHD interference would be to reduce the cutoff frequency of the analog lock-in output low pass filter, however this is not a desired solution, as it will diminish the time-resolution needed to track legitimate plasma variations. Aggressive electronic filtering of the lock-in inputs will reduce but not eliminate the error, particularly at crossing points where the contamination frequency equals that of the instrument.

An advantage to recovering all of the spectral information contained within the MSE signal is that other polarization measurements can be made. For example, the fourth PEM harmonic provides a redundant measure of linear polarization at frequencies that are high enough (80 and 92 kHz) and with a large enough bandwidth (12 kHz instead of 6 kHz) to avoid the MHD interference seen in shot 140702. γ is recovered from the fourth harmonic through nearly an identical expression as the second harmonic. The intensity-modulated signal for the fourth harmonic is given by,

$$I_{PMT} = A_{s,4}\sin(2\gamma)\cos(4\omega_1 t) + A_{c,4}\cos(2\gamma)\cos(4\omega_2 t)\ , \tag{4.10}$$

and γ is then recovered through the ratio,

$$\frac{A_{s,4}\sin(2\gamma)}{A_{c,4}\cos(2\gamma)} = \frac{J_4(A_1)}{J_4(A_2)}\tan(2\gamma) \tag{4.11}$$

Note the PEM retardation settings, $A_1 = A_2 = \pi$. In order to calculate γ using existing calibration values, the fourth harmonic amplitudes must be linearly scaled to the second harmonic lock-in outputs at a time where the signal is unaffected by MHD interference. Once this ad-hoc calibration is applied, the new amplitudes can be used to calculate γ.

To prove the validity of this calibration technique it was first applied to the Fourier recovered second harmonic. Figure 4.4.5-1 shows that while Fourier recovery of

the second harmonic amplitude does indeed result in an identical γ measurement as the lock-in, the fourth harmonic has significant additional noise. In fact, the noise of this fourth harmonic Fourier recovered signal is greater than the MHD interference error. This may be due in part to the ~3.2 times smaller fourth harmonic amplitude. The second harmonic amplitude scales as the second order Bessel function of the first kind $J_2(A_{1,2}) \approx 0.485$, where as the fourth harmonic amplitude scales as the fourth order Bessel function $J_4(A_{1,2}) \approx 0.151$. The smaller signal-to-noise (SNR) associated with the fourth harmonic limits it usefulness to only a very coarse recovery of γ. However, SNR proportionality to $\sqrt{I}$ [120] doesn't explain the full noise envelope of Fig. 4.4.5-1. The additional noise may result from higher order sideband harmonic contamination. Specifically, the second harmonic (n = 2) frequency of the 2/1 NTM exceeds the 12 kHz bandwidth of the MSE fourth harmonics.

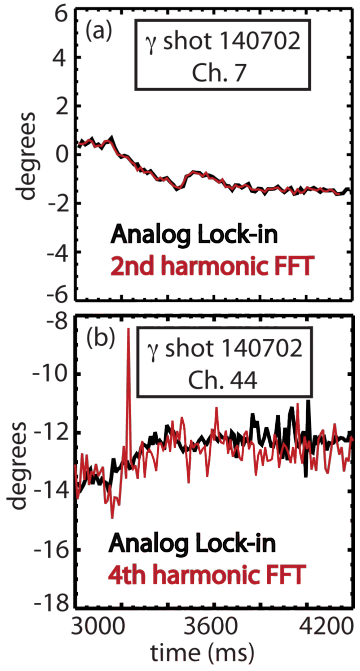

FIG. 4.4.5-1: (a) γ for channel 7, calculated from Fourier recovered second harmonic amplitudes (red), and analog lock-in recovered second harmonic amplitudes (black). (b) γ for channel 44, calculated from Fourier recovered fourth harmonic amplitudes (red), and analog lock-in recovered second harmonic amplitudes (black) (shot 140702).

Digitally filtering the sideband interference from the second harmonic may be possible using information provided by the non-interfering sideband. Equation (4.2) shows the amplitude of the $2\omega_1 - \omega$ sideband is equal to the amplitude of $2\omega_1 + \omega$ sideband. In the case shown in Fig. 4.4.2-2 time range C it can be seen that the sideband causing interference is $2\omega_1 + \omega$. By accurately recovering the amplitude and phase of the non-interfering sideband $2\omega_1 - \omega$, applying a 90^0 phase shift, and adding the result at the $2\omega_1 + \omega$ sideband frequency to the time domain of the PMT signal, it may be possible to cause destructive interference that would effectively remove the interfering

sideband. This filtering technique has not been tested, and even if successful, would not allow for real time corrected measurements of γ.

The preceding observations demonstrate a polarimeter-plasma interaction that is independent of the specific atomic physics of the MSE diagnostic. For this reason, other dual PEM tokamak polarimeters focused on Zeeman splitting[121, 122] may be sensitive to this error as well.

While post-process digital filtering could reduce this MHD interference error, there is no known way of restoring the real-time γ measurement through any digital signal processing technique. For this reason, future edge pedestal tokamak polarimeter systems should avoid MHD interference all together. While the use of higher harmonics from existing tokamak PEMs may avoid this interference, doing so requires a significant increase in signal intensity to improve signal-to-noise. The use of PEMs with second harmonic frequencies greater than the MHD intensity oscillations, and with greater frequency separation such that $2\omega_1 + \omega \neq 2\omega_2$, and $2\omega_2 - \omega \neq 2\omega_1$, could avoid MHD interference without strict signal intensity requirements. The size of the birefringent PEM crystal dictates the fundamental frequency at which it can be modulated. The smaller the crystal size the higher oscillating frequency it can achieve. Therefore, the use of smaller aperture PEMs would reduce the viewing angle that a dedicated edge polarimeter could span. However, since the observed error is isolated to the relatively narrow region of the edge pedestal a large viewing angle would not be required.

Higher frequency mode activity, such as toroidal Alfvén eigenmodes (TAE), should serve as a guide for the minimum allowable edge PEM frequency. Because TAE intensity fluctuations have been observed on MSE spectrograms at frequencies ranging from 60 to 150 kHz in DIII-D, the minimum PEM second harmonic frequency should exceed 150 kHz, making the suggested fundamental frequencies greater than 75 kHz.

Chapter 5

Future Research and Conclusions

5.1 Summary

The aim of advanced tokamak scenarios is creating high gain H-mode discharges with little or no inductive current for steady state electrical generation. To achieve the desired performance criteria at lower current requires improved confinement and larger beta. A feature of the advanced inductive hybrid discharge is that it contains a 3/2 NTM, but good confinement. It was found by Petty that hybrids maintain a flat safety factor profile and avoid sawteeth due to pumping of poloidal flux (a.k.a. "flux-pumping") about the 3/2 rational surface. This dissertation presents the first instance of hybrid-like Alfvénic current profile redistributions associated with 2/1 NTM-ELM coupling.

To ensure uniformly accurate flux-pumping measurements a fast data acquisition system was installed on the MSE of DIII-D, comprised of digital lock-in amplifiers and 500 kHz multichannel digitizers. The successful implementation of the DLI system requires matching the accumulator interval of the lock-in to the periods of the PEMs oscillations.

ELM coupling with 2/1 NTMs has been found. With the new hardware in place, MSE measurements show flux-pumping that is more than two times stronger for 2/1 NTMs than for typical hybrid discharges containing 3/2 tearing modes. This 2/1 flux-pumping maintains a safety factor profile that is stable to sawteeth. The strength of flux-pumping has a clear upward dependence on normalized beta and the proximity of the mode to the ELMing pedestal. The presence of the mode is required for flux-pumping to occur, but the strength of the pumping does not depend on the size of the island. The island serves only as a radial pivot surface around which poloidal flux is pumped from the core to the edge. Thus, a hybrid discharge containing a partially suppressed 2/1 NTM may outperform existing hybrids by permitting sawtooth free operation at lower q_{95} and higher beta.

ELM-NTM coupling consists of an Alfvénic timescale drop in the island width followed by a resistive recovery. The recovery can be described analytically by applying a downward going impulse perturbation to the modified Rutherford equation. The drop in island width increases as the size of the ELM increases. The size of the ELM (degree of particle expulsion) is dependent upon the depth of the instability[54]. Therefore, the larger an ELM the closer it is to an NTM with constant radius. This parallels the previously mentioned flux-pumping proximity finding.

All fusion gain ITER scenarios will operate in H-mode. Presently a complete model describing the transition to and sustainment of this regime does not exist. Highly resolved internal measurement of the pedestal current profile is needed to validate any complete H-mode model. A design modification to existing pedestal tokamak dual PEM polarimeters is suggested in this dissertation, which provides a partial step toward resolved pedestal current measurements.

Full spectral analysis of MSE signals reveals a clear polarimeter-plasma interaction that is detrimental to pedestal measurements. This localized error originates from small radial displacements in the edge pedestal caused by coherent core MHD. These small radial displacements give rise to large electron density oscillations that interfere with polarimeter modulations. To resolve this error higher frequency PEMs should be employed. Specifically, PEMs with fundamental frequencies greater than 75 kHz should be sufficient to avoid even relatively high frequency energetic particle induced toroidal Alfvén eigenmodes.

5.2 MSE Improvements

Measurements of internal NTM structure and flux-pumping dynamics could be improved with further work. Specifically, extending fast MSE measurements to include magnetic fluctuations could validate existing MHD models. Through improved temporal resolution, safety factor profile measurements of individual flux-pumping events may be possible, obviating the need for ensemble averaging. Both of these goals can be addressed through increased signal strength.

In the case of NTM magnetic fluctuation measurements, initial results showed a signal-to-noise ratio (*SNR*) of 2. Physical meaningfulness, comparable to that of other fluctuation diagnostics, requires a minimum *SNR* of 10. Electronic noise due to signal processing hardware is two orders of magnitude less than that originating at the detector. While improved quantum efficiencies of alternative detection methods (e.g. avalanche photodiodes) may result in as much as a factor of two improvement in detection over existing PMTs, this improvement will be insufficient to achieve the *SNR* ~ 10 goal. Signal attenuation in the fiber optic cables was measured to be negligible. Similar small losses are known for other components in the optical train. The greatest signal improvement, of ~20%, was obtained by cleaning deposits from the inside surface of the MSE vacuum window. By process of illumination, it appears that an increase in the plasma signal strength is required to achieve the desired *SNR*.

Because $SNR \propto \sqrt{I}$, where I is signal intensity, it is estimated that improving the existing *SNR* by a factor of 5 will require a 25 times increase in the light intensity. Note that this represents a minimum value to achieve physically meaningful data. Extending the fast MSE measurement to provide real-time reconstructions of magnetic island structure will require further improvement in signal strength.

As was mentioned previously, the temporal resolution of an equilibrium reconstruction using MSE is limited by photon statistics to 10 ms of averaged data. Beyond photon statistics, the upper limit of the temporal resolution for a dual PEM polarimeter is defined by the period of the slowest oscillating PEM. On DIII-D the slowest PEM period is ~25 μs. Efforts to increase signal will reduce the required integration time for each equilibrium reconstruction, and therefore increase the temporal resolution of safety factor profiles. For q-profiles generated every millisecond, flux-pumping should be observable for individual ELM-NTM coupling events.

Because both temporal resolution and fluctuation measurements will benefit from increased signal strength, future MSE work will focus on obtaining additional stimulated emissions.

References

[1] Bromberg, Joan Lisa, Fusion: Science, Politics, and the Invention of a New Energy Source, MIT Press, Cambridge, Massachusetts, (1982).
[2] Krane, Kenneth S., Introductory Nuclear Physics, John Wiley and Sons Inc. (1988).
[3] Fowler, T. Kenneth, The Fusion Quest, The Johns Hopkins University Press (1997).
[4] International Panel on Climate Change, IPCC Fourth Assessment Report: Climate Change 2007, Chapter 4.3.2.5 (2007).
[5] Freeman, Marsha "The True History of The U.S. Fusion Program – And Who Tried To Kill It" 21st Century Science & Technology 15 (Winter 2009/2010).
[6] The Magnetic Fusion Energy Engineering Act of 1980, Bill H.R. 6308, Signed into law by President Jimmy Carter Oct. 7, 1980.
[7] http://www.iter.org.
[8] J.D. Lawson, Proc. Phys. Soc. 70, pt. 1, 455, B, 6-10 (1957).
[9] P.R. Thomas, et al., Phys. Rev. Lett. 80, 5548 (1998).
[10] T. Fujita, Y. Kamada, S. Ishida, Y. Neyatani, T. Oikawa, S. Ide, S. Takeji, Y. Koide, A. Isayama, T. Fukuda, T. Hatae, Y. Ishii, T. Ozeki, H. Shirai, and the JT-60 Team, Nucl. Fusion 39, 1627 (1999).
[11] Dolan, Thomas James, Fusion Research, Pergamon Press (1982).
[12] Bellan, Paul M., Spheromaks: A Practical Application of Magnetohydrodynamic Dynamos and Plasma Self-Organization, Imperial College Press (2000).
[13] H.S. McLean, S. Woodruff, E.B. Hooper, R.H. Bulmer, D.N. Hill, C.T. Holcomb, J. Moller, B.W. Stallard, R.D. Wood, and Z. Wang, Phys. Rev. Lett. 88, 125004 (2002).
[14] P. Martin, et al., Nucl. Fusion 49, 104019 (2009).
[15] M. Fujiwara, et al., Nucl. Fusion 41, 1355 (2001).
[16] Braams, C.M. and Scott, P.E. Nuclear Fusion Half a Century of Magnetic Confinement Fusion Research, Taylor and Francis Group (2002).
[17] D.T. Garnier, A.C. Boxer, J.L. Ellsworth, J. Kensner, and M.E. Mauel, Nucl. Fusion 49, 055023 (2009).
[18] Herman, Robin, Fusion the Search for Endless Energy, Cambridge University Press (1990).
[19] J.L. Luxon, Nucl. Fusion 42, 614 (2002).
[20] Chen, Francis F., Introduction to Plasma Physics and Controlled Fusion – Vol. 1, Plenum Press (1984).
[21] Goldston, R.J. and Rutherford P.H. "Introduction to Plasma Physics", Institute of Physics Publishing (1995).
[22] Wesson, John, Tokamaks - 2nd Edition, Oxford University Press (1997).
[23] R. Bickerton, J.W. Connor, and J.B. Taylor, Nature 229, 110 (1971).
[24] C.E. Kessel, Nucl. Fusion 34, 1221 (1994).
[25] G.M. Staebler, J.E. Kinsey, and R.E. Waltz, Phys. Plasmas 14, 055909 (2007).
[26] Bellan, Paul M., Fundamentals of Plasma Physics, Cambridge University Press (2006).

[27] J.F. Artaud, et al., Nucl. Fusion 50, 043001 (2010).
[28] P.N. Yashmanov, T. Takizuka, K.S. Riedel, O.J.W.F. Kardaun, J.G. Cordey, S.M. Kaye, and D.E. Post, Nucl. Fusion 30, 1999 (1990)
[29] F. Wagner, et al., Phys. Rev. Lett. 49, 1408 (1982).
[30] F. Wagner, et al., Phys. Rev. Lett. 53, 1453 (1984).
[31] M. Kwon, I.S. Choi, J.W. Choi, J.S. Hong, M.C. Keum, K.H. Kim, M.G. Kim, M.K. Park, S.H. Seo, S. Baek, H.G. Jhang, J.Y. Kim, and the KSTAR Team, Fusion Engineering and Design, 71, 17 (2004).
[32] B.J. Xiao, D.A. Humphreys, M.L. Walker, A. Hyatt, J.A. Leuer, D. Mueller, B.G. Penaflor, D.A. Piglowski, R.D. Johnson, A. Welander, Q.P. Yuan, H.Z. Wang, J.R. Luo, Z.P. Luo, C.Y. Liu, L.Z. Liu, K. Zhang, Fusion Engineering and Design 83, 181 (2008).
[33] E.A. Lazarus, et al., Phys. Rev. Lett. 77, 2714 (1996).
[34] R.L. Boivin, et al., Fusion Science and Technology 48, 834 (2005).
[35] M.A. Van Zeeland, J.H. Yu, M.S. Chu, K.H. Burrell, R.J. La Haye, T.C. Luce, R. Nazikian, W.M. Solomon, and W.P. West, Nucl. Fusion 48, 092002 (2008).
[36] F.M. Levington, R.J. Fonck, G.M. Gammel, R. Kaita, H.W. Kugel, E.T. Powell, and D.W. Roberts, Phys. Rev. Lett. 63, 2060 (1989).
[37] D. Wroblewski, and L.L. Lao, Rev. Sci. Instrum. 63, 5140 (1992).
[38] T.S. Taylor, Plasma Phys. Control. Fusion 39, B47 (1997).
[39] T.C. Luce, et al., Nucl. Fusion 41, 1585 (2001).
[40] F. Troyon, R. Gruber, H. Saurenmann, S. Semenzato, S. Succi, Plasma Phys. Controlled Fusion 26, 209 (1984).
[41] T.S. Taylor, E.J. Strait, L.L. Lao, M. Mauel, A.D. Turnbull, K.H. Burrell, M.S. Chu, J.R. Ferron, R.J. Groebner, R.J. La Haye, B.W. Rice, R.T. Snider, S.J. Thompson, D. Wròblewski, and D.J. Lightly, Phys. Plasmas 2, 2390 (1995).
[42] R.J. La Haye, Phys. Plasmas 13, 055501 (2006).
[43] M.F.F. Nave and J.A. Wesson, Nucl. Fusion 30, 2575 (1990).
[44] ITER Physics Basis – Chapter 1: Overview and summary, Nucl. Fusion 39 2137 (1999).
[45] M. Maraschek, G. Gantenbein, Q. Yu, H. Zohm, S. Gunter, F. Leuterer, and A. Manini, Phys. Rev. Lett. 98, 025005(2007).
[46] Bateman, Glenn, MHD Instabilities, The MIT Press (1978).
[47] Z. Chang, J.D. Callen, Nucl. Fusion 30, 219 (1990).
[48] H. Zohm, Plasma Phys. Control. Fusion 38 105 (1996).
[49] A. Kirk, H.R. Wilson, G.F. Counsell, R. Akers, E. Arends, S.C. Cowley, J. Dowling, B. Lloyd, M. Price, and M. Walsh, Phys. Rev. Lett. 92, 245002 (2004).
[50] J.A. Boedo, D.L. Rudakov, E.M. Hollmann, R.A. Moyer, G.R. McKee, K. Burrell, T.E. Evans, A.W. Leonard, W.P. West, M.E. Fenstermacher, M. Groth, S.L. Allen, L. Zeng, G. Wang, J.G. Watkins, and the DIII-D Team, Journal of Nuclear Materials 337-339, 771 (2005).
[51] C.J. Lasnier, D.N. Hill, T.W. Petrie, A.W. Leonard, T.E. Evans, and R. Maingi, Nucl. Fusion 38, 1225 (1998).
[52] T.E. Evans, et al., Phys. Rev. Lett. 92, 235003 (2004).

[53] T.E. Evans, R.A. Moyer, K.H. Burrell, M.E. Fenstermacher, I. Joseph, A.W. Leonard, T.H. Osborne, G.D. Porter, M.J. Schaffer, P.B. Snyder, P.R. Thomas, J.G. Watkins, and W.P. West, Nature Physics 2, 419 (2006).
[54] P.B. Snyder, H.R. Wilson, J.R. Ferron, L.L. Lao, A.W. Leonard, T.H. Osborne, A.D. Turnbull, D. Mossessian, M. Murakami, X.Q. Xu, Phys. Plasmas 9, 2037 (2002).
[55] R.J. Groebner, P.B. Snyder, T.H. Osborne, A.W. Leonard, T.L. Rhodes, L. Zeng, E.A. Unterberg, Z. Yan, G.R. McKee, C.J. Lasnier, J.A. Boedo, and J.G. Watkins, Nucl. Fusion 50, 064002 (2010).
[56] Tobias, Benjamin John, Electron cyclotron emission imaging and applications in magnetic fusion energy, Ph.D. Thesis University of California-Davis (2010).
[57] S. von Goeler, W. Stodiek, and N. Sauthoff, Phys. Rev. Lett. 33, 1201 (1974)
[58] J. Garcia, G. Giruzzi, J.F. Artaud, V. Basiuk, J. Decker, F. Imbeaux, Y. Peysson, and M. Schneider, Phys. Rev. Lett. 100, 255004 (2008).
[59] J. Garcia, G. Giruzzi, P. Maget, J.F. Artaud, V. Basiuk, J. Decker, G. Huysmans, F. Imbeaux, Y. Peysson, and M. Scheider, Nucl. Fusion 50, 025025 (2010).
[60] A.C.C. Sips, et al., Plasma Phys. Control. Fusion 44, B69 (2002).
[61] E. Joffrin, el al., Plasma Phys. Control. Fusion 45, A367 (2003).
[62] A. Isayama, Y. Kamada, N. Hayashi, T. Suzuki, T. Oikawa, T. Fujita, T. Fukuda, S. Ide, H. Takenaga, K. Ushigusa, T. Ozeki, Y. Ikeda, N. Umeda, H. Yamada, M. Isobe, Y. Narushima, K. Ikeda, S. Sakakibara, and K. Yamazaki, Nucl. Fusion 43, 1272 (2003).
[63] M.R. Wade, T.C. Luce, R.J. Jayakumar, P.A. Politzer, A.W. Hyatt, J.R. Ferron, C.M. Greenfield, M. Murakami, C.C. Petty, R. Prater, J.C. DeBoo, R.J. La Haye, P. Gohil, and T.L. Rhodes, Nucl. Fusion 45, 407-416 (2005).
[64] C.C. Petty, M.E. Austin, C.T. Holcomb, R.J. Jayakumar, R.J. La Haye, T.C. Luce, M.A. Makowski, P.A. Politzer, and M.R. Wade, Phys. Rev. Lett. 102, 045005 (2009).
[65] ITER Physics Basis – Chapter 2: Plasma confinement and transport, Nucl. Fusion 39, 2175 (1999).
[66] P.N. Yushmanov, T. Takizuka, K.S. Riedel, O.J.W.F. Kardaun, J.G. Cordey, S.M. Kaye, and D.E. Post, Nucl. Fusion 30, 1999 (1990).
[67] B.W. Rice, Fusion Engineering and Design 34-35, 135 (1997).
[68] C.T. Holcomb, M.A. Makowski, R.J. Jayakumar, S.L. Allen, R.M. Ellis, R. Geer, D. Behne, K.L. Morris, L.G. Seppala, and J.M. Moller, Rev. Sci. Instrum. **77**, 10E506 (2006).
[69] J. Fischbach, Andover Corporation Technical Note "Standard Bandpass Filters – About Bandpass Filters", www.lot-oriel.com.
[70] Goldstein, Dennis, Polarized Light – Second Edition, Revised and Expanded, Marcel Dekker (2003).
[71] Griffiths, David J., Introduction to Electrodynamics-Third Edition, Prentice-Hall (1999).
[72] Kemp, James C., Polarized Light and its Interaction with Modulating Devices – A Methodology Review, Hinds International Application Note, (1987).
[73] F. Perrin, J. Chem. Phys. 10, 415 (1942).
[74] H. Mueller, J. Opt. Soc. Am. 37, 110 (1947).
[75] PEM-90^{TM} Photoelastic Modulator Systems User Mannual, Hind Instruments, Inc. (1994).

[76] J.D. King, M.A. Makowski, C.T. Holcomb, S.L. Allen, R. Geer, W.H. Meyer, D.N. Hill, D. Pham, and E.C. Morse, Rev. Sci. Instrum. **81**, 10D739 (2010).
[77] E.D. Morris, Jr. and H.S. Johnston, Rev. Sci. Instrum. 39, 620 (1968).
[78] A. Restelli, R. Abbiati, and A. Geraci, Rev. Sci. Instrum. 76, 093112 (2005).
[79] L.G. Rubin, Rev. Sci. Instrum. 59, 514 (1988).
[80] R.J. Jayakumar, M.A. Makowski, S.L. Allen, M.E. Austin, A.M. Garofalo, R.J. La Haye, H. Reimerdes, and T.L. Rhodes, Rev. Sci. Instrum. 75, 2995 (2004).
[81] Stanford Research Systems, About Lock-In Amplifiers, Application Note 3, http://www.thinksrs.com/downloads.pdfs/applicationnotes/aboutlias.pdf.
[82] S.J. Lascos and D.T. Cassidy, Rev. Sci. Instrum. 79, 074702 (2008).
[83] Proakis, J.G. and Manolakis, D.G. "Introduction to Digital Signal Processing" Macmillan Publishing Company (1988).
[84] J.D. King, M.A. Makowski, C.T. Holcomb, S.L. Allen, D.N. Hill, R.J. La Haye, F. Turco, C.C. Petty, M.A. Van Zeeland, T.L. Rhodes, W.H. Meyer, R. Geer, and E.C. Morse, Rev. Sci. Instrum. 82, 033515 (2011).
[85] Hamamatsu PMT Data Sheet, http://sales.hamamatsu.com/en/products/electron-tube-division/detectors/photomultiplier-tubes/part-r636-10.php.
[86] Knoll, Glenn F., Radiation Detection and Measurement – Third Edition, John Wiley and Sons, Inc. (2000).
[87] Brigham, E. Oran, The Fast Fourier Transform and its Applications, Prentice-Hall (1988).
[88] L.Lao, H. St. John, R.D. Stambaugh, and W. Pfeiffer, Nucl. Fusion 25, 1421 (1985).
[89] E.J. Strait, Rev. Sci. Instrum. 77, 023502 (2006).
[90] Hutchinson, I.H. "Principles of plasma diagnostics – Second Edition" Cambridge University Press (2002).
[91] R.J. La Haye, R.J. Buttery, S. Guenter, G.T.A. Huysmans, M. Maraschek, and H.R. Wilson, Phys. Plasmas 7, 3349 (2000).
[92] M.E. Austin and J. Lohr, Rev. Sci. Instrum. 74, 1457 (2003).
[93] J.D. King, R.J. La Haye, C.C. Petty, T.H. Osborne, C.J. Lasnier, R.J. Groebner, F.A.G. Volpe, M.J. Lanctot, M.A. Makowski, C.T. Holcomb, W.M. Solomon, S.L. Allen, T.C. Luce, M.E. Austin, W.H. Meyer and E.C. Morse, "Hybrid-like 2/1 flux-pumping and magnetic island evolution due to edge localized mode-neoclassical tearing mode coupling in DIII-D, Phys. Plasmas (submitted).
[94] L.L. Lao, H.E. St. John, Q. Peng, J.R. Ferron, E.J. Strait, T.S. Taylor, W.H. Meyer, C. Zhang, and K.I. You, Fusion Science and Technology 48, 968 (2004).
[95] L.L. Lao, H. St. John, R.D. Stambaugh, A.G. Kellman, W. Pfeiffer, Nucl. Fusion 25, 1611 (1985).
[96] L.L. Lao, J.R. Ferron, R.J. Groebner, W. Howl, H. St. John, E.J. Strait, T.S. Taylor, Nucl. Fusion, 30, 1035 (1990).
[97] Pozrikidis, C. "Numerical computation in science and engineering" Oxford University Press (2008).
[98] D. Wròblewski, K.H. Burrell, L.L. Lao, P. Politzer, and W.P. West, Rev. Sci. Instrum. 61, 3552 (1990).
[99] T. Suzuki, T. Fujita, N. Oyama, A. Isayama, G. Matsunaga, T. Oikawa, N. Asakura, and M. Takechi, Rev. Sci. Instrum. 77, 10E914 (2006).

[100] R.J. Colchin, D.L. Hills, R. Maingi, C.C. Klepper, and N.H. Brooks, Rev. Sci. Instrum. 74, 2068 (2003).
[101] D.N. Hill, T. Petrie, M. Ali Mahdavi, L. Lao and W. Howl, Nucl. Fusion 28, 902 (1988).
[102] D.P. Brennan, A.D. Turnbull, M.S. Chu, R.J. La Haye, L.L. Lao, T.H. Osborne, and S.A. Galkin, Phys. Plasmas 14, 056108 (2007).
[103] C.C. Petty, P.A. Politzer, and Y.R. Lin-Liu, Plasma Phys. Controlled Fusion 47, 1077 (2005).
[104] A. Isayama, G. Matsunaga, T. Kobayashi, S. Moriyama, N. Oyama, Y. Sakamoto, T. Suzuki, H. Urano, N. Hayashi, Y. Kamada, T. Ozeki, Y. Hirano, L. Urso, H. Zohm, M. Maraschek, J. Hobirk, and K. Nagasaki, Nucl. Fusion 49, 055006 (2009).
[105] R.J. La Haye, S. Günter, D.A. Humphreys, J. Lohr, T.C. Luce, M.E. Maraschek, C.C. Petty, R. Prater, J.T. Scoville, and E.J. Strait, Phys. Plasmas 9, 2051 (2002).
[106] R.J. Buttery, R.J. La Haye, R. Gohil, G.L. Jackson, H. Reimerdes, E.J. Strait, and the DIII-D Team, Phys. Plasmas **15**, 056115 (2008).
[107] C.C. Petty, R.J. La Haye, T.C. Luce, D.A. Humphreys, A.W. Hyatt, J. Lohr, R. Prater, E.J. Strait, and M.R. Wade, Nucl. Fusion 44, 243 (2004).
[108] R. Prater, R.J. La Haye, T.C. Luce, C.C. Petty, E.J. Strait, J.R. Ferron, D.A. Humphreys, A. Isayama, J. Lohr, K. Nagasaki, P.A. Politzer, M.R. Wade, and A.S. Welander, Nucl. Fusion 47, 371 (2007).
[109] P.A. Politzer, C.C. Petty, R.J. Jayakumar, T.C. Luce, M.R. Wade, J.C. DeBoo, J.R. Ferron, P. Gohil, C.T. Holcomb, A.W. Hyatt, J. Kinsey, R.J. La Haye, M.A. Makowski, and T.W. Petrie, Nucl. Fusion 48, 075001 (2008).
[110] J.T. Scoville, R.J. La Haye, A.G. Kellman, T.H. Osborne, R.D. Stambaugh, E.J. Strait, and T.S. Taylor, Nucl. Fusion 31, 875 (1991).
[111] F.A.G. Volpe, M.E. Austin, R.J. LaHaye, J. Lohr, R. Prater, E.J. Strait, and A.S. Welander, Phys. Plasmas 16, 102502 (2009).
[112] R.J. La Haye, R. Prater, R.J. Buttery, N. Hayashi, A. Isayama, M.E. Maraschek, L. Urso, and H. Zohm, Nucl. Fusion 46, 451 (2006).
[113] R.J. La Haye, J.R. Ferron, D.A. Humphreys, T.C. Luce, C.C. Petty, R. Prater, E.J. Strait, and A.S. Welander, Nucl. Fusion 48, 054004 (2008).
[114] D.A. Humphreys, J.R. Ferron, R.J. La Haye, T.C. Luce, C.C. Petty, R. Prater, and A.S. Welander, Phys. Plasmas 13, 056113 (2006).
[115] Z. Chang, J.D. Callen, E.D. Fredrickson, R.V. Budny, C.C. Hegna, K.M. McGuire, and M.C. Zarnstorff, Phys. Rev. Lett. 74, 4663 (1995).
[116] R.J. Fonck, D.S. Darrow, and K.P. Jaehnig, Phys. Rev. A, 29, 3288 (1984).
[117] M.E. Fenstermacher, A.W. Leonard, P.B. Snyder, J.A. Boedo, N.H. Brooks, R.J. Colchin, D.S. Gray, R.J. Groebner, M. Groth, E.M. Hollmann, C.J. Lasnier, T.H. Osborne, T.W. Petrie, D.L. Rudakov, H. Takahashi, J.G. Watkins, L. Zeng, and the DIII-D Team, Plasma Phys. Control. Fusion 45, 1597 (2003).
[118] J.A. Boedo, D.L. Rudakov, E. Hollmann, D.S. Gray, K.H. Burrell, R.A. Moyer, G.R. McKee, R. Fonck, P.C. Stangeby, T.E. Evans, P.B. Snyder, A.W. Leonard, M.A. Mahdavi, M.J. Schaffer, W.P. West, M.E. Fenstermacher, M. Groth, S.L. Allen, C.J. Lasnier, G.D. Porter, N.S. Wolf, R.J. Colchin, L. Zeng, G. Wang, J.G. Watkins, and T. Takahashi, Phys. Plasmas 12, 072516 (2005).

[119] R.J. Colchin, D.L. Hills, R. Maingi, C.C. Klepper, and N.H. Brooks, Rev. Sci. Instrum. 74, 2068 (2003).
[120] F.M. Levinton and H. Yuh, Rev. Sci. Instrum. 79, 10F522 (2008).
[121] K. Kamiya, T. Fujita, A. Kojima, and H. Kubo, Rev. Sci. Instrum. 81, 033502 (2010).
[122] D.M. Thomas, Rev. Sci. Instrum. 74 1541 (2003).